ANALYTICAL METHODS, INC. REPORT 9304

A NOVEL POTENTIAL/VISCOUS FLOW COUPLING TECHNIQUE FOR COMPUTING HELICOPTER FLOW FIELDS

FINAL REPORT

Prepared for:

NASA AMES RESEARCH CENTER
Moffett Field, California 94035

Under Contract NAS2-13194
SBIR Phase II

Prepared by:

J. Michael Summa
Daniel J. Strash
Sungyul Yoo

ANALYTICAL METHODS, INC.
2133 - 152nd Avenue, NE
Redmond, WA 98052

June 21, 1993

```
   12. STIMS 3X ACC#  9336347     ISSUE # =  99     IPS-FILE ADABAS # =   10557
FICHE AVAIL    = AD            HARD COPY AVL = OK            COPYRIGHT      = N
ORIG AGENCY    = NASA          RECEIPT TYPE  = REG           ACQUIS  TYPE   = REG
DOCUMENT CLASS= TRP            ACCESS LEVEL  =   0           ACCESS RESTR   = UNRES
LIMITATION CAT= NONE           DOCUMENT SEC  = NC            TITLE SECURITY= NC
SUBJECT CATGRY= 02             SPECIAL HANDL =               PAGE COUNT     = 00089
INC AUTHOR LST= N              INC CNTRCT LST= N             LANGUAGE       = EN
COUNTRY ORIGIN= US             COUNTRY FINANC= US            ABSTRACT PREP  = NON
PUB DATE       = 19930621      CORP SOURCE   = AV021240      JOURNAL PAGE   =    0

TITLE          = A novel potential/viscous flow coupling technique
TITLE          = for computing helicopter flow fields
TITLE SUPP     = Final Report, 16 Mar. 1990 - 26 May 1993
AUTHOR       1 = Summa, J. Michael
AUTHOR       2 = Strash, Daniel J.
AUTHOR       3 = Yoo, Sungyul
CONTRACT NUM   = NAS2-13194
CONTRACT NUM   = SBIR-02.09-9090
REPORT NUM     = NASA-CR-193272
REPORT NUM     = NAS 1.26:193272
REPORT NUM     = AMI-9304
SALES AGY PRIC= Contact the Ames SBIR Field Center Manager for fur
SALES AGY PRIC= ther information
MAJOR TERMS    = COMPUTATIONAL FLUID DYNAMICS
MAJOR TERMS    = FLOW DISTRIBUTION
MAJOR TERMS    = HELICOPTERS
MAJOR TERMS    = POTENTIAL FLOW
MAJOR TERMS    = VISCOUS FLOW
MINOR TERMS    = COMPUTERIZED SIMULATION
MINOR TERMS    = NAVIER-STOKES EQUATION
FORM OF INPUT = HC

***************    END OF ADABAS RECORD #      10557     ***************
```

ABSTRACT

The primary objective of this work was to demonstrate the feasibility of a new potential/viscous flow coupling procedure for reducing computational effort while maintaining solution accuracy. This closed-loop, overlapped, velocity-coupling concept has been developed in a new two-dimensional code, ZAP2D (Zonal Aerodynamics Program-2D), a three-dimensional code for wing analysis, ZAP3D (Zonal Aerodynamics Program-3D), and a three-dimensional code for isolated helicopter rotors in hover, ZAPR3D (Zonal Aerodynamics Program for Rotors-3D). The ZAP2D comparisons with large domain ARC2D solutions and with experimental data for a NACA 0012 airfoil have shown that the required domain size can be reduced to a few tenths of a percent chord for the low Mach and low angle of attack cases and to less than 2-5 chords for the high Mach and high angle of attack cases while maintaining solution accuracies to within a few percent. This represents CPU time reductions by a factor of 2-4 compared with ARC2D. The current ZAP3D calculation for a rectangular plan-form wing of aspect ratio 5 with an outer domain radius of about 1.2 chords represents a speed-up in CPU time over the ARC3D large domain calculation by about a factor of 2.5 while maintaining solution accuracies to within a few percent. A ZAPR3D simulation for a two-bladed rotor in hover with a reduced grid domain of about two chord lengths was able to capture the wake effects and compared accurately with the experimental pressure data. Further development is required in order to substantiate the promise of computational improvements due to the ZAPR3D coupling concept.

TABLE OF CONTENTS

LIST OF FIGURES

LIST OF FIGURES (Cont'd)

LIST OF FIGURES (Cont'd)

LIST OF FIGURES (Concl'd)

NOMENCLATURE

AR	Wing Aspect Ratio
A-H	Grid domain labels
C_ℓ, C_d, C_m	Two-dimensional lift, drag and pitching moment
$C_{\ell_{MAX}}$	Maximum two-dimensional lift coefficient
C_L, C_D, C_{My}	Three-dimensional lift, drag and pitching moment
C_Q	Rotor torque coefficient
C_T	Rotor thrust coefficient
j, k, ℓ	Grid indices
n	Unit surface normal
r	Local dimensionless rotor radius
R	Domain boundary radius normalized by chord length
R_e	Reynold's Number
S	Domain boundary surface
V, v	Velocity field
θ_{75}	Rotor collective in degrees
ϕ	Surface velocity potential
Ψ	Azimuth angle
Δ	Finite difference
∂	Partial derivative
γ	Surface vorticity
α	Angle of attack in degrees

Subscripts, Superscripts

i, o	Inner and outer boundary
w	Wake
c	Corrected
g	Geometric

1.0 INTRODUCTION

The flow fields associated with full configuration, fixed- and rotary-wing aircraft are extremely complicated and remain a challenge for applied computational aerodynamics. While linear methods or potential flow models of nonlinear wake shape effects have become commonly used techniques for aircraft performance predictions and analyses, the nonlinear methods that incorporate more correct mathematical models of the actual flow physics—such as compressibility and viscosity—are being developed and applied by research scientists. Much progress has been made in solving the full potential, Euler, and various forms of the approximate Navier-Stokes (NS) equations; however, because of the wide variation of physical scales of characteristic fluid phenomena from boundary layer thickness, shock thickness, or vortex core radius to wing span or fuselage length, a zonal method of analysis is generally projected for the entire aircraft flow field calculation. In such a zonal approach, the flow field is partitioned into zones which utilize approximate equations appropriate to the flow physics within each zone (e.g., Ref. 1 and 2). Although a zonal CFD code is more complex than, say, a NS code for the entire flow domain, required CPU time and computer memory should be significantly reduced and/or accuracy improved because of increased grid resolution where viscous or shock effects dominate.

In the Phase I research effort, a new procedure for coupling potential and viscous flow calculation schemes for a simple airfoil at low angle-of-attack was developed. In the Phase II work reported here, the two-dimensional concept is explored for the higher angle-of-attack range and is further developed for transonic effects. The coupling procedure is expanded to three-dimensional wing simulations and then generalized for helicopter rotor simulations in the hover/climb flight condition. In the rotor procedures, rotational effects are added to the NS code and secondary blade and wake influences outside of the NS domain are included in an outside iterative loop by a specialized potential flow hover code. The resultant two-zone methods, ZAP2D, ZAP3D and ZAPR3D (Zonal Aerodynamics Program-2D/3D and Rotor/3D), couples a potential flow panel method with a NASA Ames NS code, ARC2D and ARC3D respectively.[3] The coupling concept is based on the premise that any computational method can only produce valid results within the approximations of the physical model employed in its construction. Therefore, the interfacing boundary surface between the potential and viscous flow code domains must be very nearly potential in order to achieve a successful (accurate) result. This is accomplished by utilizing an overlapped, velocity-coupling procedure with the unique feature that (beyond the first iteration) the potential flow surface panel strengths are obtained from the NS solution at a smooth inner fluid boundary. These fluid surface panel values are then used to compute the outer velocity boundary conditions for the NS calculation. The iteration between the potential flow solution and the NS solution continues in a closed loop until flow convergence, or allowable iteration limits, are obtained.

2.0 METHODOLOGY

2.1 Two-Dimensional Investigation

In this work, the coupling procedure is investigated and validated for two-dimensional high angle-of-attack and transonic airfoil simulations. The two-dimensional potential flow panel code, POT2D, has been fully coupled with the thin-layer, NS code, ARC2D. Both of these codes have already been extended to three-dimensional flows, VSAERO[4] and ARC3D,[3] respectively, and have been widely used and proven to be robust and computationally accurate flow simulation programs. The limits of the validity of the zonal procedure is established in the present work by comparing the ARC2D-alone simulation for large domain size with the fully-coupled ZAP2D simulation for small domain size for a range of angle of attack and Mach number.

2.1.1 Zonal Concept

In this zonal approach the flow field is partitioned into linear potential flow and viscous flow regions. The two computational zones overlap and the innermost coupling boundary is located in the computed flow field where the approximations inherent in both methods are valid; consequently, the interfacing boundary surface between the potential and viscous flow regions must be very nearly potential in order to achieve an accurate result.

The general coupling concept for the zonal method is illustrated in Figures 1 and 2. Figure 1 shows the zonal representation of the physical flow field while the flow chart of the iteration scheme is shown in Figure 2. An inner boundary, S_i, which is measured by a radius, say R_i, is constructed to enclose a generally shaped body or airfoil and the fluid region near the body where viscous effects dominate. Although the body might be a complex shape, the inner boundary surface, S_i, would be a simple, smooth geometry. An additional outer surface, S_o, which is measured by a radius, say R_o, also of simple shape, forms the computational domain of the viscous calculation. On the other hand, the potential flow domain extends from the inner boundary, S_i, to an infinite distance from the body surface. Consequently, the two computational domains overlap between the surfaces, S_i and S_o. Since S_i should be approximately a potential flow surface, the distance between S_i and S_o should be minimized for optimum computational efficiency. Of course, the minimum overlap will be determined by numerical error limitations.

The iterative coupling of the zonal method proceeds as follows (see Figure 2).

1. The calculation procedure is initialized by computing the potential flow associated with the body motion. An integral panel method is used for this computation. In this first step only the actual body surface is represented by discrete panels and the surface potential equation is solved directly by enforcing the Neumann boundary condition.

2. The velocity field, V_o, on the outer boundary, S_o, is computed from the known potential flow surface singularity solution.

3. This velocity field, V_o, serves as the outer boundary values for the NS calculation. Once the NS solution for the flow inside S_o is obtained, the velocity field due to the viscous solution, say V_i on S_i, which is just outside the region of viscous effects, is also known.

4. This inner boundary velocity, V_i, can therefore be used to construct the known corresponding values of the potential flow panel strengths on S_i; consequently, all further potential flow calculations require only the paneling of the smooth inner boundary, S_i, and not the actual body surface. In this way, numerical errors due to complex geometric modeling and calculation of the outer boundary velocity field, V_o, should be minimized and any contamination of the NS simulation due to this source of error should be avoided.

5. This iteration loop, Steps 2-4, is repeated until the NS method is converged or iteration limits are achieved. Convergence should be measured by flow field and integrated force and moment asymptotic behavior.

2.1.2 Potential Flow Module

As is well known, the potential describing an inviscid, irrotational, incompressible flow can be expressed by its boundary values.[5] Specifically, an integral solution of Laplace's equation for the velocity potential can be derived by application of Green's theorem. The resultant boundary integral equation for the surface velocity potential is composed of two integrals:

1. A body surface integral of a doublet kernel function of strength, ϕ, and a source kernel function of strength, $\partial\phi/\partial n$, and

2. A thin wake surface integral of a doublet kernel function of strength, $\Delta\phi_w$.

Of course, the wake strengths, $\Delta\phi_w$, are related to the body surface potential, ϕ, through the wake auxiliary Kutta condition and the body source strengths, $\partial\phi/\partial n$, are known by the tangent flow boundary condition on the body. Hence the integral equation for ϕ can be solved directly as suggested by Morino.[6] In POT2D, the integral equation is discretized and transformed into an algebraic equation by representing the boundaries with flat panels and approximating the local panel source and doublet strengths with constant values just as in VSAERO. In the current code, the source strengths, $\partial\phi/\partial n$, are provided by the ARC2D normal velocity components on S_i and the matrix equation is solved for the corresponding potential doublet strength distribution, ϕ, on S_i.

A wake model is used which implies a branch cut to infinity, thus canceling the vortex left at the upper and lower trailing edges of the S_i boundary due to the truncation of the potential doublet panels (Figure 1). Additionally, an error may be introduced due to the truncation of the perturbation source strength at the rear of the inner surface. For this reason, the downstream outflow boundary remains at 5 chords beyond the airfoil trailing edge for all grid domains tested. That is, the ARC2D solution near the outflow boundary at the coupling surface, S_i, is assumed to be near free stream conditions.

Once the surface potential is computed, surface velocities are obtained by numerical differentiation and forces and moments are found by pressure integration. Further, off-body flow velocities are computed by integration of surface velocity source and doublet influence functions. The Karman-Tsien method[7] is used to correct the surface and field velocities for compressibility effects.

2.1.3 Viscous Flow Module

As noted earlier, ARC2D, originally developed by Pulliam and Steger[3] at NASA Ames, has been widely used in the computation of airfoil aerodynamics. The code has been continually improved by Pulliam and colleagues,[8, 9, 10] and the details of the theory are well documented in these references.

The basic equations solved by ARC2D are the Reynolds-averaged NS equations written in strong conservation-law form. These are simplified by including the standard thin-layer approximation for the viscous terms. The thin-layer approximation is known to be adequate for separation problems with subsonic or transonic free streams when the flow field associated with separation is convection-dominated.

For turbulent flows, the well-known Baldwin-Lomax algebraic model[11] is used for turbulence closure. This turbulence model has been used in computing solutions for a wide variety of flow conditions and has been found to be acceptably accurate.

The numerical algorithm is an implicit approximate factorization, finite-difference scheme, which can be either first- or second-order accurate in time.

Over the years of development of ARC2D, unique features have been added to the code to improve its capability to accurately predict aerodynamic characteristics for airfoil calculations. One of these features is an implementation of a viscous-inviscid coupling. A point vortex correction model has been installed to reduce the solution dependency on the size of the outer boundary. Here, circulation on the far-field boundary is set based on the ARC2D computed C_l. Using this velocity correction together with adjustments for compressibility, modified outer velocities are constructed. It is noted that this correction yields accurate results for domains larger than 4 chords in length.[12]

2.1.4 Boundary Conditions

In ZAP2D, a parallel procedure is employed whereby the POT2D computed velocities with compressibility correction are used as far-field boundary conditions. At the outer boundary, velocities and pressure corrected for compressibility are specified and density is calculated from the pressure and free stream stagnation enthalpy. Since velocities, pressure and density are known, energy at the boundary can be determined.

Since the POT2D formulation is based upon an incompressible flow assumption and the ARC2D formulation upon a compressible flow assumption, flow variables calculated at both boundaries must be compatible with each assumption. For this purpose, a simple method by Karman-Tsien, based upon the tangent-gas approximation, is used for the compressibility correction. At the inner boundary, velocity components calculated by ARC2D are converted to incompressible transpiration velocities for the POT2D representation. The pressure coefficient and velocity components calculated by POT2D at the outer boundary are in turn modified for compressibility for the ARC2D boundary conditions. These routines are alternated in the coupling procedure.

2.2 Three-Dimensional Investigation

The concept directly follows the previously described two-dimensional work, which employs an overlapping velocity coupling technique. As discussed, this method requires that the overlapping region is located where potential flow approximations are valid. Consequently, the actual wing surface and the viscous (or transonic) region near the wing are excluded from the overlapping boundaries. This zonal concept has been utilized to fully couple the widely used Navier-Stokes code, ARC3D,[3] with the potential flow panel code VSAERO.[4]

The grid generation for this task was accomplished with the interactive code, HYGRID. developed by Visual Computing, Inc.[13] This code was designed under the concept of Object Oriented Programming, and is capable of multi-block, hyperbolic grid generation about general three-dimensional configurations.

The theoretical basis for the extension to three dimensions follows the two-dimensional version detailed in Section 2.1; therefore, further details are not required here. The validation of the resultant computer code, ZAP3D (Zonal Aerodynamics Program 3-D), will be discussed in Section 3.2.

2.3 Three-Dimensional Wing/Vortex Investigation

A wing/vortex interaction problem was investigated in order to test the requirement of capturing the vortex within the outer zonal boundary. The ability of the method to handle a vortex passing into the reduced zonal domain is fundamental to any rotor simulation. Two methods for this problem were investigated. One is to prescribe the known vortex core as fixed boundary conditions at the appropriate grid points within S_o. This simple technique could eliminate the need for increased grid density near the vortex. The other is to use the S_o boundary velocities perturbed by the vortex core.

In either case, no changes were required to the basic potential flow module for the wing/vortex simulation. However, for validation purposes, a subroutine was added to ARC3D. This routine was utilized to test the accuracy of VSAERO to compute the induced velocities due to a vortex of known strength and location by the Biot-Sevart law.

2.4 Hover/Climb Rotor Investigation

The zonal method has been generalized for an isolated rotor in hover or climb. Since the experimental data by Caradonna and Tung[14] and calculations by Srinivasan, et. al.[15,16] and others[17,18] were available for comparison purposes, a test case of a two-bladed, aspect-ratio-6 rotor with a NACA 0012 section was chosen for this investigation. Some important issues were addressed, such as:

a) Whether to modify ARC3D for a rotor flow simulation or use any readily available rotor code,

b) Which type of grid system to be employed about the rotor configuration, and

c) How to efficiently couple ARC3D, ZAP3D, and a rotor code to provide correct boundary conditions.

Any viscous flow code alone may not properly calculate the flow of a lifting rotor unless its domain size is large enough to consider far boundaries as undisturbed ones, since the rotor induces significant velocities at large distances from the rotor. Therefore, specification of a no-flow condition at the inflow boundaries of a computational box, which is typically small for economy, poses a difficulty for the prediction method. This no-flow condition produces a closed box environment for the rotor in which the flow recirculates within the computational box. Here, a simple and economical computation program called HOVER,[19] which was developed by Summa using a vortex lattice method, is used to provide velocity boundary conditions at certain boundaries. (Nonlifting flow calculations can be done without using externally specified boundary conditions; namely using the freestream boundary

conditions.) For viscous flow calculations, various options were considered, which include the use of any rotor code available in the public domain and modification of ARC3D for rotational flow. Also, in the case of using ARC3D, the possibility of adopting either an unsteady approach for a rotating blade or a steady one for a fixed blade rotor with a rotating freestream was investigated. After some research, it was found that the modification of ARC3D for a blade-fixed representation could be achieved easily by adding rotational freestream terms in the subroutine RHS of ARC3D.

2.4.1 Zonal Concept for HOVER

For the three-dimensional rotor simulation, the zonal concept developed for wings in translation is generalized to include flow disturbances outside the NS domain. Since this general procedure is more complicated than described earlier, it is discussed in some detail here. The zonal representation of the hover/climb flow field is illustrated in Figure 3. Since this problem is axisymmetric, a single blade, say, the primary blade, is fully immersed within the NS domain, S_o. While one might choose to simulate only the outer portion of the blade with the viscous code, it is hoped that the zonal coupling within S_o will allow for the entire blade simulation and, hence, a root vortex. The effects of secondary blades and wake surfaces outside of S_o are included by updating S_o boundary conditions with a potential flow method, the Analytical Methods, Inc. (AMI) HOVER code.[19] The technique of utilizing a potential flow hover calculation to initialize the finite difference domain boundary condition has been employed by other investigators.[14,20,21] However, the reduced outer boundary domain, S_o, due to this potential/viscous coupling within S_o, should allow for the closed-loop update of these outside potential flow influences. Such updating will be required to properly address viscous and compressible effects on hover/climb performance.

The generalized zonal iteration scheme is shown in Figure 4. There are two iterative loops—an inside loop that uses the three-dimensional extension of the potential/viscous coupling procedure investigated in Phase I and an outside loop to update the potential model of the flow disturbances outside of the NS domain which are driven by the viscous simulation. The iterative coupling of the general method proceeds as follows.

1. The calculation procedure is initialized by computing a potential flow associated with the body motion. In fixed wing and body applications, an integral panel method developed by AMI, VSAERO,[4] would be used. For the rotor problems, programs HOVER and/or ROTAIR,[19] also developed at AMI, will be used for this step.

2. The velocity field, say, $V^o_{S_o}$, on the outer boundary, S_o, due to potential flow disturbances outside S_o is computed.

3. The velocity field, say, $V^i_{S_o}$, on the outer boundary, S_o, due to potential flow disturbances inside S_o is computed.

4. The resultant velocity field, V_o, serves as the outer boundary values for the NS calculation. Once the NS solution for the flow inside S_o is obtained, the disturbance velocity field due to viscous and compressible effects, say, V_i on S_i, which is just outside the region of viscous/transonic effects, is also known.

5. This inner boundary velocity, V_i, can therefore be used to generate known corresponding values of source strength, $\partial\phi/\partial n$, and surface vorticity, γ. These source and vorticity

strengths on S_i are required for a new potential flow velocity update on S_o, i.e., $V^i_{S_o}$. Again, all further potential flow updates within S_o require only the paneling of the smooth inner boundary, S_i. Therefore, numerical errors in $V^i_{S_o}$ should be minimized and contamination of the NS simulation should be avoided.

6. This inside S_o iteration loop, Steps 3-5, is repeated until the NS method is converged or iteration limits are achieved. Convergence should be measured by flow field and integrated force and moment convergence.

7. For the rotor case, the NS computed blade loading and wake development can then be used to update the potential flow simulation outside of S_o. For example, secondary blades and wakes can be *assigned* new potential flow strengths and wake positions can be recomputed for fixed blade loading.

8. With new blade and wake surface potential flow singularities obtained, an outside iterative loop is executed by returning to Step 2 and updating $V^o_{S_o}$. Once more, this outside loop can be continued until blade loading is unchanged or iteration limits are obtained.

2.4.2 Potential Flow Module

For the hover/climb case, the potential flow module included in ZAP3D for updating S_o boundary conditions due to NS changes at S_i requires only minor changes. Specifically, the onset flow components as seen from the fixed-blade reference are extracted from the velocities at S_i so that the Green's function approach is applicable. Then, disturbance velocity updates to S_o due to the potential flow solution at S_i are added to the local onset flow components at S_o. While these simple modifications take care of the secondary velocity coupling updates within ZAPR3D, the initial potential flow solution for the rotor flow field and also the secondary blade and wake influences outside of S_i required the coupling with a full rotor simulation package, HOVER.

HOVER is a "linearized" lifting-surface representation of the rotor airloads that is accomplished by a vortex lattice placed on the rotor planform area in the disk plane as illustrated in Figure 5. In HOVER, the influences of individual panels in the blade lattice are computed by quadrilateral vortex rings; therefore, the basic unknowns in the flow tangency equations are the panel ring vortex strengths, or, equivalently, panel doublet strengths. The program includes prescribed as well as relaxed wake calculations. If the user has supplied elastic blade properties, the elastic twist and bending deformations and their impact on the rotor loads are computed during the program iterations. The user can also request a thrust coefficient and the program will adjust the collective setting through the prescribed wake iteration to obtain the thrust. The relaxed wake calculation then proceeds at fixed collective.

Once a converged wake geometry is computed by the prescribed wake or relaxed wake options, inviscid forces and moments on the blade bound vortex segments are then evaluated in the usual way by applying the Kutta-Joukowski Law. Of course, the chordwise and radial pressure jump distributions are also calculated.

Finally, with the sectional coefficient of lift distribution known from the lifting-surface calculation, the profile drag and, hence, profile and total torque must be determined by falling back on empirical data. This reliance on empiricism is, of course, removed in the ZAPR3D representation, which includes the full viscous terms.

The discrete vortex filaments shed from the trailing edge of each blade represent the hovering rotor wake, which quickly separates into two parts for conventional rotors—an inboard sheet of weaker vorticity and an outer tip sheet that rapidly rolls up to form a very strong tip vortex. HOVER also includes a simple model of the tip vortex shedding across the blade chords shown in Figure 5, which improves the prediction of aerodynamic loading near the rotor tip.

The overall wake structure in the HOVER program is illustrated in Figure 6, and consists of near-, intermediate-, and far-wake regions. The dimensionless axial coordinates at the start of the intermediate- and far-wake regions are ZFAR1 and ZFAR2, respectively. The near-wake region generally includes four vortex passes below the generating blade and is the region of wake relaxation. The intermediate-wake region serves as a "buffer" zone between the near-wake filaments and far-wake model. In the far-wake, each helical vortex filament is continued as a semi-infinite cylindrical sheath of uniform vorticity. The far-wake velocity contribution is then computed by the equivalent source disc located at ZFAR2.

Generally, the calculated thrust at the completion of the prescribed wake iteration for fixed blade collective is too high, and a relaxed wake iteration is required to compute realistic rotor performance. This is because the empirical equations are derived from experimental data of thrust, torque, and tip-vortex filament geometry. Consequently, prescribed wake programs demonstrate good correlation for integrated loads for a large number of conventional rotors since the prescribed wake constants are intimately related to the theoretical methods used to construct the empiricisms. However, these methods are less successful when compared with known collective settings, which implies that although integrated performance is predicted successfully, local sectional loads may not be properly calculated. Certainly, if the wake itself deviates from the experimental data base for the prescribed wake constants, performance predictions could be significantly in error.

The relaxed, force-free wake procedure includes the Scully code model[22] and the self-induced velocity contribution derived from the work reported by Widnall.[23] Additionally, velocity components along vortex filaments are computed in cylindrical polar coordinates. The radial, V_R, and axial, V_Z, velocity components are integrated over a time step that is adjusted by the average tangential, V_T, velocity components across the particular wake segment. Consequently, the final wake azimuthal gridding remains fixed throughout the relaxation iterations, and wake deformations are computed in these azimuthal planes.

The calculated radial circulation distribution is analyzed at each prescribed or relaxed wake iteration to calculate the inboard extent of the tip vortex roll-up. During the relaxed wake iterations, if the radial position of the maximum circulation shed into the tip vortex changes by more than 4% of the radius, and the option to relax only the tip vortex geometry is active, then the wake segmentation is regenerated, growing or eliminating the necessary "inner sheet" filaments, based on prescribed wake constants computed from the current relaxed wake position.

Finally, in order to utilize HOVER in the ZAPR3D procedure, a general velocity scan subroutine was developed that also interfaced with the required ARC3D boundary condition surfaces. In particular, procedures for locating the wake penetration points through S_i and also for summing the wake and secondary blade velocity influences outside of S_i were devised. Additionally, three-dimensional graphics displays were developed for visualizing and debugging the rotor velocity fields required in the ZAPR3D simulation.

2.4.3 Viscous Flow Module

Major modifications in the viscous modules include those in ARC3D and the grid generation routines.

For a rotor version of ARC3D, rotational freestream terms as a function of radius were added to the subroutine RHS. Because the grid system is constructed on a blade-fixed reference, no unsteady approach is necessary. Of course, if forward flight is of concern, then the grid should be generated at respective azimuthal angle positions to reflect the proper rotational velocities as well as advancing ones.

Many different sets of boundary conditions, including a characteristic-type boundary condition procedure, were examined to find the effect of each boundary condition. All the boundary conditions are explicitly specified, in order to obtain the most consistent solution behavior. At the wall, a no-slip boundary condition is used. The density at the wall is determined by a zeroth order extrapolation. The pressure along the body surface is calculated from the normal momentum relation. To ensure the continuity across the wake cut for the H-grid topology, the flow quantities are determined by averaging the flow variables from both sides of the singular plane. At the far-field boundary, velocities and density are extrapolated and pressure is assumed constant. At the upstream and downstream planes, velocity components are prescribed by HOVER calculations. Pressures at both planes are extrapolated and density is assumed constant. At the root boundary conditions, density and pressure are assumed to be same as these at the inner grid point. Contravariant velocity components are extrapolated. Finally, at all boundaries, the total energy is determined from the equation of the state. For the nonlifting case only, the upstream and downstream flow properties of the H-topology grid are swapped using a periodicity condition in the blade azimuthal direction.

2.4.4 Grid Module

A body-conforming, finite-difference grid of a cylindrical type has been used for one rotor blade (with a rounded-tip cap) because of the periodic nature of the hover flow field. In this grid setting, since no forward flight is concerned, the free stream rotates in the clockwise direction while the rotor is fixed at a given azimuthal angle. In contrast to the grid system (a C-C type) constructed for the three-dimensional, rectangular wing in translation, a C-H type grid system was chosen such that C-mesh planes along the radial direction from the rotor axis could better describe the rounded tip geometry, and H-mesh planes along the streamwise direction could be easily duplicated. Once the H-type mesh was generated on the rotor, the grid planes at both leading edge and the trailing edge were rotated to represent the upstream and the downstream of the rotor. Although smaller domains erected on a part of the rotor configuration may be used for zonal calculations, domains of about two chords away from the surface which include the entire rotor blade, were generated. On the other hand, a nonlifting flow calculation included a hemispherical domain which was generated for periodic boundary conditions to be applied at both inlet and exit planes. In general, the grid was clustered near the leading and trailing edges and near the tip region to resolve the tip vortex. It was also clustered in the normal direction with a geometric progression in order to resolve the viscous flow near the blade surface. In these cases, there are about 10 to 15 points in the boundary layer with a spacing of the first grid point from the surface equal to 0.00005 chord. This corresponds to a y+ value of 0(1) in order to capture the viscous sublayer effect. Also, the inboard plane near the axis of rotation was located at a radial station equal to one chord length and a full cosine distribution of grid points was employed with an equal distribution of grid points at the tip region.

A simple algebraic grid generation method was used. By using surface normals on the given surface points, prescribed far-field normals, and a geometric progression ratio which is calculated from the characteristic size of domain, the grid system of limited azimuthal range is generated.

3.0 COMPUTED RESULTS

3.1 Two-Dimensional Validation

The effectiveness of the coupling procedure installed in ZAP2D[24] is measured by demonstrating accurate and converged solutions for a range of angles of attack at subsonic Mach number in section 3.1.1[25] and at angles of attack near the two-dimensional $2C_{l_{MAX}}$ point over a range of free stream Mach Numbers in Section 3.1.2,[26] together with decreasing domain size. The impact of the coupling technique on solution convergence characteristics and on required boundary size for a given accuracy in lift, drag and pitching moment has been investigated. In this work, the NACA 0012 airfoil was selected for the validation cases because of the experimental data base.[27]

3.1.1 Angle of Attack Validation

The validity of ZAP2D effectiveness in angle-of-attack cases is demonstrated with the NACA 0012 airfoil for decreasing domain size in comparison with the large-domain ARC2D simulation and with the experimental database. Calculations assuming a fully turbulent flow field were made with a Reynolds number of 3.0 million based on the chord length and the free stream velocity corresponding to a Mach number of 0.3. Geometric angles of attack from the experimental data by Harris,[27] ranging up to the stall angle, were specified in the computations with the corrections suggested by Harris.

3.1.1.1 Grid Domain Cases

A total of six grid domains for the NS calculations were utilized to investigate the blockage effects of the outer boundary on ZAP2D performance. Table 1 shows the grids and the corresponding case identifiers, where R_o is normalized by chord length. A basic C-type grid around the NACA 0012 airfoil was generated by an algebraic method where surface normal is maintained (Figure 7). The total number of grid points ranges from 12,025 (185 x 65) for the largest domain with R_o=25 chord lengths (Grid A) to 6,549 (177 x 37) for the smallest domain with R_o=0.12 chord lengths (Grid F). Successive grids (B through F) were obtained by stripping off outer grid points from Grid A. The upper and lower airfoil surfaces each have 80 grid points for all grids, while the wake surface has 12 points for the largest domain. The grid generated is clustered near the surface with a normal spacing of 0.000025 so that the effect of the viscous sublayer can be captured, and also clustered at both the leading and trailing edges with a spacing of 0.002. For the POT2D calculation, the location of the inner boundary surface, S, was held fixed at a distance approximately 10% of the chord from the airfoil surface.

GRID	MESH SIZE	R_o	$1/R_o$
A	185 x 65	25.0	0.04
B	181 x 57	5.0	0.20
C	177 x 45	0.5	2.0
D	177 x 39	0.17	5.8
E	177 x 38	0.14	7.1
F	177 x 37	0.12	8.3

Table 1. Summary of Grid Domains.

3.1.1.2 Validation and Domain Size Effects

ZAP2D and ARC2D (Version 195) were ported to the Stardent Titan and also to the IRIS 4D/240GTX workstation. To investigate the effects of domain size (Grids A-F) on the integrated forces and moment computed by ZAP2D and ARC2D calculations for fixed input parameters were performed with Grid A as a baseline calculation for each angle-of-attack case. The full NS option was utilized and calculations were continued for 1,000 iterations. Originally, it was expected that post-stall behavior would be investigated with ARC2D and the effectiveness of the ZAP2D coupling could be measured for flow separation conditions. However, various attempts, including a time accurate approach, smaller Δt, and various dissipation coefficients, have not yielded consistent results for such cases. This shortcoming of the NS simulation has also been recently documented by Raghavan et al.[28] Consequently, the maximum angle-of-attack case reported here is $\alpha=14.53°$.

ZAP2D converged solutions were obtained for all domain sizes and angles of attack up to $\alpha=12.86°$. At $\alpha=14.53°$, ZAP2D diverged for Grids E and F. While this behavior might be due to numerical error in the ZAP2D boundary condition updates or violation of the potential flow assumption at the inner boundary, ARC2D itself might also exhibit some instabilities for such small domains.

The robustness and stability of ARC2D for small domains was checked by imposing boundary conditions computed by ARC2D with the large Grid A domain. In this study, it was found that accurate solutions within the small domains were obtained only if the turbulent viscosity was calculated up to the edge of the outer boundary where the magnitude of the vorticity was less than 1% of the maximum level around the airfoil. This is in contrast to the standard 75% of the domain size that is coded in ARC2D. With this change to ARC2D, the ARC2D computed loads for Grids C-E, subject to the outer and downstream boundary conditions provided by the Grid A ARC2D solution, exhibited deviations compared with the Grid A solution of less than 0.2% of C_ℓ and of about 5% of C_d and C_m. On the other hand, a solution could not be obtained for Grid F; hence, with the current coding in ARC2D which includes turbulent viscosity throughout the entire domain, the smallest domain size where a converged ZAP2D solution could be expected for $\alpha=12.86°$ would be Grid E. In fact, for $\alpha=12.86°$, ZAP2D converged for all grids including Grid F; however, as noted above, for $\alpha=14.53$, ZAP2D diverged for Grid E.

Figures 8(a) through 8(c) illustrate the effects of domain size on section lift, C_ℓ, drag, C_d, and moment, C_m, coefficients, respectively. Each data line shows the calculation for a fixed angle of attack. Based on the work reported in Reference 35, ZAP2D is almost independent of domain size for outer boundaries larger than $R_o=5$; consequently, ZAP2D calculations are illustrated in Figure 4 for Grids B-F ($R_o=5$ to $R_o=0.12$). The target values for C_ℓ, C_d, and C_m are then taken as the respective ZAP2D computed values for a domain of 5 chord lengths; i.e., for zero error, each trend line would exhibit no deviation from its initial value.

As shown in Figure 8(a), the deviation of the ZAP2D computed C_ℓ is less than 1% from its target values for low angles of attack and has a maximum of approximately 4% for the high angle-of-attack cases. Again, at $\alpha=14.53°$, ZAP2D diverged for Grid E.

As expected, the computed drag coefficient is more sensitive to domain size. In Figure 8(b), the deviation from its target values is less than approximately 30 drag counts for alphas less than 5°. The deviation for Grid E increases to a maximum of 75 drag counts at $\alpha=12.86°$. This numerical scatter has been traced to small errors in the computation of "near" field velocities adjacent to the outflow

boundary where potential flow panels are quite large. On the other hand, the deviation for Grid C at the higher alphas is caused by small velocity inaccuracies generated by ignoring the near-field computation altogether or by a lack of accuracy in the potential flow solution. Regardless, the computed C_d for the smallest is less than 25 drag counts in error from its target values for all angles of attack.

The domain dependency of the computed C_m, illustrated in Figure 8(c), is quite small (the scale is unusually expanded). For all angles of attack, the variation from target values is less than 0.005.

Figures 9(a) through 9(c) compare the angle-of-attack trends of the ARC2D (Grid A) and ZAP2D (smallest domain) calculations with experimental data[36] for C_ℓ, C_d and C_m, respectively. The ZAP2D and ARC2D angle-of-attack trends are almost identical. Results for the two codes differ by less than 3% in C_ℓ, less than 7 counts in C_d, and less than 0.004 in C_m. Once more, the scale of the pitching moment data in Figure 9(c) is unusually expanded for clarity.

In general, the calculations are in good agreement with experiment, other than at $\alpha = 14.53°$, where the experiment showed a stall phenomenon. It is possible that, by using Harris' formula of $\alpha_c = \alpha_g$ - 1.55 x C_ℓ, too much correction in geometric angle of attack was made in this nonlinear region, which resulted in a smaller angle of attack than the actual stall angle. However, in Figure 9(a), the computed $d(C_\ell)/d\alpha$ is almost flat and the stall may occur just beyond this angle. (Additional calculations revealed that the stall does occur between 15° and 15.5°.) Of course, the uncertainty of the turbulence modeling and the location of transition will influence the stall characteristics. Before the stall, the deviation of calculated C_ℓ from experiment ranges from 1.8% at $\alpha = -1.81°$ to 8.3% at $\alpha = 12.86°$. Evidently, the viscous calculation has not properly represented the actual loss in circulation due to the thickening boundary layer above approximately 12° angle of attack. In Figure 9(b), the computed C_d is approximately 20 drag counts larger than the experimental values for alphas between 4.97° and 12.86°. While approximately 30% of this error might be due to ignoring the laminar boundary layer at the airfoil nose, the remainder must be due to the underprediction of the boundary layer thickness effects. In Figure 9(c) the experimental C_m trend with angle of attack is accurately predicted by ARC2D and ZAP2D up to the stall angle (note expanded scale).

Finally, the drag polar is shown in Figure 10(a) and the pitching moment curve in Figure 10(b). Again, up to the experimental stall angle, the comparison of the computed and experimental values is reasonably good. It should be noted here that an assessment of experimental results for the NACA 0012 airfoil also show significant data scatter[29] which might explain some of the differences in the comparison.

Distributions of pressure coefficient computed with Grid F are shown in Figure 11 and compared with experimental data for a range of angles of attack. As can be seen, the calculations agree very well with experiment at moderate alphas. However, at the higher alphas, the computed pressures are too low compared with those of the experimental data. Again, apparently the boundary layer effects are not simulated exactly. However, all suction and pressure peaks are correctly predicted. Mach contours around the airfoil at $\alpha = 12.86°$ are shown in Figures 12(a) and (b). Figure 12(a) from the ARC2D-alone solution (Grid A) is almost identical to Figure 12(b) from the ZAP2D solution with Grid F. A substantial transonic and supersonic region exists near the leading edge (a maximum Mach number of 1.2) in a region close to the body surface. Although some Mach numbers reach more than 0.5 at the outer boundary, these are local phenomena and the compressibility correction used here is still considered reasonably valid. Figures 13(a) and (b) show pressure contours around the airfoil which agree very well. The normal pressure gradient near the leading edge on the upper surface is very large

and immediately downstream of the trailing edge the normal pressure gradient is negligible. This is true for the range of angles of attack investigated, and is confirmed by the streamline plot in Figure 14 which is calculated using ZAP2D with Grid F at $\alpha=12.86°$. As shown, the streamline curvature effects are important at high incidences near the leading edge and in the wake region where the flow tends to return to the free-stream direction.

The numerical stability and convergence characteristics are shown in Figure 15(a) where the time histories of C_ℓ and C_d are compared for 1,000 time steps for ARC2D (Grid A) and ZAP2D (Grid C). Beyond about 200 iterations, both solutions monotonically converge. The ZAP2D time history demonstrates the reduced magnitude of both C_ℓ and C_d fluctuation levels due to a large reduction of the grid domain. Additional improvement in this behavior was obtained by incorporating an automatic schedule procedure in ZAP2D. In this scheme the first POT2D calculated boundary conditions are not updated until the rate of change of C_ℓ ($\Delta C_\ell/\Delta t$) in the ARC2D solution is less than 0.001. Once the boundary is updated by POT2D, the ARC2D calculation proceeds until $\Delta C_\ell/\Delta t$ in the ARC2D solution is again less than 0.001. This procedure stops when both $\Delta C_\ell/\Delta t$ is less than 0.001 and the L2 norm of the residual in the ARC2D solution is reduced by 3 orders of magnitude from the initial value. A total of four zonal updates results in a significant improvement in the solution history. In the range of 400 iterations, the rate of change of C_ℓ and C_d in the automated procedure is about half that of ARC2D and about the same as that of ARC2D at iteration 700.

Finally, the time history of the L2 norm of residual is compared for ARC2D (Grid A) and ZAP2D (Grid C) in Figure 15(b). The ARC2D simulation shows a reduction of 3 orders of magnitude, whereas the ZAP2D calculation converged to a reduction of about 4 orders of magnitude. It is natural that the ARC2D solution with Grid A should have a larger error of mass conservation than that of the ZAP2D solution with Grid C. Oscillatory behavior is observed in the L2 norm of residual in the ZAP2D calculation and is probably due to machine zero accuracy. Further, in the automatic scheduling, the density residual jumps abruptly at each update due to the sudden change of the boundary values. Although the calculation stopped after the density residual was reduced by 3.5 orders of magnitude, it is possible to allow more iterations to reach a lower residual.

3.1.1.3 Improved CPU Time

For the low angle-of-attack case, a reduction of CPU time by a factor of 4 was reported in previous work.[24] A reduction of grid points by a factor of about 2 and of iterations by the same factor were the result of using the automated zonal update schedule. For high angle-of-attack cases, a similar overall savings in CPU time was achieved. Total execution time on the Titan at $\alpha=12.86°$ is 4,300 seconds for ZAP2D with Grid C and 16,215 seconds for ARC2D with Grid A. The CPU times required in these calculations were 0.00134 seconds/grid point/iteration for ARC2D and 5.5 seconds/iteration for POT2D on the Titan; 0.00080 seconds/grid point/iteration were required for ARC2D and 3.3 seconds/iteration for POT2D on an IRIS workstation.

3.1.2 Mach Number Validation

The objective of this work was to determine the range of applicability of this zonal concept for free stream Mach numbers through 0.84 at angles of attack near the two-dimensional $C_{\ell_{MAX}}$ point. In the following sections, the detailed analysis of the zonal simulation of the flow past an airfoil is compared with the NS alone simulation as well as with experimental data.

3.1.2.1 Grid Domain Cases

A total of eight grid domains have been utilized to study the sensitivity of the ZAP2D zonal concept to domain size with particular emphasis on compressibility effects. A description of the grids and their corresponding case identifiers are included below in Table 2. In this table and throughout this report, R_o is the outer domain radius normalized by chord length. The total number of mesh points ranged from 12,025 (185 x 65) for the largest domain (outer boundary characteristic distance, R_o - 25 chord lengths—Grid A) to 6,919 (187 x 37) for the smallest domain (outer boundary characteristic distance, R_o - 0.1 chord length—Grid H). The upper and lower airfoil surfaces each had 80 grid points for all domains. A total of 12 mesh points was included in the wake region, for Grid A, between the airfoil trailing edge and the downstream boundary at a distance of 25 chord lengths. To allow the use of the simple wake model in ZAP2D, the wake region for Grids B through H was modeled with 14 mesh points spaced from the airfoil trailing edge to a point 5 chord lengths downstream. This downstream boundary location remained fixed for all ZAP2D calculations to minimize the grid variation during the study. Also, the downstream grid spacing was held constant beyond approximately one chord length from the airfoil trailing edge in an effort to minimize errors in the potential flow field velocity calculation. The ARC2D calculations were made exclusively on Grid A and were used as "target" values for the smaller domain, ZAP2D computations which were conducted on Grids B through H. The point vortex correction available in ARC2D[3] was not used in this study. This option has demonstrated a similar domain reduction capability in two-dimensional airfoil applications, but the ZAP2D concept has the advantage of possessing a direct three-dimensional extension.

GRID	MESH SIZE	R_o	$1/R_o$
A	185 x 65	25.0	0.04
B	187 x 57	5.0	0.2
C	187 x 54	3.0	0.33
D	187 x 52	2.0	0.5
E	187 x 48	1.0	1.0
F	187 x 45	0.5	2.0
G	187 x 40	0.2	5.0
H	187 x 37	0.1	10.0

Table 2. Summary of Grid Domains.

3.1.2.2 Validation and Domain Size Effects

Previous numerical studies to validate the basic ZAP2D zonal concept for an airfoil at a fixed, moderate angle of attack at low subsonic Mach number[24] and to extend the validation to a range of angles of attack up to stall were detailed in Section 3.1.1.[25] Further validation of this zonal concept, included here, involves the flow about a NACA 0012 airfoil at Mach numbers 0.3, 0.5, 0.7, 0.8 and 0.84.[26] The angles of attack for each Mach number (see Table 3) correspond approximately to the two-dimensional $C_{l_{MAX}}$ point as defined by the test data of Harris,[27] and as such represent a very challenging set of conditions to test the coupling concept. In fact, it is assumed that these flight conditions will define the expected minimum benefit from this two-dimensional zonal method in terms of CPU time reduction.

Mach Number	Apha (Geometric)	Alpha (Corrected)
0.30	14.86	12.86
0.50	9.86	8.35
0.70	5.86	4.75
0.80	2.86	2.29
0.84	1.86	1.67

Table 3. Summary of Flight Conditions

Since the inner fluid boundary surface, S_i, is to approximate a potential flow surface, care must be taken to ensure that the effects of the transonic flow conditions are minimized. Consequently, the local Mach number was monitored on the inner S_i boundary at periodic intervals in the iteration sequence. If the local Mach number achieved a level of 0.9 anywhere on the S_i boundary, the code would automatically shift the indicial location of S_i outward. For domains too small to satisfy this restriction, the inner S_i boundary was located no closer than two grid contours inside S_o. The choice of a "C" topology, of course, makes this type of adjustment very simple to implement. Further work would include utilizing an arbitrary shape for the inner S_i boundary.

The effects of domain size (Grids A-H) on the computed integrated forces and moment have been thoroughly investigated for fixed ARC2D input parameters. Also, the ZAP2D results presented here include boundary condition updates at every iteration in the viscous/potential flow cycle. The solutions for Mach numbers 0.5 through 0.84 have been assumed converged when the solution residual achieved a third order reduction. The Mach 0.3 results exhibited the "stiffness" associated with low Mach number computations[41] and as a result were assumed converged when the solution residual achieved a fourth order reduction.

Of course, in most cases a combination of force coefficient and residual reduction is a superior means of determining solution convergence. Here, it is only necessary to set some reasonable convergence criteria for comparing two numerical results.

The lift, drag and pitching moment variation with domain size is presented in Figure 16. Again, all calculations presented are at the experimental $C_{t_{MAX}}$ values. The ARC2D "target" solution is the value located at an outer boundary radius of 25 chords ($1/R_o=0.04$). The general trend for the lift variation with domain size (Figure 16(a)) appears to be consistent throughout the Mach number range tested. Some inconsistencies are present in the drag and pitching moment results in the region of Mach 0.5 (Figures 16(b) and (c)). This behavior may be an indicator of the need for grid refinement for each flight condition to obtain optimum shock/boundary layer resolution. However, the validation of the zonal method by means of comparison with two related numerical algorithms is not compromised since the common NS component in ARC2D and ZAP2D is exposed to the same degree of local grid resolution.

The effect of compressibility at these high lift conditions upon the accuracy of the ZAP2D model is clearly shown as the freestream Mach number is varied from 0.3 to 0.84. To maintain the same level of accuracy (as measured by the difference between the ZAP2D integrated force and moment coefficients and the target values), the domain size must increase with increasing freestream Mach number. By requiring a deviation no larger than 3% (in absolute value) from the target value, only a 20% chord domain is needed at Mach 0.3, while at Mach 0.84, a 5-chord domain is necessary (Figure 17). Computing the lift to this accuracy resulted in a range in drag deviation from the target value of roughly 2% (10 drag counts) at Mach 0.84 to 10% (30 drag counts) at Mach 0.3.

A plot of the experimentally determined maximum lift coefficient as a function of freestream Mach number, for the cases considered here, approximates the stall limit for the NACA 0012 airfoil (Figure 8(a)). To verify that the numerical results corresponding to the stall limit, further cases must be examined to determine the computed $C_{\ell_{MAX}}$ point. A 1.67° corrected angle of attack at Mach 0.84 was the largest angle for which a converged (non-oscillatory) ARC2D result was obtained. Similarly, the work described in Section 3.1.1 had determined that the maximum corrected angle of attack at a Mach number of 0.3 is 12.86°. The computed maximum lift at the remaining Mach number points has yet to be verified. Presented in Figure 18(a) are lift results comparing ARC2D results on Grid A (R_o=25) with ZAP2D results on Grids C and G (R_o=3 and 0.2). As indicated, the ARC2D and ZAP2D (Grid C) results compare well with the data from experiment. The Grid G computations are included here to demonstrate the degradation in the small domain solution at the higher Mach numbers. The computed lift coefficient on Grid G at Mach 0.3 is within 2% of the ARC2D target value, while at Mach 0.5, the ZAP2D calculation is greater than 7% in error. It is fortuitous that the computed lift coefficient on Grid G at Mach 0.84 is nearly identical to the experimental value.

Similar conclusions may be obtained when examining the drag and pitching moment variation with freestream Mach number at the flight conditions considered (see Figures 18(b) and (c)). The ARC2D and ZAP2D computed pitching moment coefficients are in close agreement with the data from experiment except at Mach 0.8 and 0.84 (Figure 18(c)). Here, an increased nose-down pitching moment is apparent due to a computed aft shock position as compared with experiment.

Further insight may be gained through examination of some critical flow features at a single flight condition. For this purpose a freestream Mach number of 0.7 and an angle of attack of 4.75° was arbitrarily selected. Contours of local Mach number are presented in Figure 19 for both ARC2D (Grid A) and ZAP2D (Grid C). The comparison between the two computed solutions is quite good for this challenging transonic flight condition. The ZAP2D result used for comparison corresponds to a 3-chord outer domain radius (Grid C), which yielded a lift coefficient within 2.5% of the target ARC2D value. The drag coefficient was computed to within 2.8% (11 drag counts) of the target value.

The distribution of surface pressure coefficient, Cp, computed by ZAP2D for Grid C is compared with values from experiment in Figure 20. Deviations in surface pressure, between ARC2D (Grid A) and ZAP2D (Grid C), were not discernible to the scale shown in this figure. The correlation between ZAP2D and experiment is reasonably good over most of the airfoil with the exception of the shock location and downstream shock/boundary layer interaction region. This type of correlation is similar to that reported by Maksymiuk and Pulliam[12] for the NACA 0012 airfoil at Mach 0.8. Proper analysis of this transonic condition would require grid refinement which was beyond the scope of the present study.

The convergence characteristics are shown in Figure 21 where the time histories of C_ℓ are compared for ARC2D (Grid A) and ZAP2D (Grid C). Previous work at Mach 0.3[24,25] had indicated that the ZAP2D calculation was a stabilizing influence based on comparison of the convergence trends. As indicated here, the convergence history at Mach 0.7 is quite similar for the two codes. The previously observed convergent oscillatory behavior over the first 200 iterations has been replaced by highly damped oscillatory behavior over this time-step domain.

The time histories of the density residual are compared for ARC2D (Grid A) and ZAP2D (Grid C) in Figure 22. The ZAP2D zonal concept demonstrates a faster reduction in residual compared with ARC2D alone. The ARC2D computation has achieved a third-order reduction in residual by iteration 413, while ZAP2D requires only 281 iterations.

3.1.2.3 Improved CPU Time

The initial work presenting the ZAP2D concept[24] had shown a saving in CPU time by a factor of 4 for a low-Mach-number, two-dimensional airfoil computation. This represented a calculation on a grid domain radius of 0.14 chord lengths with an accuracy of 1% in lift when compared with the large domain result (Grid A). The work presenting the validation of this zonal concept at low Mach number for a range of angles of attack up to stall detailed in Section 3.1.1[25] had shown a similar ratio. The results presented here indicate a saving in required CPU time by roughly a factor of 2 for Mach numbers greater than about 0.5 at angles of attack near $C_{\ell_{MAX}}$. In the present study, the ZAP2D zonal concept has demonstrated an increased rate of convergence over ARC2D alone and also a reduction in the grid domain radius from 25 to 3 chords (for Mach 0.8 or less), with less than 3% loss in accuracy.

3.2 Three-Dimensional Fixed Wing Validation

The objective of this work was to extend the previously documented two-dimensional zonal concept to three dimensions and to validate the technique for an aspect ratio 5 rectangular wing consisting of NACA 0012 airfoil sections. The following sections detail the validation process and include comparisons between ZAP3D, ARC3D and available experimental data.[31]

3.2.1 Grid Domain Cases

A total of six grid domains have been utilized to study the sensitivity of the ZAP3D concept to domain size for a rectangular wing at a single flight condition. A description of the grids is included in Table 4 below.

GRID	MESH SIZE	R_o	$1/R_o$
A	100 x 39 x 23	16.78	0.06
B	100 x 39 x 20	3.41	0.29
C	100 x 39 x 19	2.00	0.50
D	100 x 39 x 18	1.18	0.85
E	100 x 39 x 17	0.69	1.45
F	100 x 39 x 16	0.41	2.44

Table 4. Summary of Grid Domains.

The total number of mesh points ranged from 89,700 for the largest domain outer boundary characteristic distance (R_o - 16.78 chord lengths—Grid A) to 62,400 for the smallest domain (R_o - 0.41 chord length—Grid F). The upper and lower airfoil surfaces each had 80 grid points for all domains, based upon a C-O topology (see Figure 7).

3.2.2 Validation and Domain Size Effects

To validate the implementation of the ZAP3D coupling concept, a very detailed investigation of the induced velocity components on S_i, the resultant potential solution on S_i, and the induced velocity updates at S_o are required. An artificial potential flow only zonal loop was constructed as utilized in the earlier two-dimensional work in order to validate the accuracy of the potential flow off-body velocity calculation and the transpiration based coupling technique. By utilizing this method, special near-field (scan points that fall within a panel characteristic dimension) velocity parameters that are inherent in the VSAERO velocity scan procedure were sized to limit any induced velocity error to less than 1% for the expected S_o and S_i relative grid densities.

As discussed earlier, since the "wake extension" of the S_i boundary includes no source terms, the outflow boundary should theoretically be located far enough downstream such that ARC3D obtains nearly freestream conditions on S_i at this location. However, for outflow boundaries located far away, the wake will eventually impact S_i or even S_o for onset flows at non-zero angles of attack. A comparison of the velocity components on S_i as computed by ARC3D and the standard ZAP3D simulation (Figures 23(a) and (b)) indicates the effect of wake impingement on the coupling surfaces. This condition violates the potential flow approximation of the ZAP3D zonal concept at S_i. Consequently, the computed ZAP3D wake behavior is completely incorrect. That is, ARC3D information involving the wake deficit is passed to the S_i boundary in the form of a normal velocity boundary condition only, and there is no mechanism in the current model to accurately transmit any vorticity delay information via a potential flow surface to the outer boundary S_o.

Furthermore, because the grid density is not maintained to capture the wake correctly for the entire distance downstream, numerical diffusion will certainly lead to errors in the Navier-Stokes velocities on the S_i boundary. While not thoroughly investigated here, such local errors apparently may not significantly affect the computed wing forces and moments in the ARC3D-alone simulations, but can drive the ZAP3D simulation to a different converged result because of the potential flow update of the boundary conditions at S_o.

One technique that can be utilized to minimize the wake-impingement problem is to align the downstream grid with the freestream direction. This, however, would require rotation and redistribution of the grid for each angle of attack. Clearly, other more practical corrective measures that do not involve such geometric changes are preferred.

The technique adopted here, which avoids modification of the volume grid, is to shorten the downstream extent of the effective S_i boundary while maintaining the entire S_o boundary. Of course, as S_i is shortened, the "wake extension model" which is required in ZAP3D is also brought forward within the S_o domain. This modification avoids the problems associated with the wing wake impingement on S_i. It does, however, imply some additional error of unknown but probably small magnitude, since the "wake extension" of S_i does not presently include any source term that should be required to continue ARC3D disturbances from freestream conditions at the S_i terminus. A comparison of the ARC3D and ZAP3D velocity components with the shortened S_i surface (Figures 24(a) and (b)) indi-

cates a substantial improvement in the streamwise velocity component. The vertical component shows some improvement over the wake region, but is slightly worse near the airfoil trailing edge station (note the scale differences between Vx/a and Vz/a). For the present case, evidently the potential errors due to the neglect of any source terms on the wake extension appear to be small; therefore, this method has been incorporated in all the calculations presented below.

As previously mentioned, domain size effects for ZAP3D and ARC3D were obtained over a range of R_o values from 16.78 to 0.441 chords (see Table 4). A single flight condition of $\alpha=8.75°$, Mach 0.12 and R_e 1.2 million was examined for an aspect ratio 5 rectangular wing.[31] The ZAP3D simulation consisted of potential flow outer boundary velocity updates at every 250 ARC3D iterations. The S_i boundary was located a distance of 0.14 chord from the wing for all ZAP3D calculations ($l=14$). Furthermore, based on the previously described wake impingement study, the inner S_i boundary was shortened to a location just beyond the wing trailing edge (x/c=1.02, j=85). All of the ZAP3D and ARC3D calculations achieved a residual reduction of 3-4 orders.

Figure 25(a) illustrates the ZAP3D and ARC3D lift variation with domain size. As indicated by the greatly expanded vertical scale in this figure, the ZAP3D three-dimensional lift C_L for $R_o=0.69$ ($1/R_o=1.45$, Grid E) is less than 3% higher than the target ARC3D C_L with $R_o=17$. In this case, the shortened S_i in ZAP3D is very effective in maintaining the ARC3D target C_L for reduced domain size. Still, based on the two-dimensional results,[25] which indicated less than 2% error in $C\ell$ for R_o values as low as 0.14 chords, smaller domain sizes than achieved here should be possible. It may be that the three-dimensional wake impingement on S_o that still occurs in these calculations is limiting the amount of domain reduction that is possible for a given error limit. Further studies of the effects of the downstream location of the outflow boundary and the grid density in the wake region should be investigated as a possible source of error that was not present in the two-dimensional simulations. Figures 25(b) and (c) illustrate the computed drag coefficient (C_D) and pitching and moment coefficient (C_{My}) variation with domain size. As illustrated, for ZAP3D domain size reductions down to 1 chord length, there are fewer than 10 counts variation in C_D and less than 0.0015 change in C_{My}.

Because it exhibits the least error of the smaller domains in the computed C_L compared with the ARC3D target value (less than 0.5% error), the ZAP3D result at an outer radius of 1.18 chords (Grid D) was selected here for further detailed analysis. A comparison of the symmetry plane chordwise pressures between the large domain ARC3D result ($R_o=17$) and the ZAP3D calculation is presented in Figure 26. There is no discernable difference to plotting accuracy in the two simulations. The computed spanwise loading distributions by ARC3D and ZAP3D are compared with the wind tunnel data in Figure 27. Again, the ARC3D and ZAP3D results are nearly identical and compare very well with the experimental data. The history of solution residual for the ARC3D large domain and ZAP3D small domain is presented in Figure 28. The spikes in residual for the ZAP3D calculation are associated with the outer boundary velocity update (potential flow update every 250 ARC3D iterations). The relative improvement in residual reduction over ARC3D is due to the reduced distance over which information must travel. These phenomena were also noted in the two-dimensional work,[24] Section 3.1.

The history of total lift coefficient is shown in Figure 29. The improvement in C_L convergence over the first few hundred iterations that was noted in the two-dimensional work is not apparent here. Additional ARC3D large domain data points are required to be conclusive, since there is lift coefficient information only at every 250th iteration.

As noted earlier, the final deviation in lift coefficient between ZAP3D ($R_o=1.18$ Grid D) and ARC3D ($R_o=17$ Grid A) is less than half a percent. To demonstrate the importance of multiple viscid/inviscid iterations, an ARC3D calculation that is initialized with the potential flow solution is shown in the inset in Figure 29. As illustrated, the ARC3D lift coefficient, given a potential flow

initial condition, deviates from the multiple update ZAP3D calculation (and ARC3D large domain) by about 3%.

Finally, a comparison between the ZAP3D computed pressure coefficient and the values from experiment[31] are presented in Figures 30(a), (b), (c) at inboard, mid, and outboard wing span locations. Overall, the comparisons in the pressure distributions are quite good.

3.2.3 Improved CPU Time

A general statement regarding the saving in CPU time by the three-dimensional zonal method is premature at this time. The outflow boundary location and downstream grid density effects on the reduced domain calculations need to be further investigated to achieve the minimum grid domain sizes that should be possible. Furthermore, higher angles of attack and higher Mach numbers need to be studied before the issue of CPU time is resolved.

Nevertheless, based upon the convergence behavior shown in Figures 28 and 29, the current ZAP3D calculation at an outer domain radius of 1.18 chords represents a speed-up in CPU time over the ARC3D large domain calculation by a factor of about 2.5. This improvement is obtained for less than a 0.5% deviation in C_L, 10 counts change in C_D, and 0.0015 variation in C_{M_y}. Since the two-dimensional studies achieved a speed-up by a factor of 4, it is expected that further reductions in the required computational domain size can be achieved with sizable improvements in CPU time.

3.3 Three-Dimensional Wing/Vortex Validation

To validate the scheme for vortex-induced lift on a wing, a simple numerical calculation was made. A vortex-generating wing (aspect ratio 5) with a NACA 0012 airfoil section was mounted vertically with 8° of yaw and located upstream of a horizontally-mounted wing. This downstream wing was geometrically identical to the upstream one, but was set at zero angle of attack. Other flow conditions were M=0.12 and Re=1.5 million, based upon the chord length. The flow on the investigated wing was assumed to be fully turbulent and the Baldwin-Lomax algebraic turbulence model was used for turbulence closure. Figure 31 shows a typical location and shape of the far boundary surrounding the wings (R_o=18).

As explained in Section 2.3, the upstream wing and shed tip vortex will modify the boundary conditions at S_o. Various outer domain boundaries were investigated in order to test the ability to capture these effects within ARC3D. After some study of boundary locations, five different domain sizes were thoroughly investigated, with boundaries ranging from a large radius outer boundary which completely encloses the wings (R_o=5.8) to a small radius outer boundary just outside the investigated wing (R_o=0.08). Up to about 90,000 grid points were used for the largest domain with 98 points along the streamwise direction, 43 points along the spanwise direction, and 21 points in the normal direction. Smaller domains were achieved by removing outer layers of the C-type grid. In all domain sizes studied, the downstream exit boundary remained at a fixed location. At this exit boundary, conditions are internally computed from ARC3D.

Figure 32(a) illustrates the computed spanwise lift coefficient of the downstream wing for the respective outer boundaries. The computed span loadings illustrate the effect of the upwash and downwash induced by the tip vortex located at Y=2.0 (80% of span length) and Z=0.5. Among five

ARC3D/VSAERO solutions, only two—with the outer boundary at R_o=0.4 and 0.24—are regarded as valid because only these two show reasonable comparisons with the VSAERO-alone solutions. The solution with R_o=0.08 apparently has the boundary too close to the viscous region around the investigated wing. The cases with R_o=0.68 and 5.8 contain the tip vortex within the domains, but the vortex effects were not properly accounted for in the calculations because of numerical diffusion due to the course grid density for these larger domains. Clearly, if the vortex is present within the calculation domain, the grid should be dense enough to capture the vortex from the outer boundary condition and maintain its effect without dissipation, or it should be modeled as a potential prescribed vortex filament which is carried throughout the domain.

In another study to thoroughly resolve the differences obtained with ZAP3D and ARC3D initialized by VSAERO for the vortex/wing interaction test case, the velocity updates at the S_o boundary were replaced with an exact line vortex calculation. In this way, any numerical errors arising in the ZAP3D/VSAERO updates associated with the boundary velocities would be eliminated, and the ARC3D simulation could then be investigated for grid convergence. Again, the NACA 0012 wing was utilized with a vortex of known strength passing above the wing. The wing had a chord of 1 and a semispan of 2.5, and the infinite line vortex was located at Y_V, Z_V = (2.0, 1.5). The vortex strength was arbitrarily set to Γ=0.5, and symmetry conditions were enforced on the X-Z plane. Further, the wing angle of attack was set to zero so that any lift was entirely induced by the influence of the line vortex.

Figure 32(b) illustrates the computed spanwise lift coefficient for several grid cases. The VSAERO calculation is also shown for comparison and is considered the target solution, because a potential flow approximation should accurately model this particular case. Although the figure includes calculations for two different domain sizes (R_o=1.02 and R_o=1.7), grid density studies have been completed only for the R_o=1.7 boundary. In this case, the vortex penetrates the NS domain between S_i and S_o. Furthermore, for all calculations, the vortex influence is included as velocity boundary conditions at S_o only. With R_o=1.7, three different grid densities were used to calculate the flow (98 x 39 x 19, 98 x 39 x 31, and 98 x 38 x 51). In the denser grid cases, grid lines were added between the ℓ=19 and ℓ=18 surfaces such that the tip vortex passing between two surfaces could be more accurately resolved. The comparison with VSAERO shows that in the original grid (98 x 39 x 19) sectional lift was overpredicted on the inboard wing and underpredicted on the outboard wing. In this case, the vortex effects are incorrectly dissipated within the viscous solution. In the latter two grids, there is less than a 3% variation in the spanwise lift. Because the spanwise lift also compares very well with VSAERO for these two cases, the viscous effects are believed to be correctly captured. Hence, if the grid density near the vortex is sufficient, ARC3D can successfully simulate the vortex/wing interaction where the vortex penetrates S_o, and the vortex effect is provided by velocity boundary conditions on S_o only. For the rotor cases, this ability is a requirement in order to utilize the ZAP3D concept.

3.4 Hover Rotor Validation

3.4.1 A Nonlifting Rotor Case

The nonlifting flow may be considered self contained when the flow field at the outer boundary, S_o, lies undisturbed. In order to achieve this state, the outer domain, S_o, should be located at least 10 times the chord length beyond the rotor. Then, it is sufficient to impose the rotational freestream

boundary condition at the S_o boundary without using any externally provided boundary conditions; thus, NS alone calculations are possible. Because of the axisymetric flow, periodic boundary conditions (see Section 2.4.3), are imposed and the calculations are performed for only one blade. The grid at the inlet and exit planes maintains the exact symmetry and no interpolation was required to swap the flow variables in these planes.

As a preliminary case to verify the rotor simulation, calculation of a nonlifting, two-bladed, aspect-ratio-6 rotor with a NACA 0012 section was carried out. Experimental data[14] and other NS calculations[15-18] are available for a tip Mach number of 0.52, and a Reynolds number (based on the tip speed and chord) of 2.32 million. At this Reynolds number, the flow region on the surface can be regarded as turbulent over the entire blade. For a viscous calculation, a domain size of $R_o=20$ with about 125,000 grid points of 91 points along the streamwise direction (40 points on the blade), 39 points along the spanwise direction, and 35 points along the normal direction were used. A partial view of the grid generated is shown in Figure 33.

A typical ARC3D solution for the Cray-2 required about 2,000 time steps to reduce the residuals by 0(-3) with a CPU time per time step per grid point of 35 ms. The time step of 1.00 was used with the Jacobian correction to accelerate the convergence to steady state. The maximum CFL number corresponding to the step size was 1.7. The calculated pressure coefficients, based upon the sectional dynamic pressure, are shown in Figures 34(a) through 34(e), and compared with the experiment. Although relatively coarse grid was used—compared with those in other similar calculations—results are in very good agreement. Consequently, the modifications to ARC3D for the rotor simulation are correct for this case, and the more interesting lifting case could be investigated with the ZAP3D zonal coupling.

3.4.2 A Lifting Rotor Case

The HOVER program installation on Unix machines and its modifications were verified by comparing the wake geometry and integrated performance for an untwisted, rectangular planform, two-bladed model rotor of aspect ratio 13.7, which was reported in Reference 14. The measured wake geometry data was reported to be in agreement with the prescribed wake equations of References 18 and 19. Hence, the calculated wake geometry should remain relatively fixed during the relaxation iterations in the HOVER module.

In the HOVER initial solution, the full wake was relaxed and calculations were started with Landgrebe's prescribed wake geometry. The computed collective was adjusted to obtain a thrust coefficient equal to that measured in the test. The computed wake geometry converged to a unique position regardless of the starting geometry.

Figures 35(a) and (b) compare the measured and calculated tip vortex geometry for five relaxed wake iterations for $C_T=0.0037$. The calculated geometry is well within the scatter of the experimental data,[11] and there is very little movement of the tip vortex through the relaxation iteration. Figure 36 illustrates several constant azimuthal cuts through the inner sheet and tip vortex for the last relaxed wake iteration. For $\psi=90°$ and 180°, there are no differences in these geometries when compared with the second relaxation iteration. Moreover, the inner sheet does remain linear as expected with only a slight roll-up indicated at the outboard end where the vorticity is extremely weak.

The measured trend of thrust coefficient, C_T, with collective, Θ_{75}, and torque coefficient, C_Q, is also predicted quite well as shown in Table 5.

MEASURED			PREDICTED		
θ_{75}	C_T	$C_Q \times 10^3$	θ_{75}	C_T	$C_Q \times 10^3$
5 ± ½°	.0018	.109	5.2°	.0018	.117
8 ± ½°	.0037	.253	8.5°	.0037	.250
12 ± ½°	.0056	.493	12.1°	.0056	.439

Table 5. Detailed Comparison of Measured and Calculated Hover Performance for the Ames Untwisted Rotor.

The difference in the C_Q for the 12° case is probably due to separations that occur at the lower test Reynolds number. The corresponding performance map comparison is shown in Figure 37 where the usual ±2% experimental error band on C_T for fixed C_Q has been applied. These results verify the accuracy of the Unix installation and modifications of the HOVER code.

As noted earlier, the coupling of the HOVER module within ZAPR3D is essential in order to complete the rotor simulations. In ZAPR3D, the HOVER module must first provide the converged rotor blade loads and associated rotor wake vorticity and geometry. Again, since the vortex-lattice method inherently includes an infinite computational domain, this computed rotor flow field should facilitate large reductions in the required viscous computational domain. The HOVER module then passes boundary condition information to the ARC3D rotor module by velocity scans at appropriate off-blade boundaries. Specifically, the entire HOVER flow field is utilized to compute the initial S_o boundary conditions for ARC3D while the HOVER flow field outside of S_i is utilized to provide a part of the S_o boundary conditions for continued ZAPR3D iterations. During the ZAPR3D iterations, the completion of the boundary condition updates at S_o are accomplished by velocity scans due to the ZAP potential flow representation of the inner surface coupling boundary, S_i.

In order to complete this work, the procedure for sharing S_i and S_o boundary information was generalized for the C-H grid topology used for the rotor simulation. Whereas the S_i boundary for the wing cases were transmitted by specifying a single constant-ℓ surface, the rotor case require transmitting several restricted grid surfaces. Additionally, a general procedure was also designed and coded to identity the HOVER wake intersections with S_i and the portions of the wake contained within the S_i volume. With the geometric work complete, a generalized velocity scan procedure was written for the HOVER module that would automatically compute both of the required ZAPR3D velocity updates at S_o. Figure 38 compares the HOVER velocity scans at a ZAPR3D boundary located just upstream of the primary blade for the rotor case that is described below. The downwash predicted by HOVER for the entire flow field is illustrated in Figure 38(a), while Figure 38(b) illustrates the downwash for all influences outside of the S_i volume. As expected, there is a reduction in the downwash due to the elimination of the wake effects within S_i. While no comparisons with experimental data are possible for such a velocity decomposition, detailed analysis of several rotor calculations have been utilized to confirm the HOVER velocity scan routine.

With the HOVER velocity scan module complete, lifting rotor simulations by the modified ARC3D program and ZAPR3D could be researched. The test case for these viscous calculations is the same rotor that was investigated in the nonlifting ARC3D simulations. Numerical calculations for the hover condition are presented for a single collective setting of 8 degrees, a tip Mach number of 0.44, and a Reynolds number (based on tip speed) of 1.92 million. These conditions correspond to the available experimental test conditions. Again, in all calculations, the flow on the surface was assumed to be fully turbulent and the Baldwin-Lomax algebraic model was used for turbulence closure.

While ARC3D only calculations cannot be obtained for the lifting rotor case, a preliminary ARC3D calculation that utilized periodic boundary conditions at the inlet and exit planes and HOVER provided boundary conditions at the far boundary located below the rotor was investigated in order to provide a baseline for the ZAPR3D simulations. For this purpose, a grid of an ellipsoidal shape (minor axis along the rotational axis) was generated with 91 points in the rotational stream direction, 39 points in the radial direction, and 35 in the normal direction to the blade surface. As usual in the work reported here, the normal grid spacing was clustered near the blade in order to achieve y+ values of 0(1) for the grid points just off the surface. Because this rotor has two blades, the grid includes a total azimuthal angle sweep of 180 degrees. Also, in order to avoid interpolations of flow quantities at the periodic planes, wakecut planes at upstream and downstream locations with respect to the blade surface grid, which is itself at 8 degrees incidence, were gradually elevated and lowered respectively to match grid points at inlet and exit boundaries. Of course, this grid generation scheme is only required for calculations using periodic boundary conditions. For general boundary conditions which are employed for other lifting calculations illustrated here, please refer to Section 2.4.3.

This large domain ARC3D calculation with periodic/HOVER boundary conditions achieved 0(3) residual reduction in 2000 iterations. While convergence was obtained, the grid was apparently too sparse throughout the volume to accurately resolve the entire flowfield wake effects, since the calculated blade pressure distribution did not reflect the wake induced downwash or blade passage effects correctly. Figure 39 illustrates a typical chordwise pressure distribution (Cp's are based on the sectional onset flow dynamic pressure) comparison with the experimental data (and another calculation discussed later). As shown in this figure, the periodic/HOVER boundary condition solution does not compare very well with the data on the upper surface and also behaves poorly at the trailing edge.

Rather than pursue vastly increased grid density that is required to resolve the wakes for the full 180 degree domain, a reduced zone grid (Zon1) was generated that encloses the primary blade with upstream and downstream boundaries located approximately 1 chord ($R_o=1$) from the leading and trailing edges respectively. The grid included a mesh density of 89x39x35 for a total of about 121,000 points. A view of several selected planes for the Zon1 grid is shown in Figure 40. In this case, ZAPR3D is used for the simulation but no inside potential flow updates from S_i are requested (i.e., ZAPR3D (ITI=0)). In this way, the HOVER solution provides the velocity conditions at all boundaries for a single ARC3D converged simulation. The computed chordwise pressure coefficient at the 68% radius is illustrated in Figure 39. Comparison with the experimental data is very good at this location and is clearly much improved over the periodic boundary condition case. The trailing edge behavior of this computation is also improved over the earlier result; however, comparisons with the experimental data at other locations indicate that the wake effects, while improved, are still not completely resolved. This is illustrated in Figure 41 which compares the ZAPR3D (ITI=0) and HOVER computed radial distributions of the section thrust coefficient. Since the HOVER simulation compares accurately with the experimental data (CT=0.0048), the passing tip vortex effects have clearly not

been captured correctly in the viscous calculation. It also appears that conditions near the root may need to be improved as well.

In order to capture the tip vortex correctly, a new grid (Zon2) was generated, and the full ZAPR3D simulation utilized. A perspective view of the new zone boundaries for the coupled calculation is shown in Figure 42 while a quantitative display of the relative positions of the inner and outer boundary surfaces are shown in Figure 43. In this case, the outer boundary is located approximately 2 chord lengths from the blade (R_o=2) and the inner boundary approximately 1 chord length. For this new grid, Zon2, the grid density has increased to 89x79x55 for a total of about 387,000 points, or just over three times that used in Zon1. The radial density in Zon2 on the inboard half is the same as that used in Zon1 but the outboard half density is much finer. Further, since the tip vortex trajectory was already known from the HOVER calculation, the grid density in Zon2 was increased in this region. A smaller geometric expanding progression was also used in the normal direction for Zon2. Finally, the wake cut distances at both the root and tip were maintained in the hope of improving the solution near the root.

Two ZAPR3D simulations have been undertaken for this fine grid domain. First, a calculation that includes no inside loop updates, ZAPR3D (ITI=0), was completed and required 2500 viscous iterations to achieve 3 orders reduction in residual. Second, a calculation that includes an inner surface potential flow update every 250 iterations, ZAPR3D (ITI=7), was started and continued for approximately 1700 viscous iterations before running out of the requested computer time. Unfortunately, this calculation had achieved a residual reduction of only 2 orders at this time and because of time constraints has not been continued at this time. Figure 44 illustrates the convergence history for these two cases for the first 2000 viscous iterations. Comparison of these characteristics with those obtained in the 2D and 3D wing calculations indicate that while the inner surface zonal update is being correctly modeled, the domain size needs to be further reduced in order to demonstrate the convergence trend that should be expected. Since the rotor case requires the relative comparison between ZAPR3D solutions rather than the comparison between small domain ZAP3D and large domain ARC3D solutions that were possible in the fixed wing simulations, the current trend reported in Figure 44 should be expected until the domain size is much smaller.

Figure 45 compares the HOVER, ZAPR3D (ITI=0), and ZAPR3D (ITI=7) predictions of the radial thrust loading. Clearly, the ZAPR3D (ITI=7) solution is not yet converged as noted above and will undoubtably match the ZAPR3D (ITI=0) solution when finished. Furthermore, the ZAPR3D results for the increased grid density has more correctly captured the rotor wake effects than those reported in Figure 41. The ZAPR3D (ITI=0) maximum sectional thrust value does compare favorably with the HOVER value but the peak value is located further outboard in the viscous case. Additionally, the ZAPR3D loading near the root indicates that the boundary conditions imposed there may not yet be consistent with the HOVER simulation. These differences and the radial slope change in the ZAPR3D thrust loading at the mid-radius location may be due to abrupt grid distribution changes. More detailed grid studies will need to be investigated in order to resolve these issues.

Finally, Figure 46 compares the converged ZAPR3D (ITI=0) computed pressure distribution for this rotor with the experimental data. Again, it is expected that for this domain size, the completed inside loop simulation, ZAPR3D (ITI=7), will produce essentially the same computed pressure distributions illustrated here. Clearly, the wake effects are more correctly captured in this calculation than the earlier simulations (compare with Figure 39). In fact, this calculation compares very favorably with the experimental data with the exception of the suction peak near the root and the pressure on the

suction side near the trailing edge at the 98 % radius location. This later trend is most likely due to the tip edge vortex that will probably require additional grid refinement.

Future ZAPR3D work should concentrate on detailed grid refinement studies and systematic reductions in the outer boundary domain size. Undoubtably, such studies would remove some of the limitations of the simulations obtained so far and would also facilitate the detailed validation of the effectiveness of the inner boundary updates to capture the rotor wake effects. Once this baseline work is complete, full hover rotor performance map correlations should be completed for a variety of rotors in order to substantiate the promise of computational improvements due to the ZAPR3D coupling concept.

4.0 CONCLUSIONS

The primary objective of this work was to demonstrate the feasibility of a new potential/viscous flow coupling procedure for reducing computational effort while maintaining solution accuracy. The success of such a procedure should allow for more exact viscous simulations for simple geometries on a workstation environment and full helicopter configurations on current super computers. In this zonal procedure, the flow field is partitioned into zones which utilize approximate equations appropriate to the flow physics within each zone. The coupling concept is based on the premise that any computational method can only produce valid results within the approximations of the physical model employed in its construction. Therefore, the interfacing boundary surface between the potential and viscous flow code domains must be very nearly potential in order to achieve a successful (accurate) result. This is accomplished in the current technique by requiring that beyond the first iteration the potential flow surface panel strengths are obtained from the NS solution at a smooth inner fluid boundary. These fluid surface panel values are then used to compute the outer velocity boundary conditions for the NS calculation. The iteration between the potential flow solution and the NS solution continues in a closed loop until flow convergence, or allowable iteration limits, are obtained.

This closed-loop, overlapped, velocity-coupling concept has been developed in a new two-dimensional code, ZAP2D (Zonal Aerodynamics Program-2D), a three-dimensional code for wing analysis, ZAP3D (Zonal Aerodynamics Program-3D), and a three-dimensional code for isolated helicopter rotors in hover, ZAPR3D (Zonal Aerodynamics Program for Rotors-3D). ZAP2D couples a simple airfoil panel code, POT2D, with the airfoil Navier-Stokes code, ARC2D. Similarly, ZAP3D couples a modified version of VSAERO with ARC3D. Finally, ZAPR3D, couples the modified version of VSAERO with the lifting surface HOVER code and the ARC3D code that has been modified to include rotational effects. The current status and findings for each of these programs are briefly summarized below.

Detailed results developed and obtained under this contract for ZAP2D applied to a NACA 0012 airfoil at low angle of attack was reported in Reference 24. In this report, studies for a range of angles of attack and Mach number are thoroughly discussed. Computational effects of grid domain sizes from 25 to 0.10 chord lengths have been investigated for a NACA 0012 airfoil with ZAP2D. Comparisons with large domain ARC2D solutions and with experimental data have shown that the required domain size can be reduced to a few tenths of a percent chord for the low Mach and low angle of attack cases and to less than 2-5 chords for the high Mach and high angle of attack cases while maintaining solution accuracies to within a few percent. The smaller domain sizes result in a reduction in the required number of grid points and also a reduction of the number of required iterations for a converged solution; consequently, at this stage of the development, ZAP2D has demonstrated CPU reductions by factors of 2-4 compared with ARC2D.

Future enhancements to ZAP2D should include an automated procedure to determine the optimum location and shape of the inner and outer coupling boundaries. Such improvements in ZAP2D should routinely provide a reduction in CPU requirements for all cases by a factor on the order of 4 compared with the N-alone simulation.

Detailed calculations by ZAP3D and ARC3D have been investigated for a rectangular planform wing of aspect ratio 5 with NACA 0012 airfoil sections. All calculations included a freestream angle of attack of 8.75°, a Mach number of 0.12, and a Reynold's number of 1.5 million. In this work, grid domain sizes from 17 chord lengths to 0.41 chord lengths have been studied. Converged values for C_L, C_D, and C_{My} were obtained from the large domain (R_o=17) ARC3D calculation and served as

target values for the ZAP3D simulations for reduced grid domain sizes. Current calculations show that the grid domain size for ZAP3D can be reduced to 0.7 chord lengths with less than a 3% error in C_L compared with the large domain ARC3D result. Additional reductions in the required computational domain for ZAP3D are expected as the method is further developed and refined. Nevertheless, the current ZAP3D calculation for an outer domain radius of about 1.2 chords represents a speed-up in CPU time over the ARC3D large domain calculation by about a factor of 2.5. This improvement is achieved for less than a 0.5% deviation in C_L, 10 counts change in C_D, and 0.0015 variation in C_{My}.

Future work with ZAP3D should address modeling improvements in the downstream wake region in order to further reduce the domain size requirement and improve the computational efficiency of the code. Higher angle of attack and Mach number cases also need to be investigated before the overall effectiveness of the zonal coupling procedure utilized in ZAP3D can be validated.

Preliminary hover calculations with ZAPR3D have been completed for a two-bladed, rotor with a NACA0012 airfoil and an aspect ratio of 5. As noted above, ZAPR3D combines methodology from ZAP3D (potential flow updates at the inner boundary surface, S_i), HOVER (lifting surface hover method to initialize the rotor solution and to provide the wake and secondary blade influences that are outside of S_i), and a modified ARC3D (viscous solution within the outer domain, S_o). The addition of the rotational flow terms to ARC3D were validated by comparison with experimental data for the non-lifting hover case. As shown in this report, computed and experimental chordwise pressure distributions are comparable for the non-lifting case. Coupled ZAPR3D calculations for a lifting case with a collective setting of 8 degrees have included selected domain sizes from approximately 10 chord down to 1 chord lengths. While a full 180 degree azimuthal grid calculation with periodic boundary conditions was not able to capture and maintain the full wake effects and did not achieve a favorable comparison with experimental pressure data, a ZAPR3D simulation for a fine grid restricted to a reduced domain of about 2 chord lengths was able to capture the wake effects and did compare accurately with the experimental pressure data. Current preliminary comparisons of the radial thrust loading computed by HOVER and various ZAPR3D calculations show good agreement in the maximum thrust loading due to the tip vortex passage but indicate that this peak value is located further outboard in ZAPR3D than in HOVER. Furthermore, the ZAPR3D loading near the root also indicates that the boundary conditions imposed there may not be consistent with the HOVER simulation. Comparisons of the residual history for a ZAPR3D simulation with no inside loop updates (ITI=0) and a ZAPR3D simulation with inside updates every 250 iterations (ITI=7) illustrate that the inner surface updates are correctly modeled but also indicates that the domain size needs to be reduced considerably in order to demonstrate the convergence improvement that is found in the ZAP3D wing simulations. Until this additional work is complete, estimations of any reductions in computational effort cannot be made.

Future ZAPR3D work should concentrate on the detailed validation of the effectiveness of the inner boundary updates to capture the rotor wake effects and to systematically reduce the required outer boundary domain size. Once this baseline work is complete, full hover performance map correlations should be completed for a variety of rotors in order to substantiate the promise of computational improvements due to the ZAPR3D coupling concept.

Acknowledgements

The work reported here was initiated under NASA SBIR Contract NAS2-12961 and supported under NASA SBIR Phase II Contract NAS2-13194. Some computing time was contributed by Cray Research, Inc. The authors would also like to thank their colleagues and staff at Analytical Methods, Inc.

5.0 REFERENCES

1. Flores, J. and Chaderjian, N.M., "The Numerical Simulation of Transonic Separated Flow About the Complete F-16A", AIAA-88-2506, June 1988.

2. Wake, B.E. and Sankar, L.N., "Solutions of the Navier-Stokes Equations for the Flow About a Rotor Blade", *J. Am. Hel. Soc.*, April 1989.

3. Pulliam, T.H., and Steger, J.L., "Implicit Finite Difference Simulations of Three-Dimensional Compressible Flow", AIAA-78-10, 1978.

4. Maskew, B., "Prediction of Subsonic Aerodynamic Characteristics: A Case for Low-Order Panel Methods", *J. Aircraft*, Vol. 19, No. 2, February 1982.

5. Lamb, H., *Hydrodynamics*, 6th Ed., Dover Publications, New York, 1945.

6. Morino, L., "Unsteady Compressible Potential Flow Around Lifting Bodies Having Arbitrary Shapes and Motions", TR-72-01, Boston University, June 1972.

7. Shapiro, A.H., *Compressible Fluid Flow, Vol. 1*, The Ronald Press Co., New York, 1953.

8. Pulliam, T.H., Jesperson, D.C. and Childs, R.E., "An Enhanced Version of an Implicit Code for the Euler Equations", AIAA-83-0344, 1983.

9. Pulliam, T.H., and Steger, J.L., "Recent Improvements in Efficiency, Accuracy, and Convergence for Implicit Approximate Factorization", AIAA-85-0360, 1985.

10. Pulliam, T.H., "Efficient Solution Methods for the Navier-Stokes Equations", Lecture Note for the von Karman Institute for Fluid Dynamics Lecture Series titled, *Numerical Techniques for Viscous Flow Computation in Turbomachinery Bladings*, von Karman Institute, Rhode-St.Genese, Belgium, The Netherlands, 1985.

11. Baldwin, B.S., and Lomax, H., "Thin Layer Approximation and Algebraic Model for Separated Turbulent Flows", AIAA-78-257, 1978.

12. Maksymiuk, C.M., and Pulliam, T.H., "Viscous Transonic Airfoil Workshop Results Using ARC2D", AIAA-87-0415, 1987.

13. Cordova, J.Q., "VisualGrid, A Software Package for Interactive Grid Generation", Presented at AIAA 21st Fluid Dynamics, Plasma Dynamics and Lasers Conference, Seattle, WA, June 18-20, 1990.

14. Caradonna, F.X., and Tung, C., "Experimental and Analytical Studies of a Model Helicopter Rotor in Hover," *NASA TM-81232*, September 1981.

15. Srinivasan, G. R., and McCroskey, W. J., "Navier-Stokes Calculations of Hovering Rotor Flow Fields", *J. of Aircraft*, Vol. 25, No. 10, October 1988, pp. 865-874.

16. Srinivasan, G.R., Baeder, J.D., Obayashi, S., and McCroskey, W.J., "Flow Field of a Lifting Hovering Rotor—A Navier-Stokes Simulation", *NASA TM 102862*, August, 1990.

17. Agarwal, R. K., and Deese, J. E., "Navier-Stokes Calculations of the Flow Field of a Helicopter Rotor in Hover, "AIAA-88-0106, 1988.

18. Aoyama, T. et al, "Navier-Stokes Analysis of Blade Tip Shape in Hover", Paper No. I.4.1.1, *Proc. of the Sixteenth European Rotorcraft Forum*, Glasgow, Scotland, September 1990.

19. Summa, J.M., "Advanced Rotor Analysis Methods for the Aerodynamics of Vortex/Blade Interactions in Hover", *Vertica*, Vol. 9, No. 4, 1985.

20. Egolf, T.A., and Sparks, S.P., "A Full Potential Rotor Analysis with Wake Influence Using an Inner/Outer Domain Technique", *J. Am. Hel. Soc.*, Vol. 32, No. 3, July 1988.

21. Wake, B.E., and Lakshmi, N.S., "Solutions of the Navier-Stokes Equations for the Flow about a Rotor Blade", *J. Am. Hel. Soc.*, April 1989.

22. Scully, M.B., "Computation of Helicopter Rotor Wake Geometry and its Influence on Rotor Harmonic Airloads", MIT ASRL-TR-178-1, March 1971.

23. Widnall, S.E., "The Structure and Dynamics of Vortex Filaments", *Annual Review of Fluid Mechanics*, Vol. 7, 1975.

24. Summa, J.M., Strash, D.J. and Yoo, S., "A Zonal Flow Analysis Method for Two-Dimensional Airfoils", AIAA-90-0571, *AIAA J.*, Vol. 30, No. 2, February 1992.

25. Yoo, S., Summa, J.M., and Strash, D.J., "Angle-of-Attack Validation of a New Zonal CFD Method for Airfoil Simulations", Presented at 8th Applied Aero. Conf., Portland, OR, August 1990.

26. Strash, D.J., Summa, J.M., Yoo, S., "Mach Number Validation of a New Zonal CFD Method (ZAP2D) for Airfoil Simulations", AIAA-91-0185, January 1991.

27. Harris, C.D., "Two-Dimensional Aerodynamic Characteristics of the NACA 0012 Airfoil in the Langley 8-Foot Transonic Pressure Tunnel", *NASA TM-81927*, April 1981.

28. Raghavan, V., McCroskey, W.J., Van Dalsen, W.R. and Baeder, J.D., "Calculations of the Flow Past Bluff Bodies, Including Tilt-Rotor Wing Sections at a = -90°", AIAA-90-0032, 1990.

29. McCroskey, W.J., "A Critical Assessment of Wind Tunnel Results for the NACA 0012 Airfoil", *NASA TM-100019*, October 1987.

30. Anderson, D.A., "Tannehill, J.C. and Pletcher, R.J., *Computational Fluid Mechanics and heat Transfer*, Hemisphere Publishing Corporation, New York, 1984.

31. Bragg, M.B., Khodadoust, A. (Ohio State University), "Effect of Simulated Glaze Ice on a Rectangular Wing", AIAA-89-0750, January 1989.

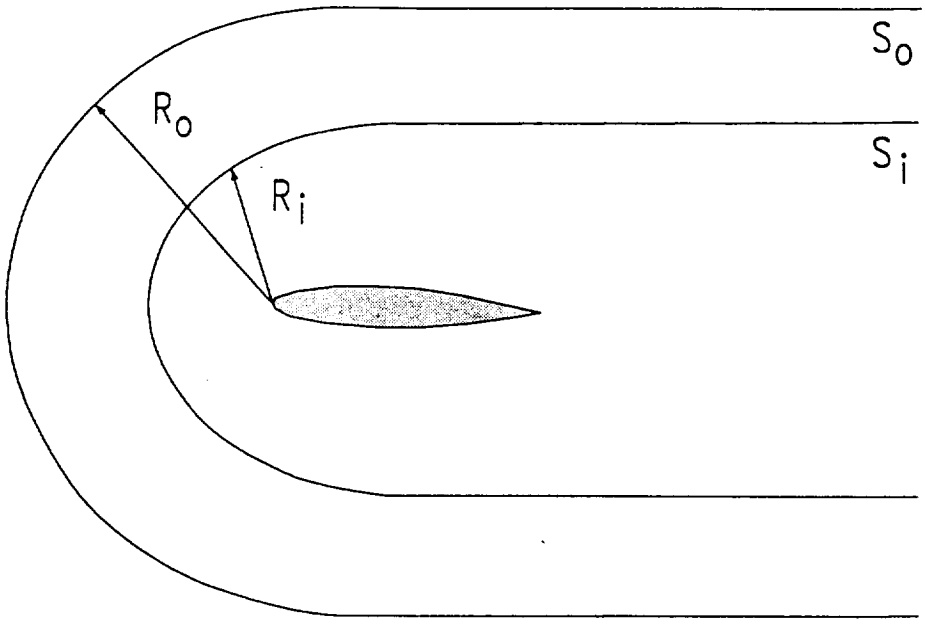

Fig. 1. Zonal Representation of the Physical Flow Field.

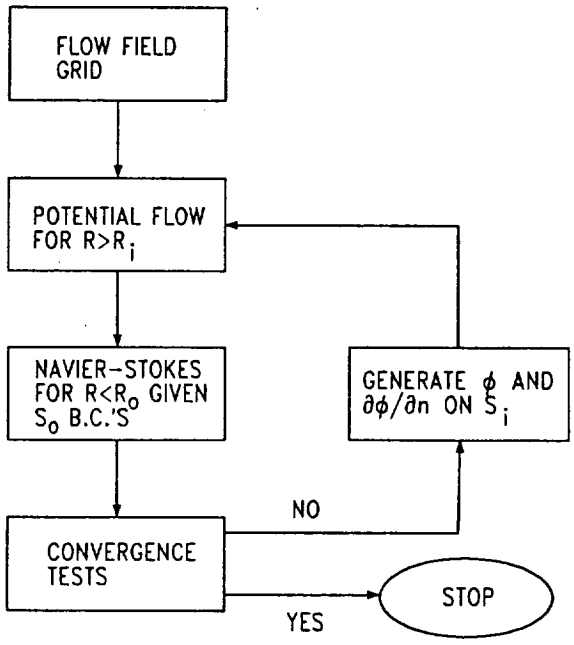

Fig. 2. Zonal Methodology Flow Chart.

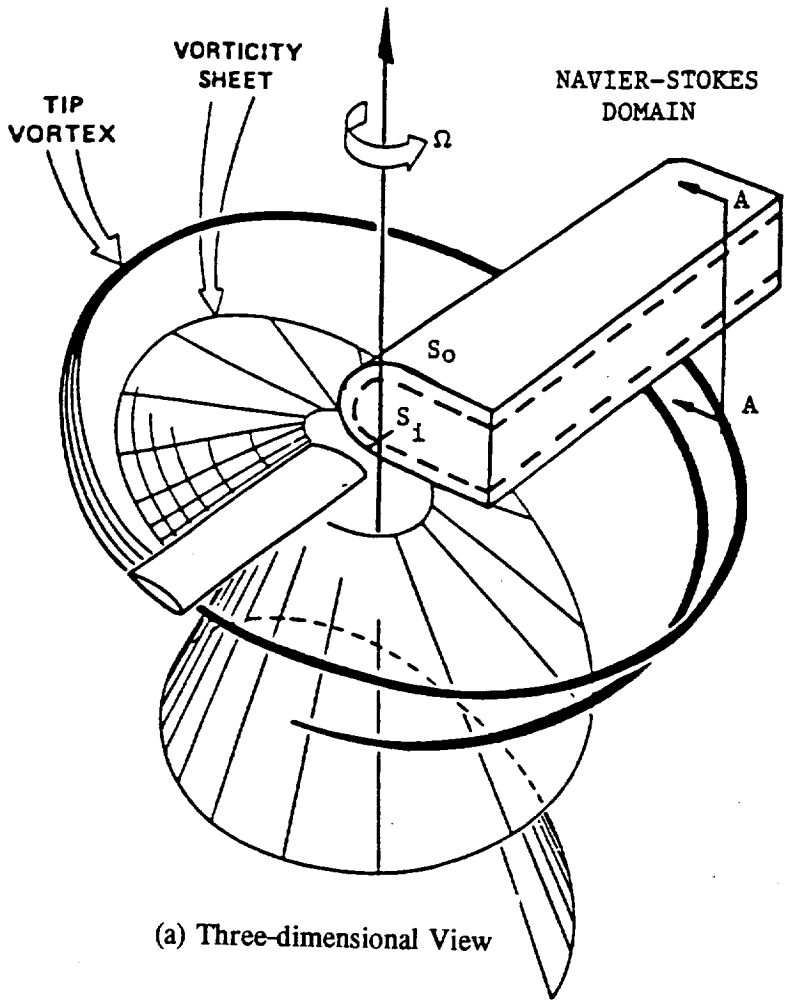

(a) Three-dimensional View

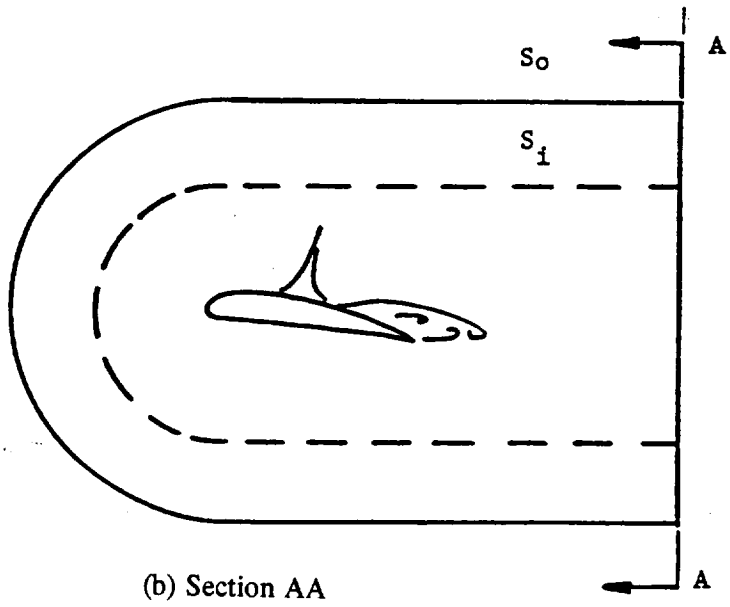

(b) Section AA

Fig. 3. Zonal Representation of Hover/Climb Rotor Flow Field.

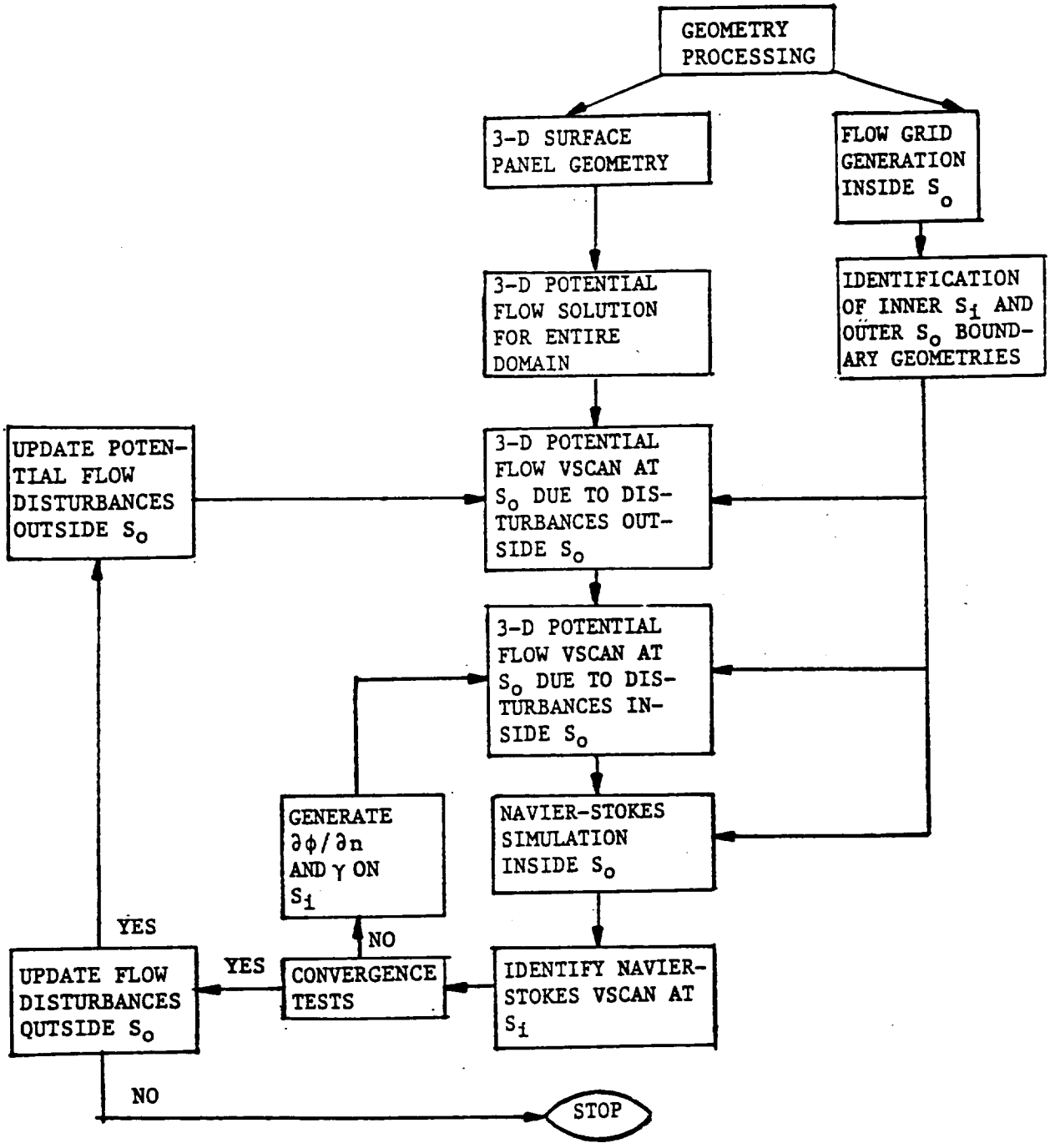

Fig. 4. Zonal Hover/Climb Rotor Methodology Flow Chart.

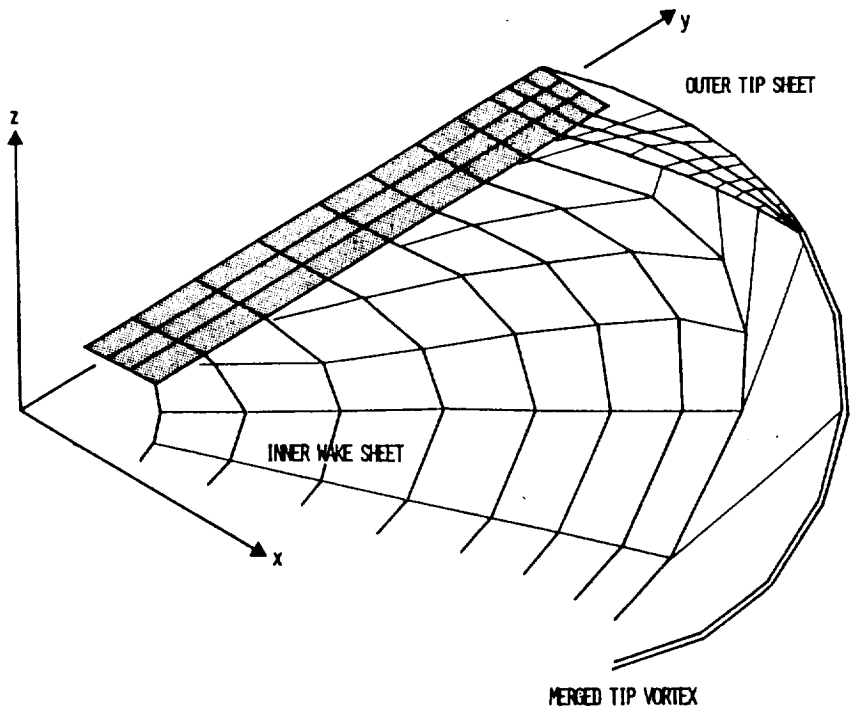

Fig. 5. Rotor Blade Vortex-Lattice Model.

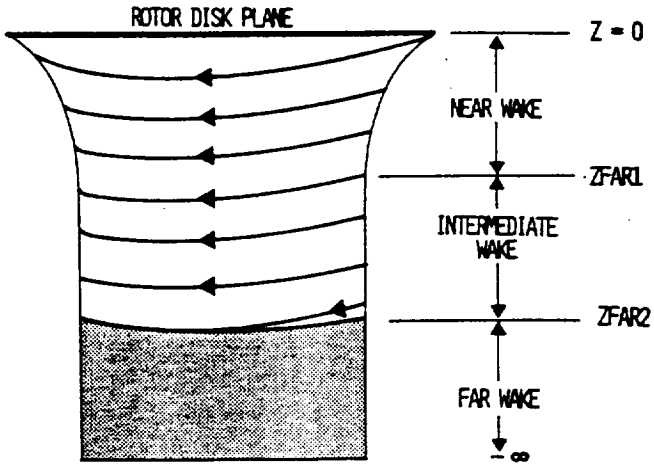

Fig. 6. Global Hover Wake Model.

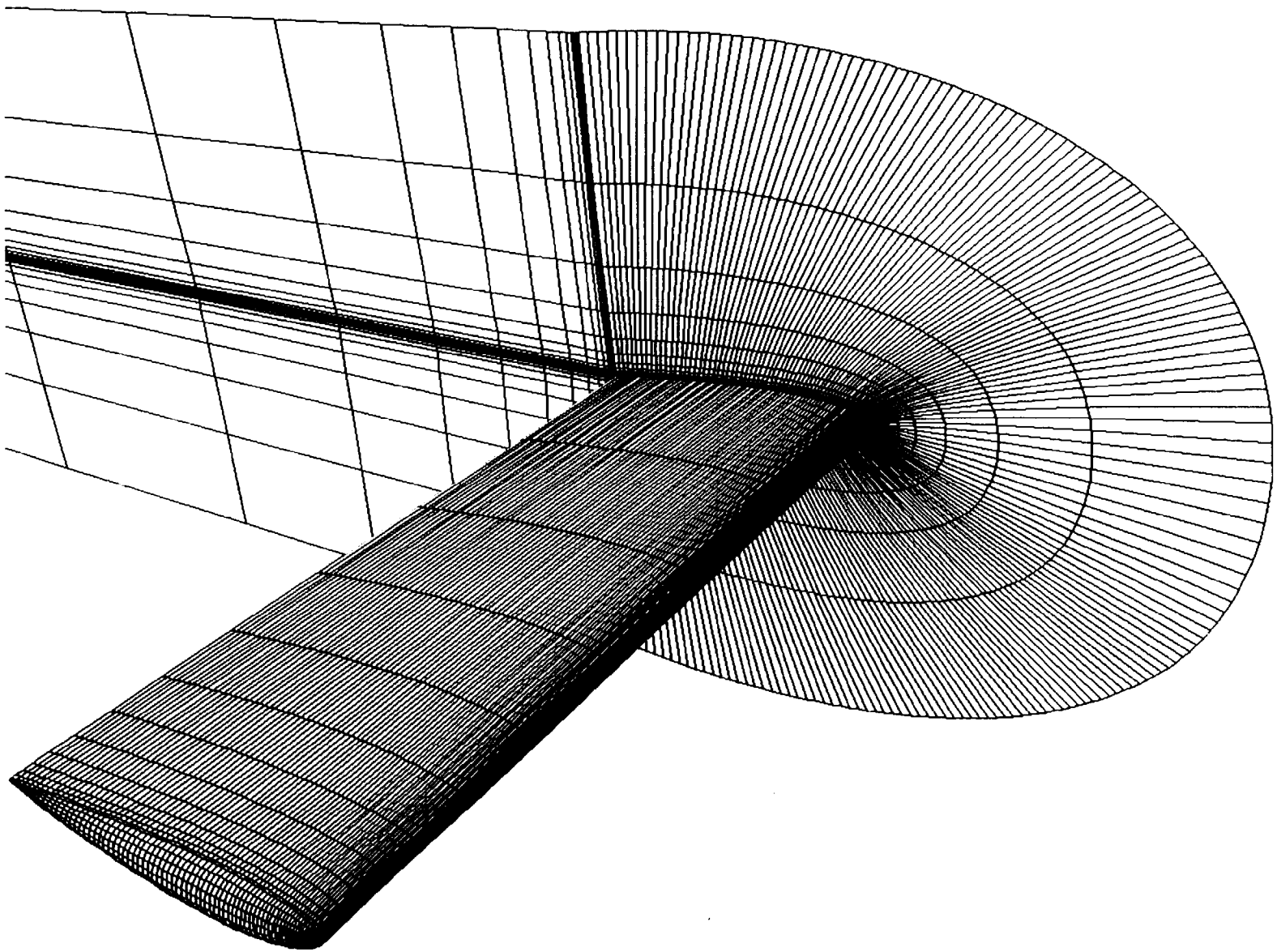

Fig. 7. Grid Definition for an AR 5 Rectangular Wing Including Partial View of Plane of Symmetry.

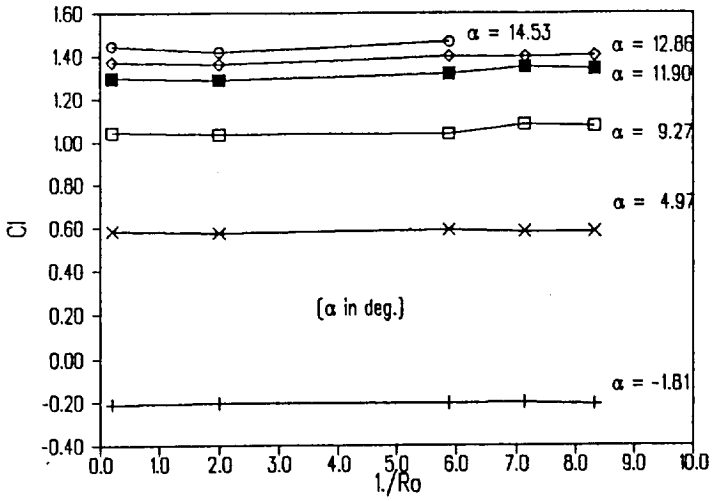

(a) Lift Coefficient

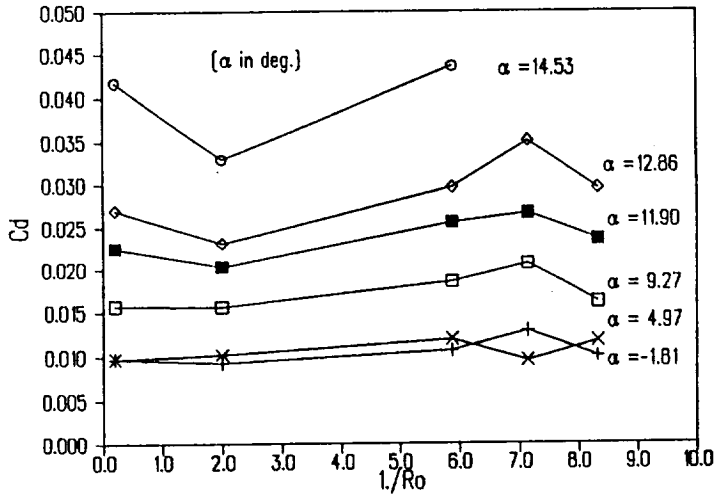

(b) Drag Coefficient

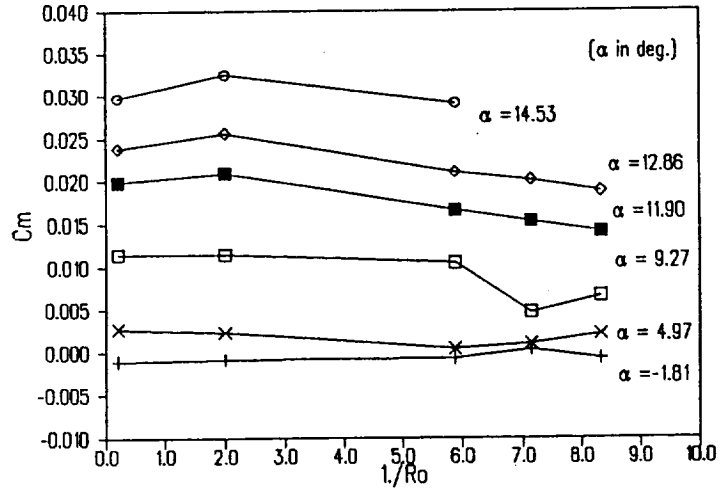

(c) Moment Coefficient

Fig. 8. Computed Force and Moment Variation vs. Domain Size for NACA 0012 Airfoil with Angle-of-Attack Variation; M=0.3 and R_e=3.0 Million.

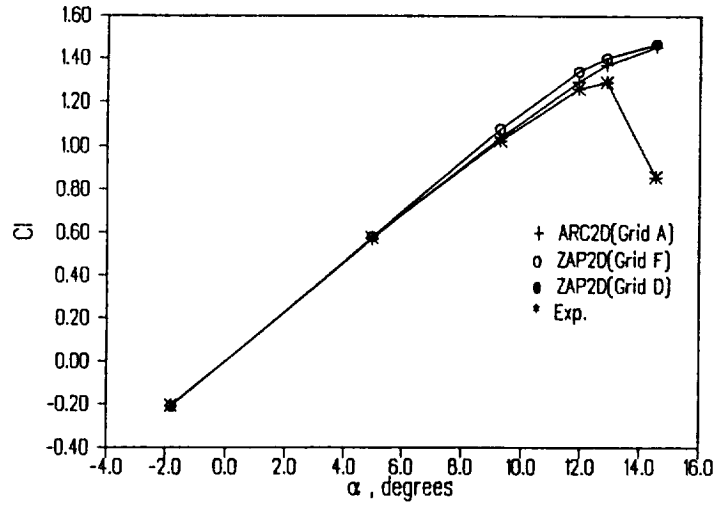

(a) Lift Coefficient

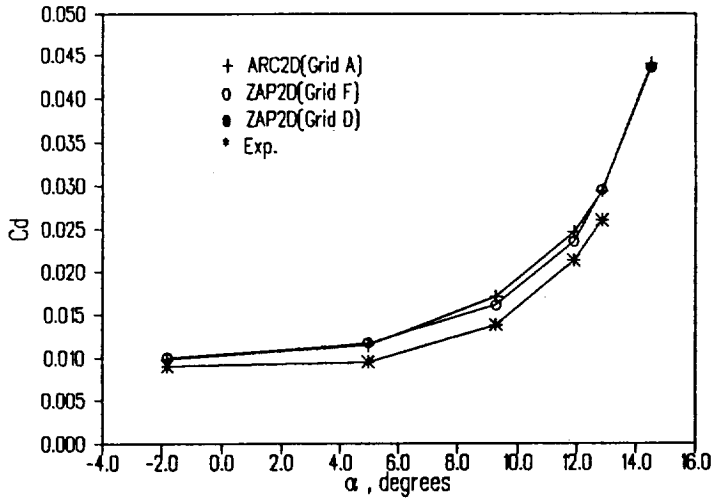

(b) Drag Coefficient

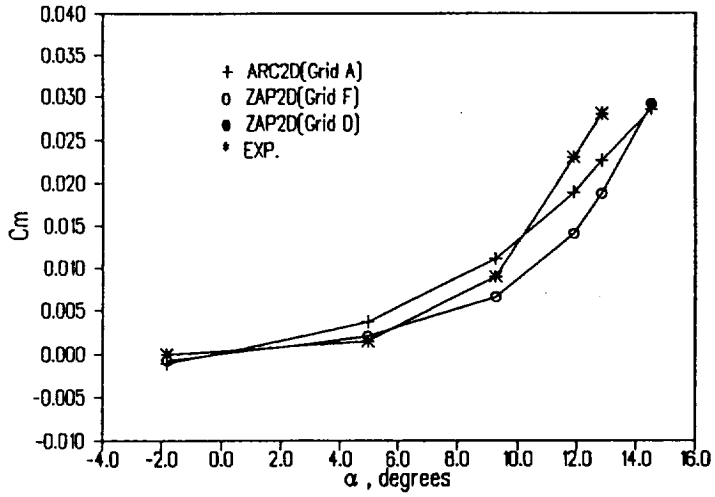

(c) Moment Coefficient

Fig. 9. Computed Force and Moment Variation vs. Angle of Attack for NACA 0012 Airfoil with Domain Size Variation; M=0.3, R_e=3.0 Million.

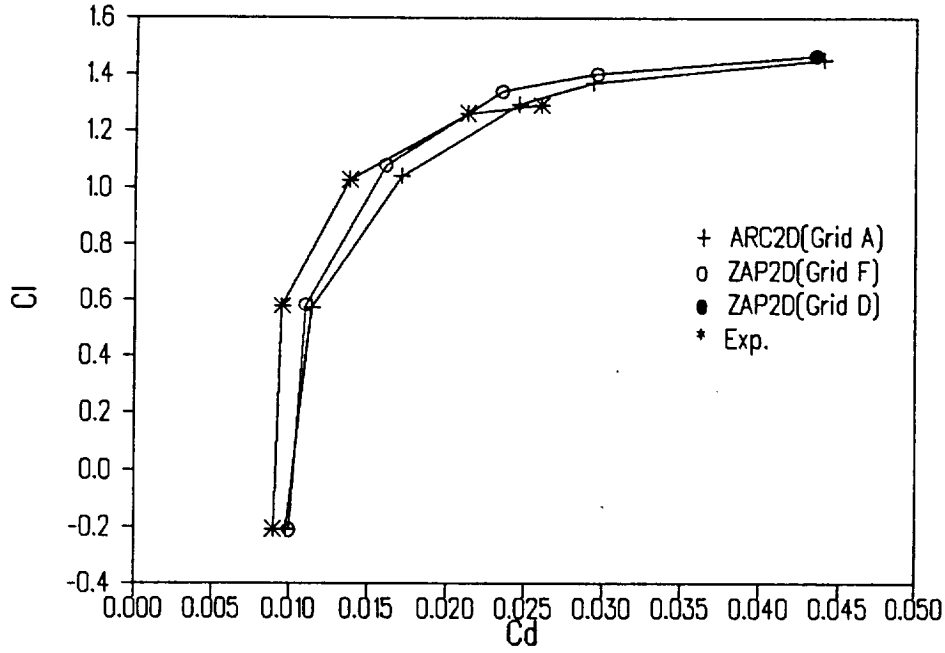

(a) Lift vs. Drag Coefficient

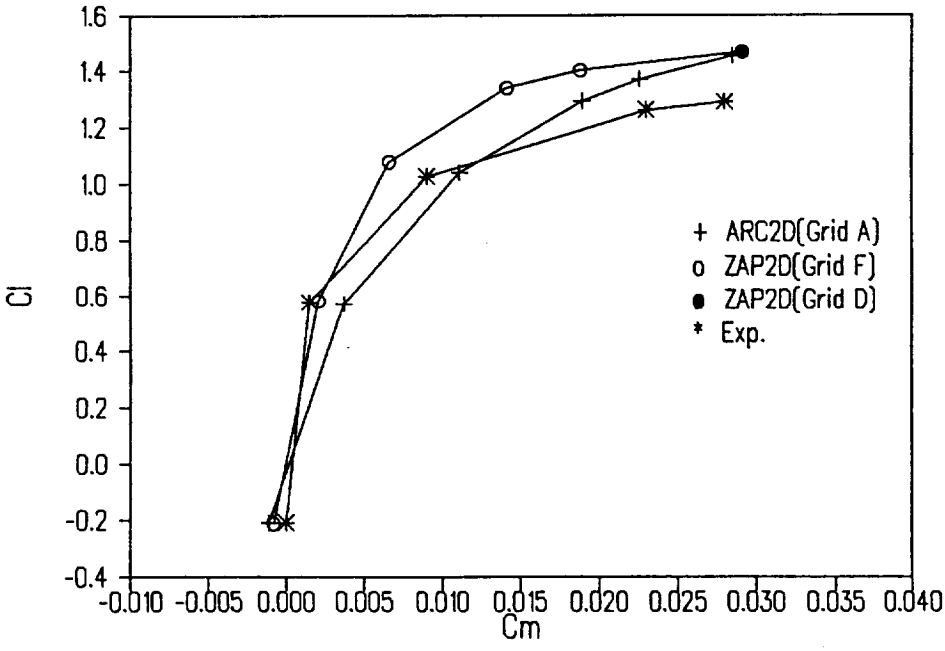

(b) Lift vs. Moment Coefficient

Fig. 10. Drag Polar and Pitching Moment Curve with Domain Size Variation; M=0.3 and R_e=3.0 Million.

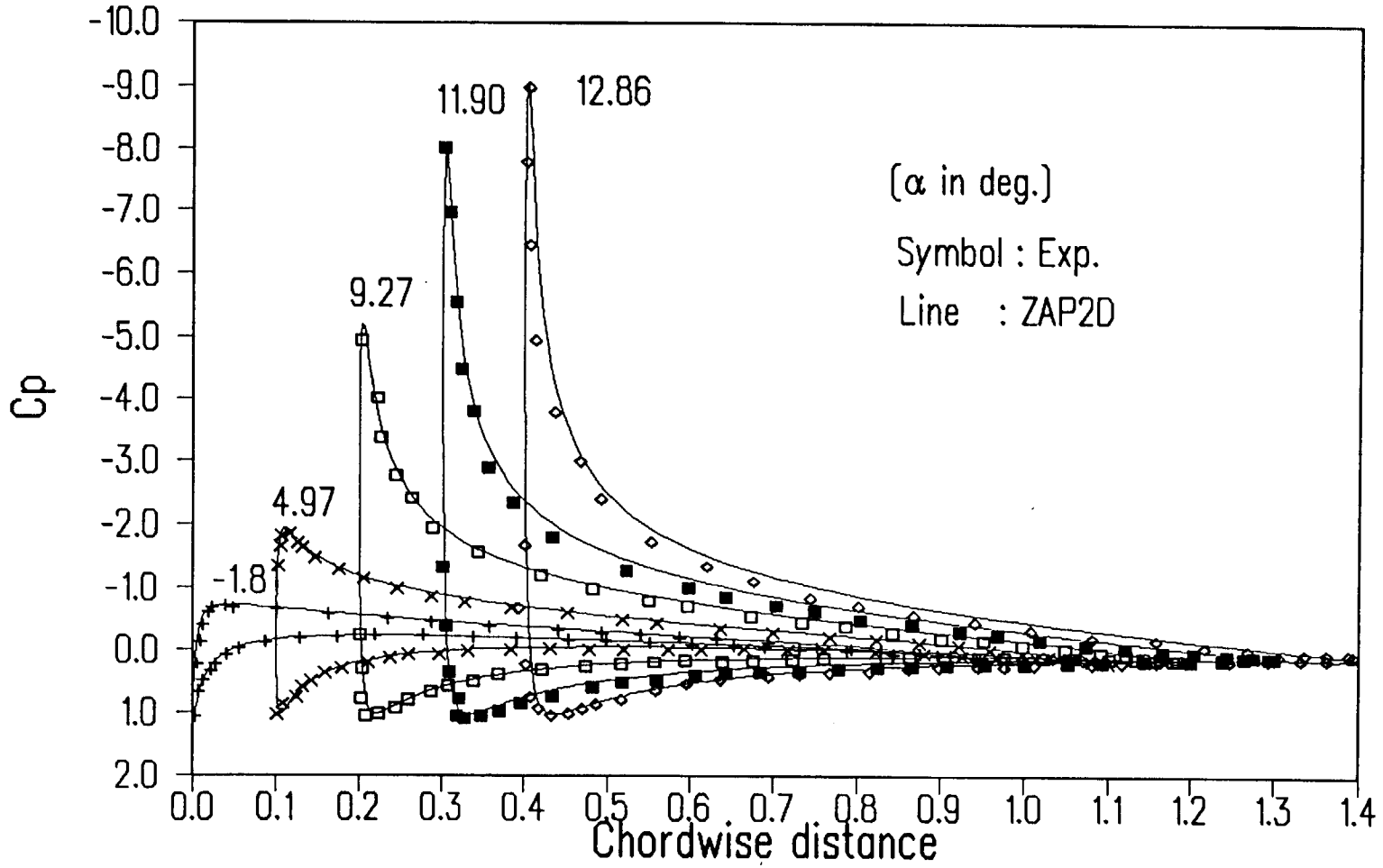

Fig. 11. Comparison of Computed (GRID F) and Experimental Pressure Distribution; M=0.3 and R_e=3.0 Million.

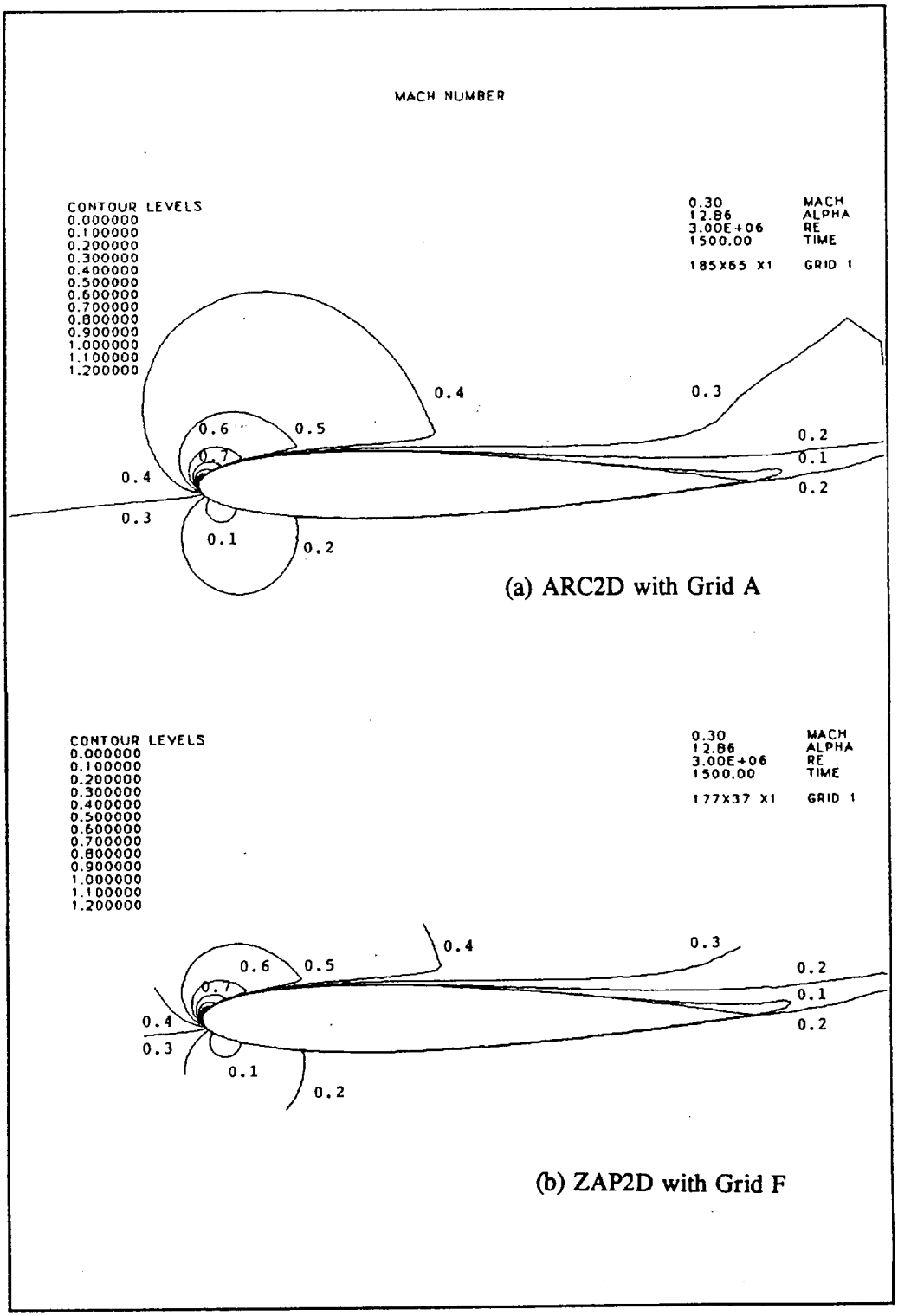

Fig. 12. Comparison of ZAP2D and ARC2D Computed Mach Contours;M=0.3, R_e=3.0 Million and α = 12.86°.

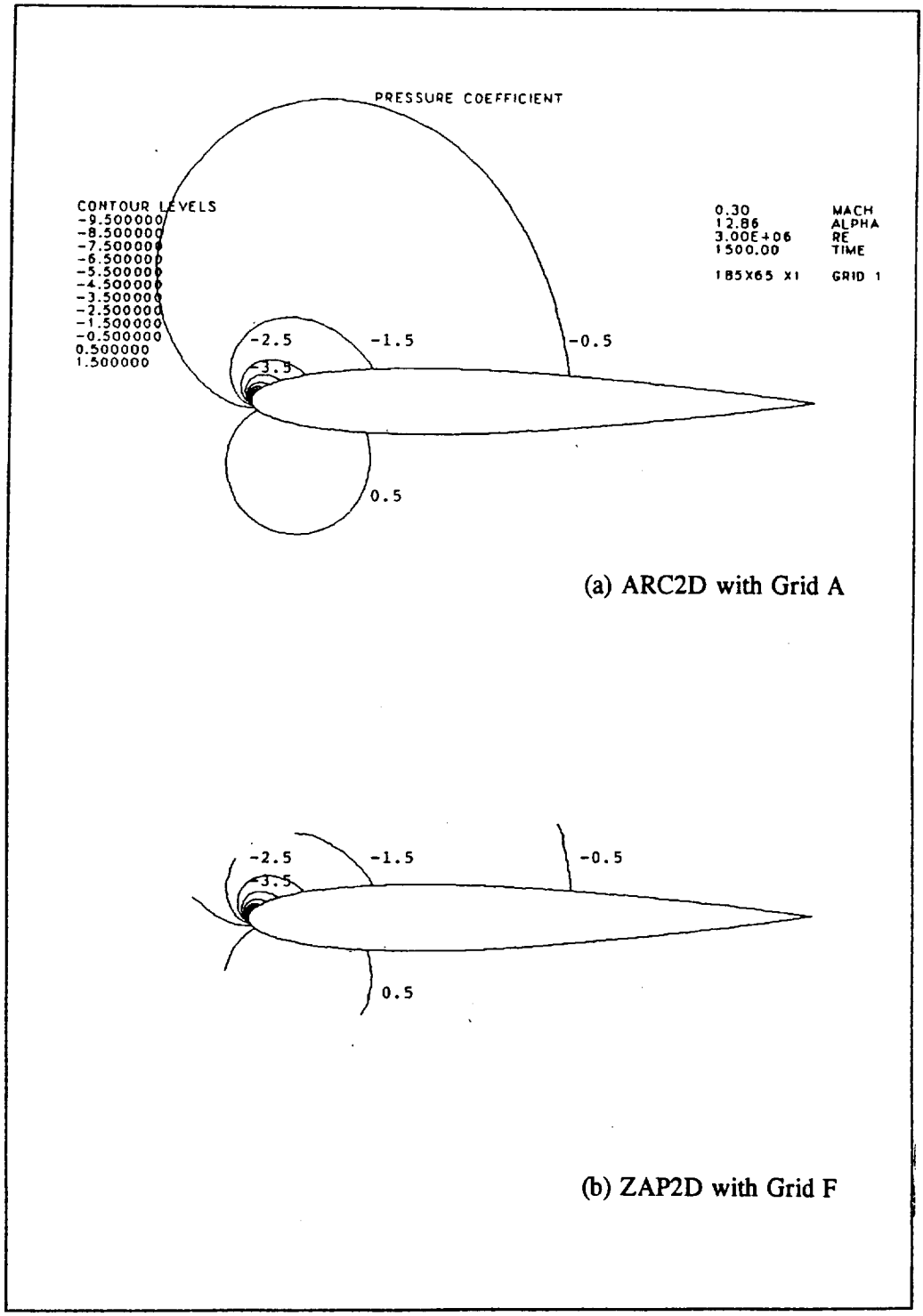

Fig. 13. Comparison of ZAP2D and ARC2D Computed Pressure Contours; M=0.3, R_e=3.0 Million and α=12.86°.

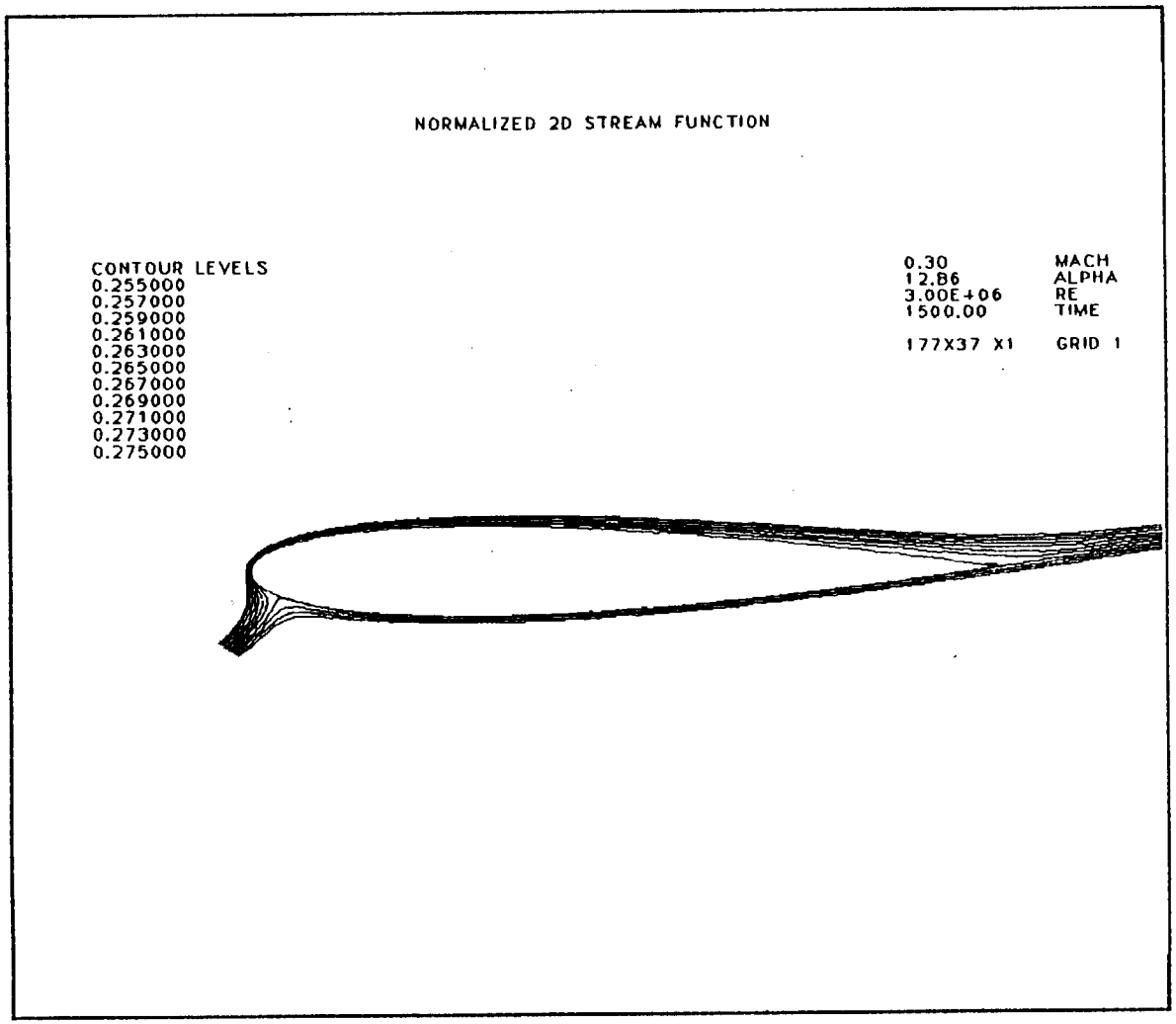

Fig. 14. Streamlines around the NACA 0012 Airfoil; M=0.3, R_e=3.0 Million and α=12.86°.

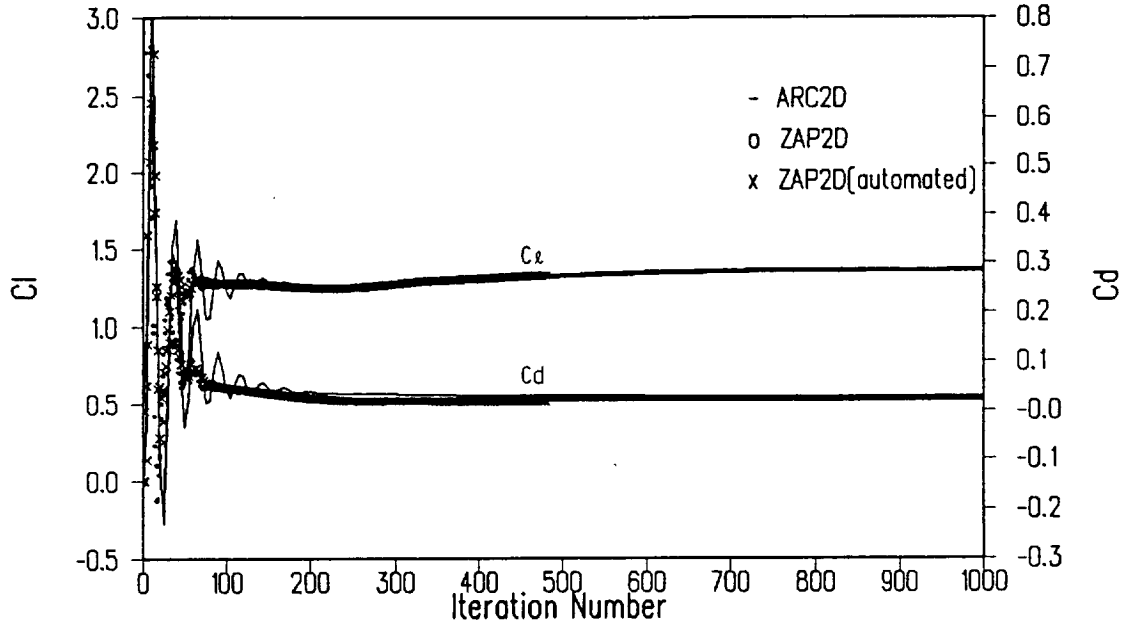

(a) C_ℓ and C_d Iteration History

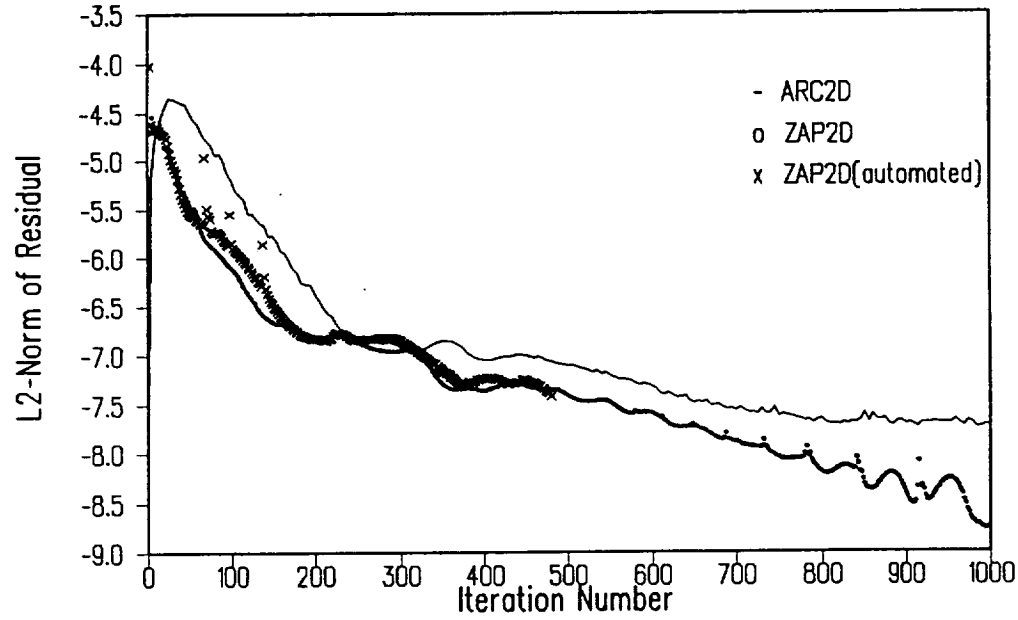

(b) L2-Norm Residual Iteration History

Fig. 15. Comparison of ZAP2D (R_o=0.17) and ARC2D (R_o=25) Computed Loads and Residual Iteration History; M=0.3, R_e=3.0 Million and α=12.86°.

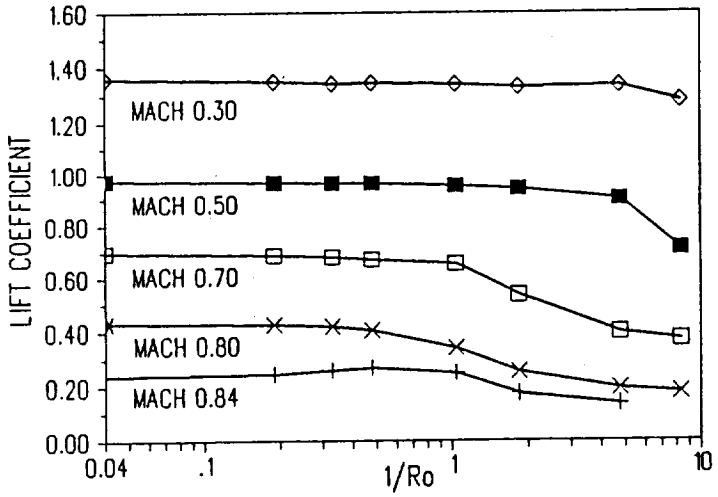

(a) ZAP2D (Grids B-H) and ARC2D (Grid A) Computed Lift Coefficient

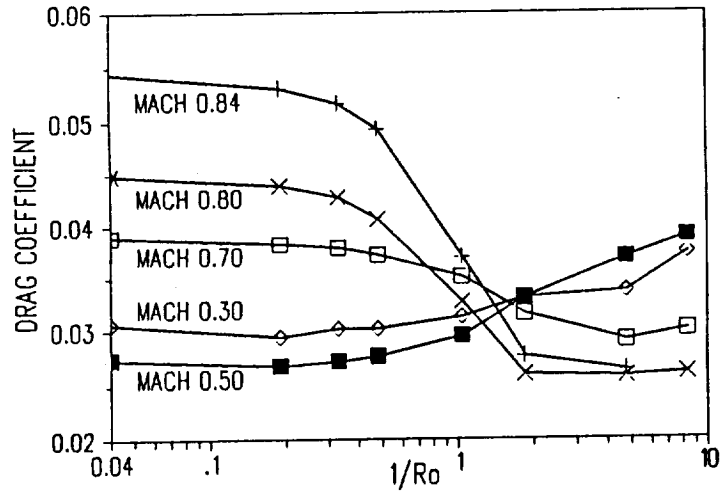

(b) ZAP2D (Grids B-H) and ARC2D (Grid A) Computed Drag Coefficient

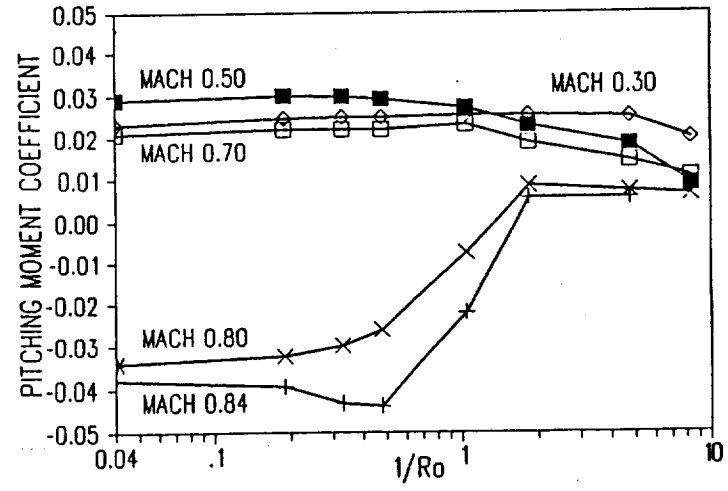

(c) ZAP2D (Grids B-H) and ARC2D (Grid A) Computed Moment Coefficient

Fig. 16. Computed Force and Moment Variation with Domain Size for a NACA 0012 Airfoil at Various Mach Numbers and at Angles of Attack near $C_{l_{MAX}}$.

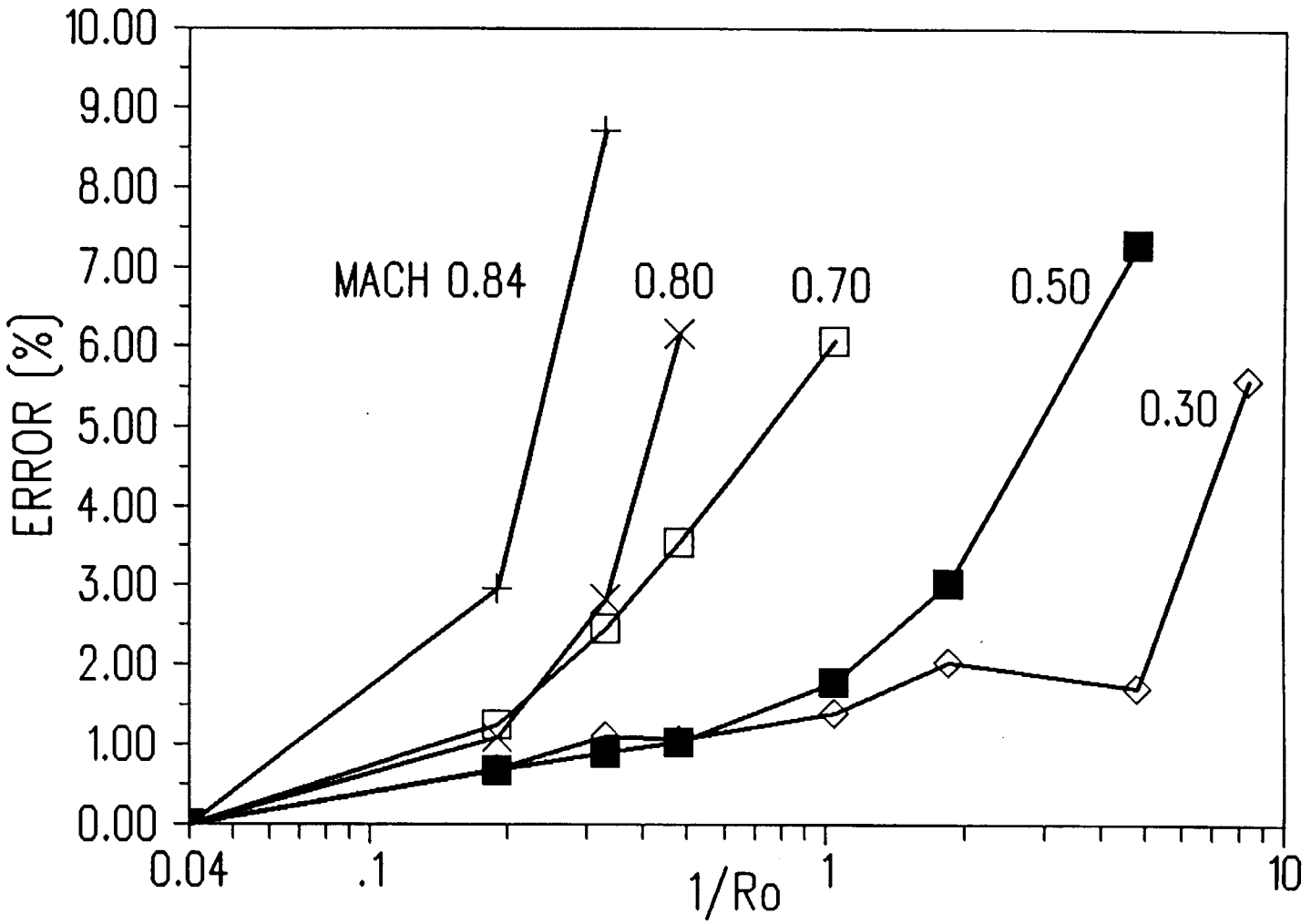

Fig. 17. Error in Lift Coefficient With Domain Size for ARC2D as Compared with the ARC2D Large-Domain Solution.

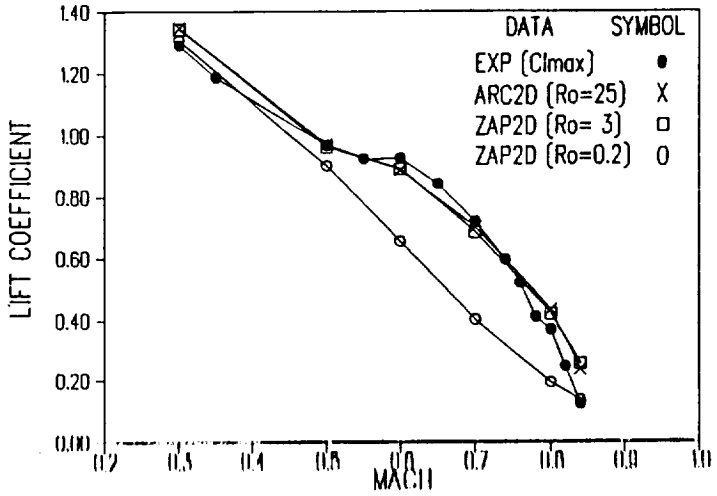

(a) Lift Coefficient

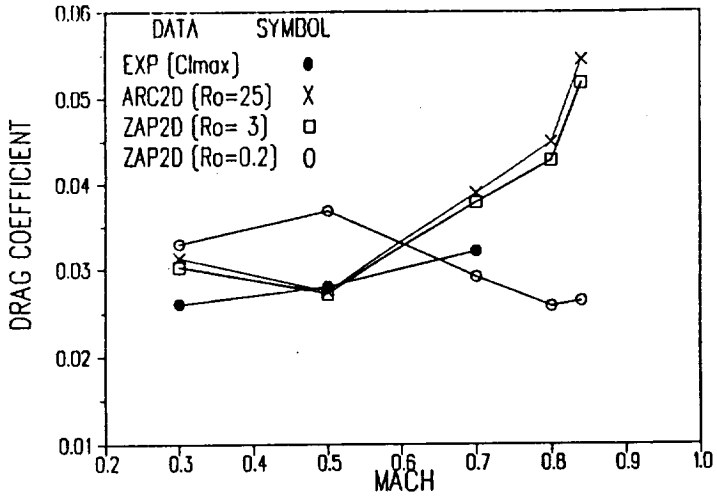

(b) Drag Coefficient

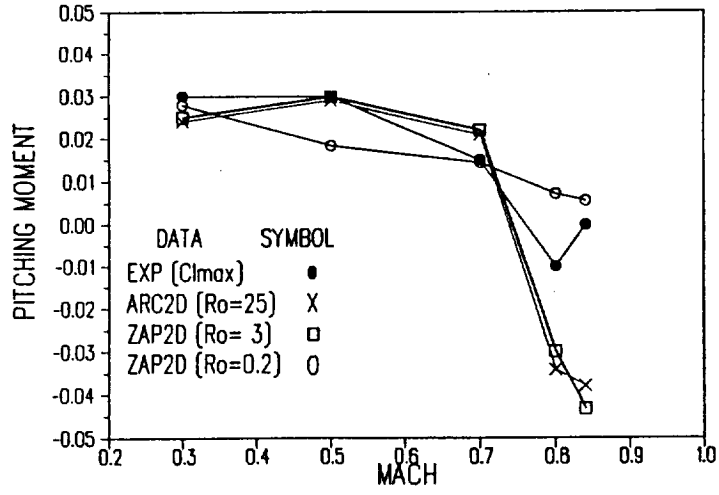

(c) Moment Coefficient

Fig. 18. Comparison of ZAP2D (Grids C and G), ARC2D (Grid A) and Experimental Force and Moment Variation with Mach Number.

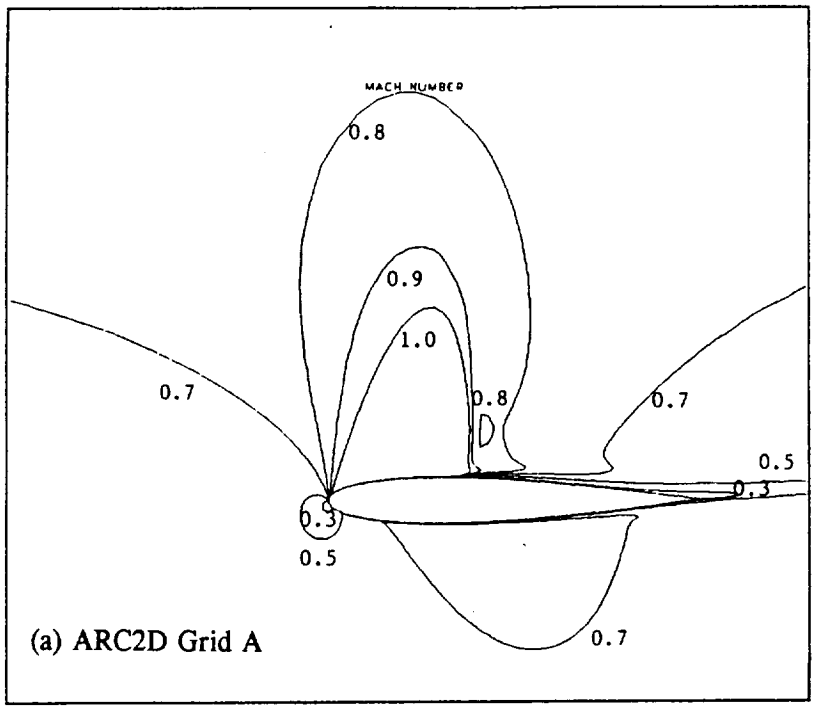

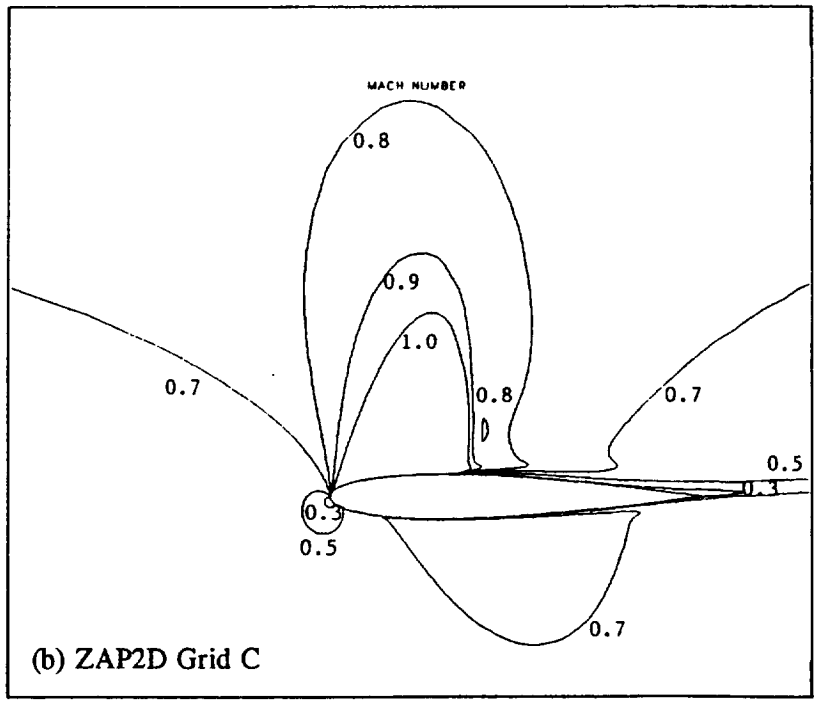

Fig. 19. Comparison of ZAP2D and ARC2D Computed Mach Contours for a NACA 0012 Airfoil at Mach 0.7, α=4.75°.

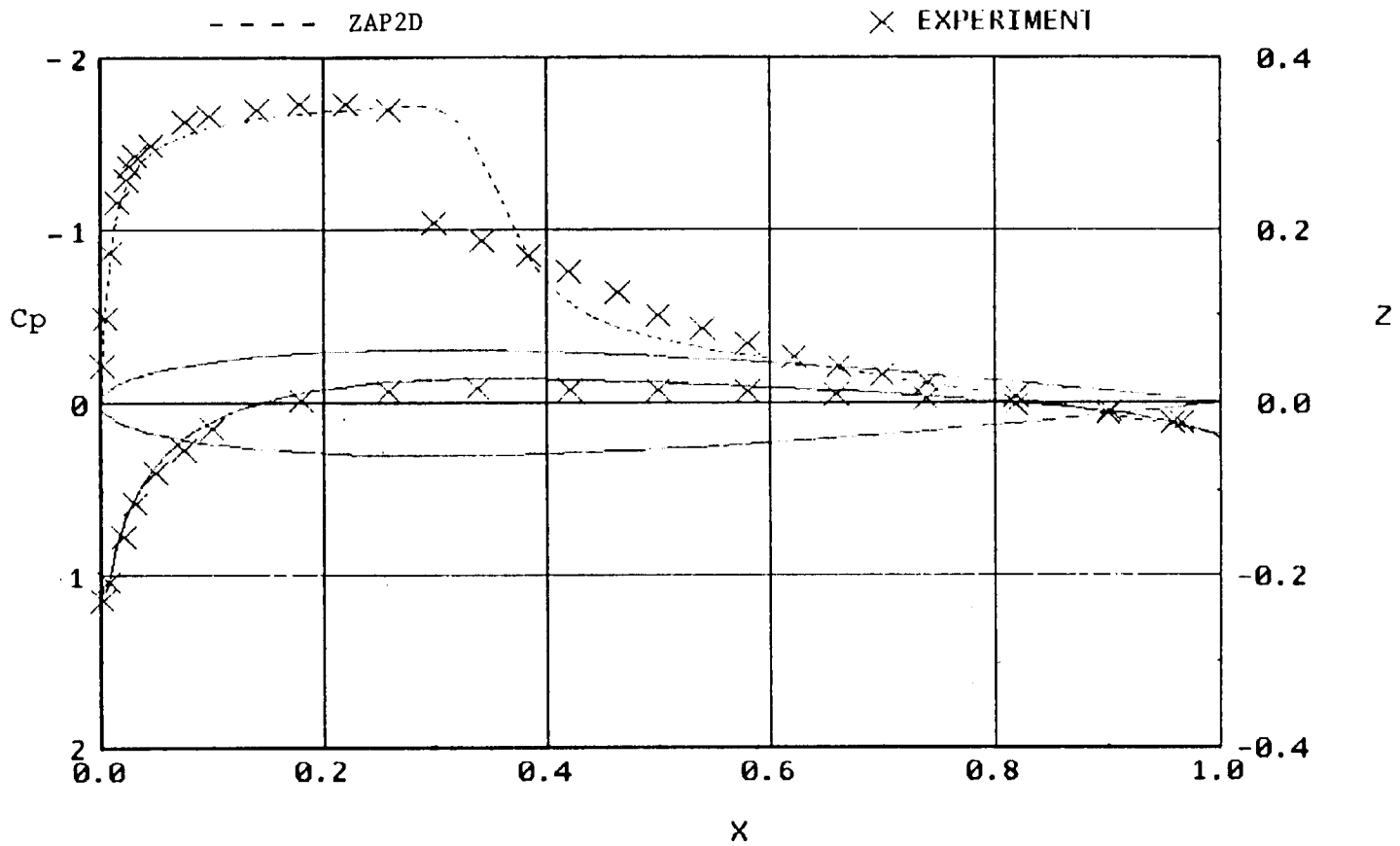

Fig. 20. Comparison of ZAP2D (Grid C) and Experimental Cp Distribution for a NACA 0012 Airfoil at Mach 0.7, α=4.75°.

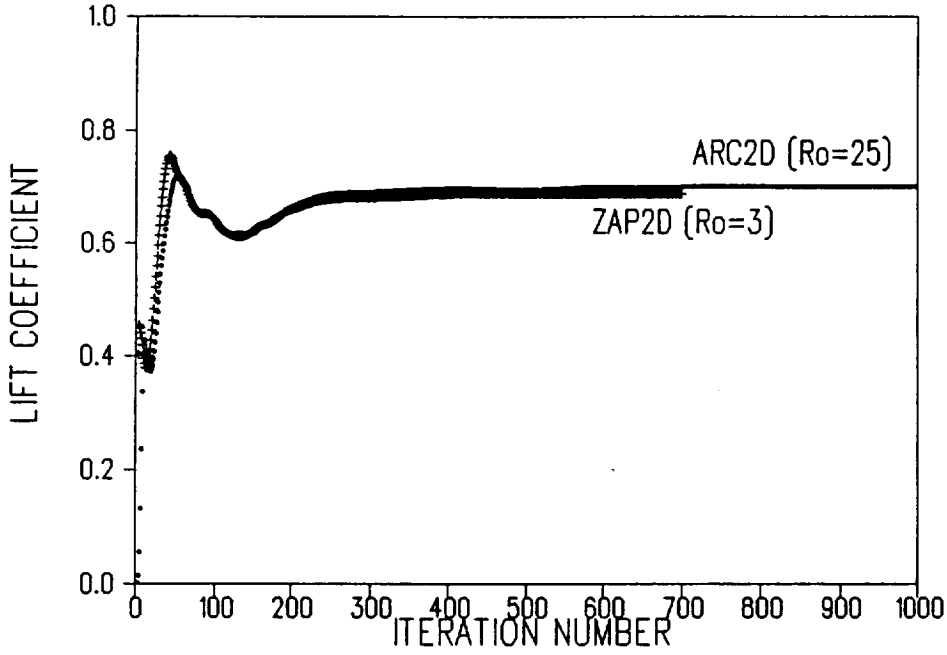

Fig. 21. Comparison of ZAP2D (Grid C) and ARC2D (Grid A) Computed C_ℓ Iteration History for a NACA 0012 Airfoil at Mach 0.7, α=4.75°.

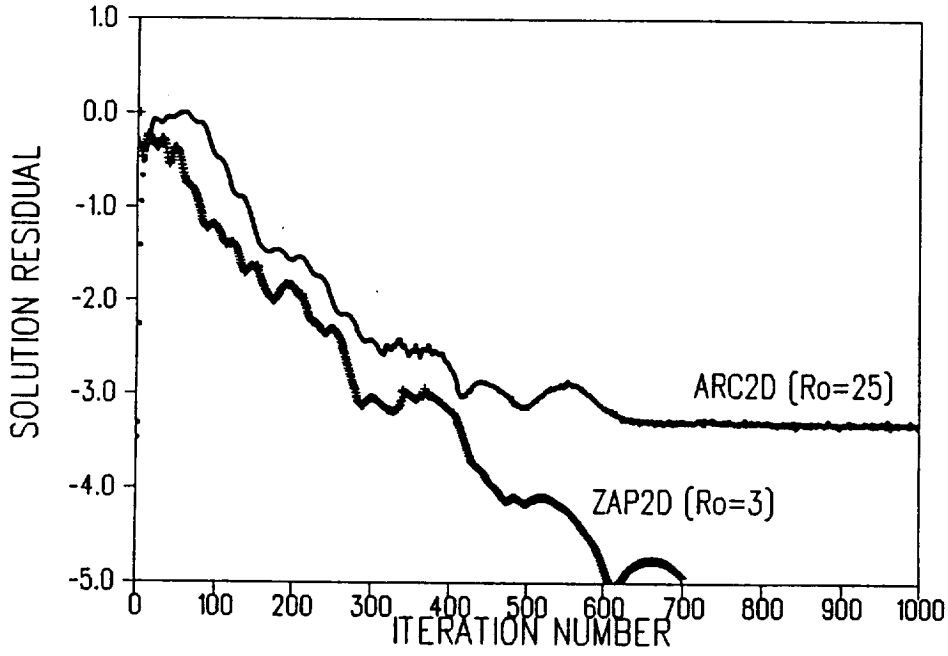

Fig. 22. Comparison of ZAP2D (Grid C) and ARC2D (Grid A) Solution Residual History for a NACA 0012 Airfoil at Mach 0.7, α=4.75°.

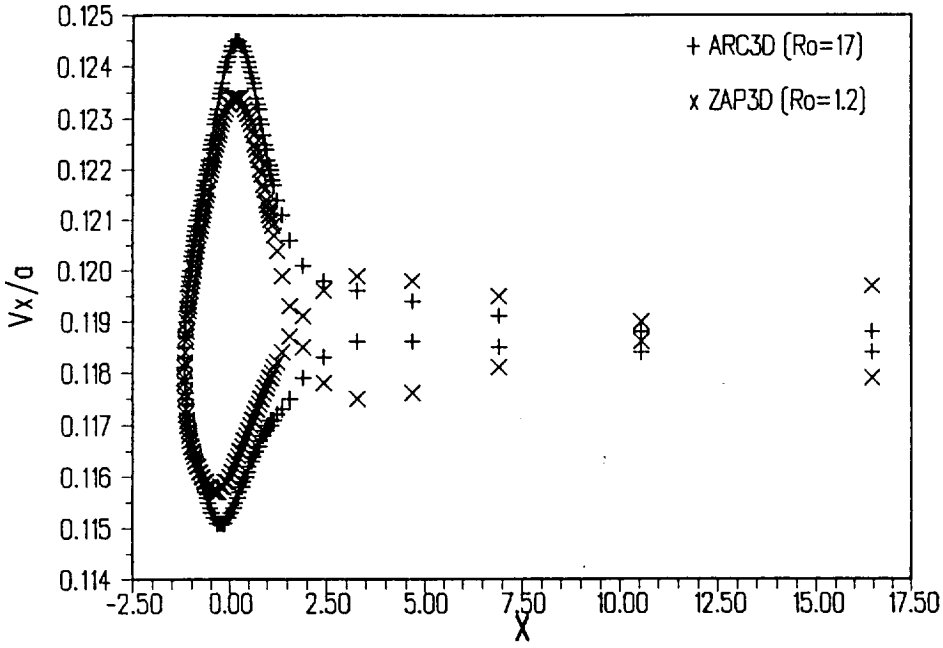

(a) Horizontal Component

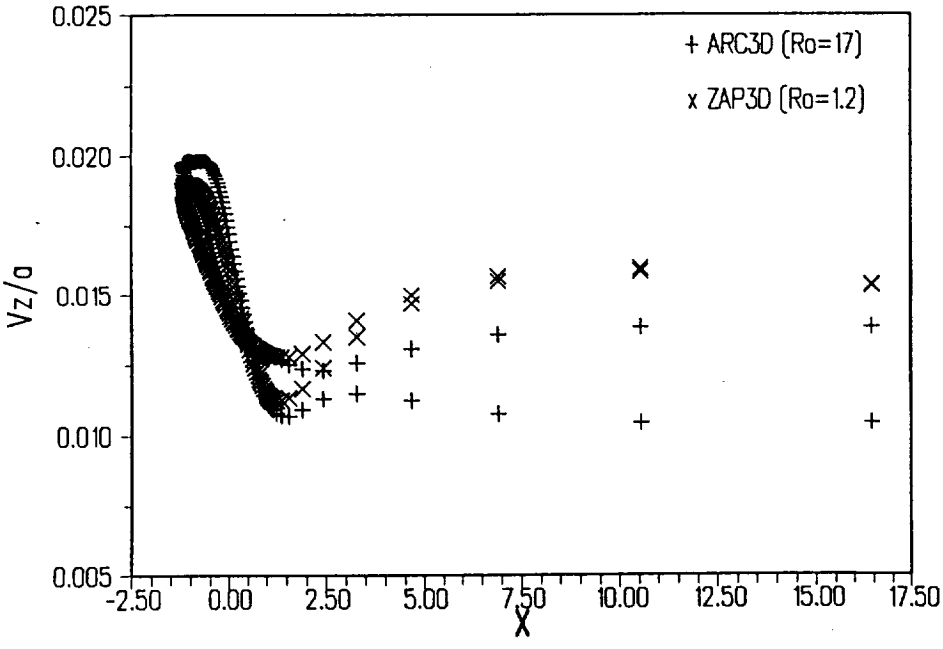

(b) Vertical Component

Fig. 23. Baseline ZAP3D and ARC3D Computed Velocity Component Normalized by Local Speed of Sound for an AR 5 Rectangular Wing at Mach 0.12, α=8.75 and R_e 1.5 Million.

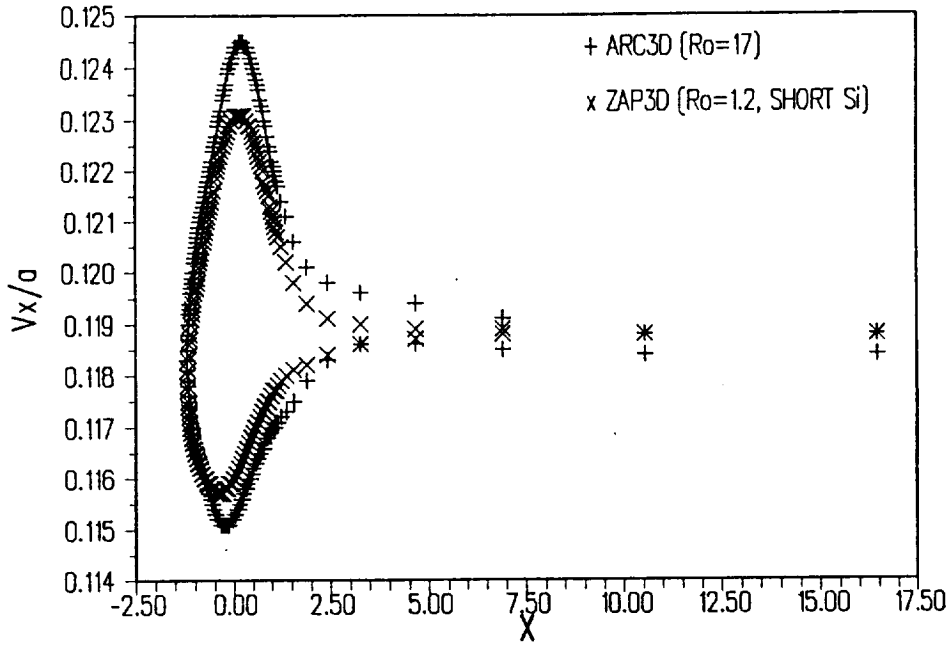

(a) Horizontal Component

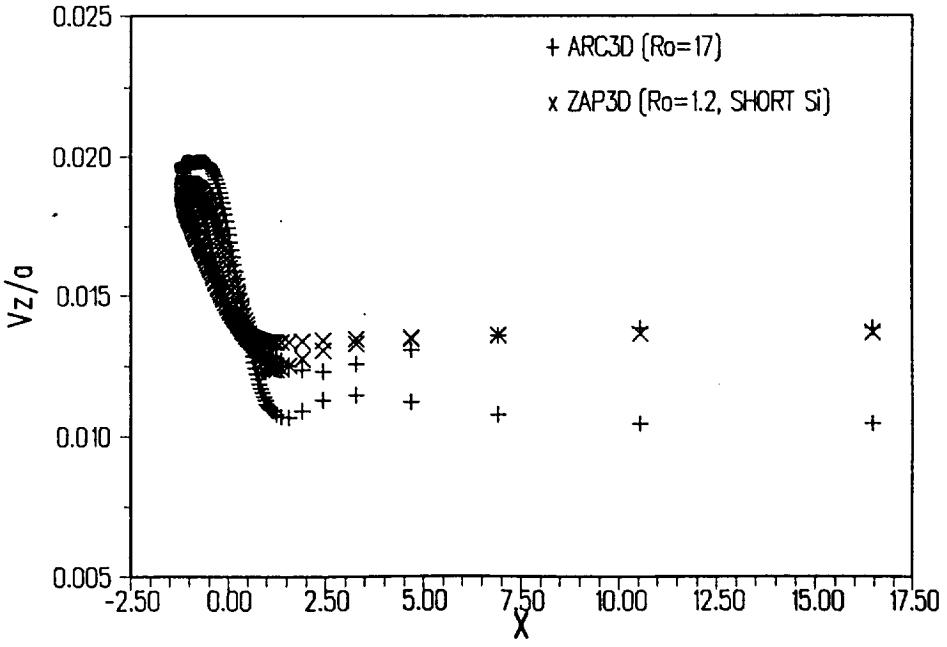

(b) Vertical Component

Fig. 24. ZAP3D and ARC3D Computed Velocity Component Normalized by Local Speed of Sound with Short S_i for an AR 5 Rectangular Wing at Mach 0.12, α=8.75 and R_e 1.5 Million.

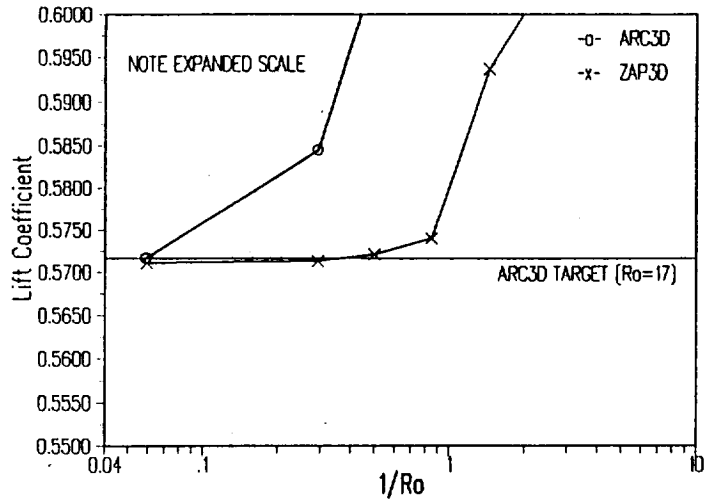

(c) Moment Coefficient

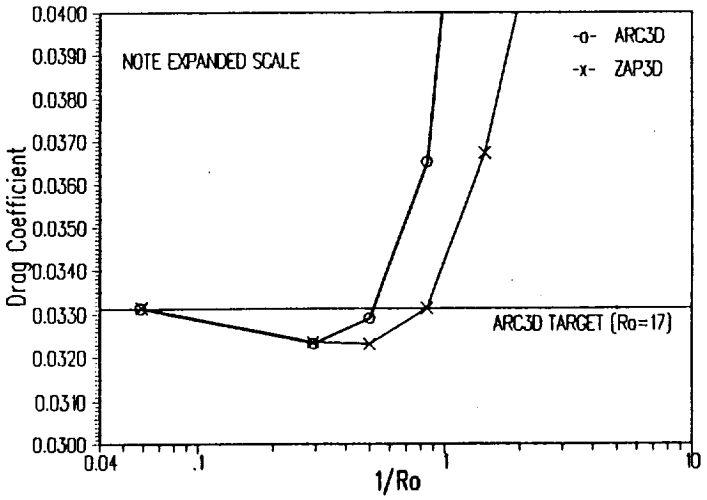

(b) Drag Coefficient

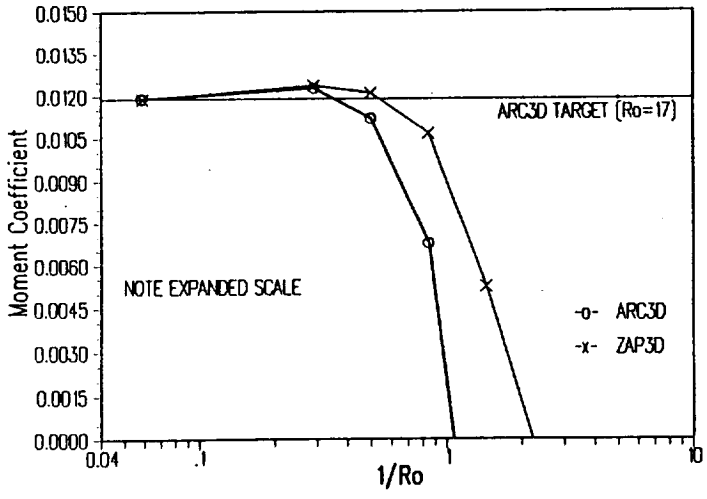

(a) Lift Coefficient

Fig. 25. ZAP3D and ARC3D Computed Force and Moment Variation with Domain Size for an AR 5 Rectangular Wing at Mach 0.12, α=8.75 and R_e 1.5 Million.

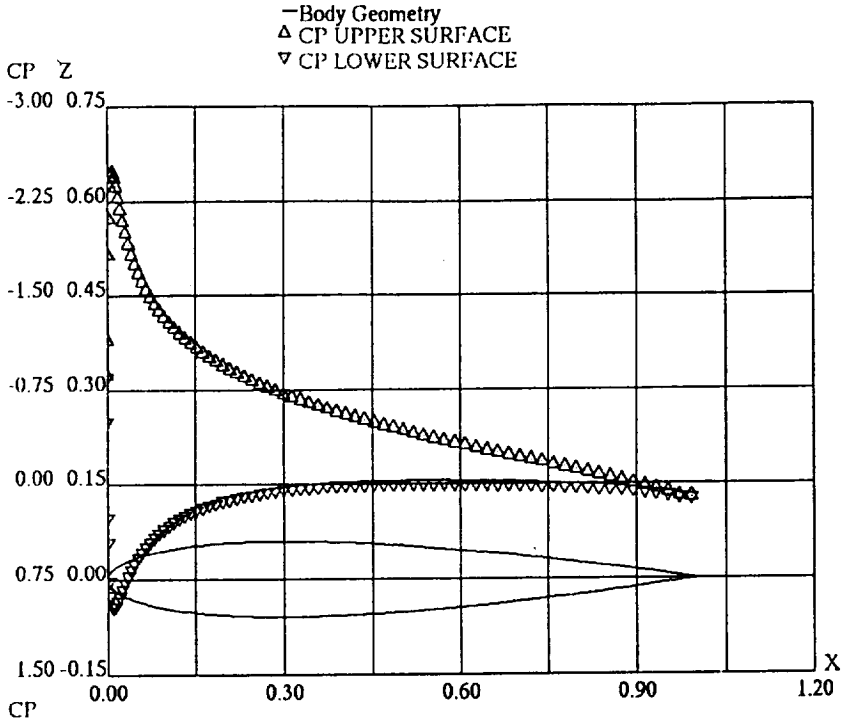

(a) ARC3D with $R_o = 17$

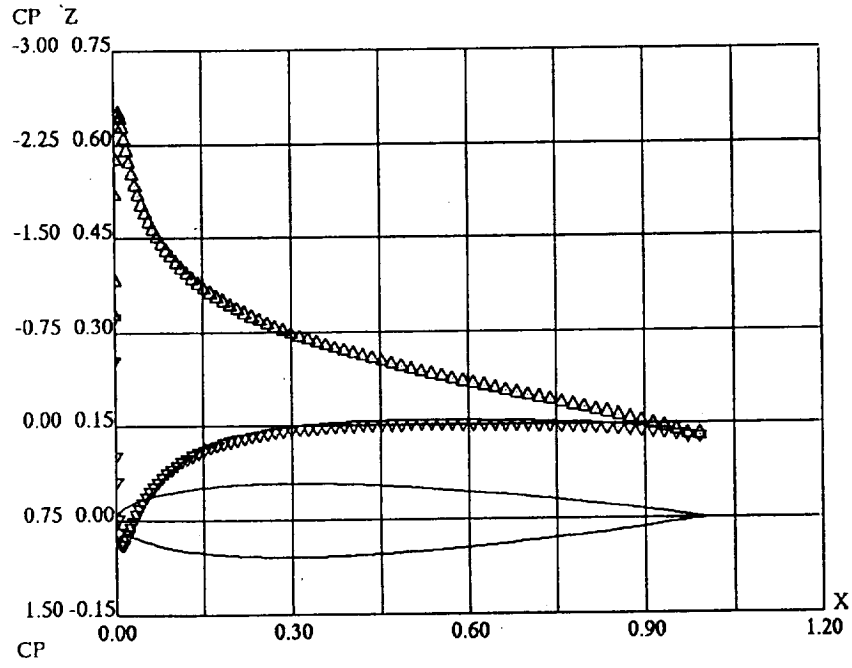

(b) ZAP3D with $R_o = 1.2$

Fig. 26. Computed Surface Pressure Coefficient on the Plane of Symmetry for an AR 5 Rectangular Wing at Mach 0.12, $\alpha = 8.75$ and R_e 1.5 Million.

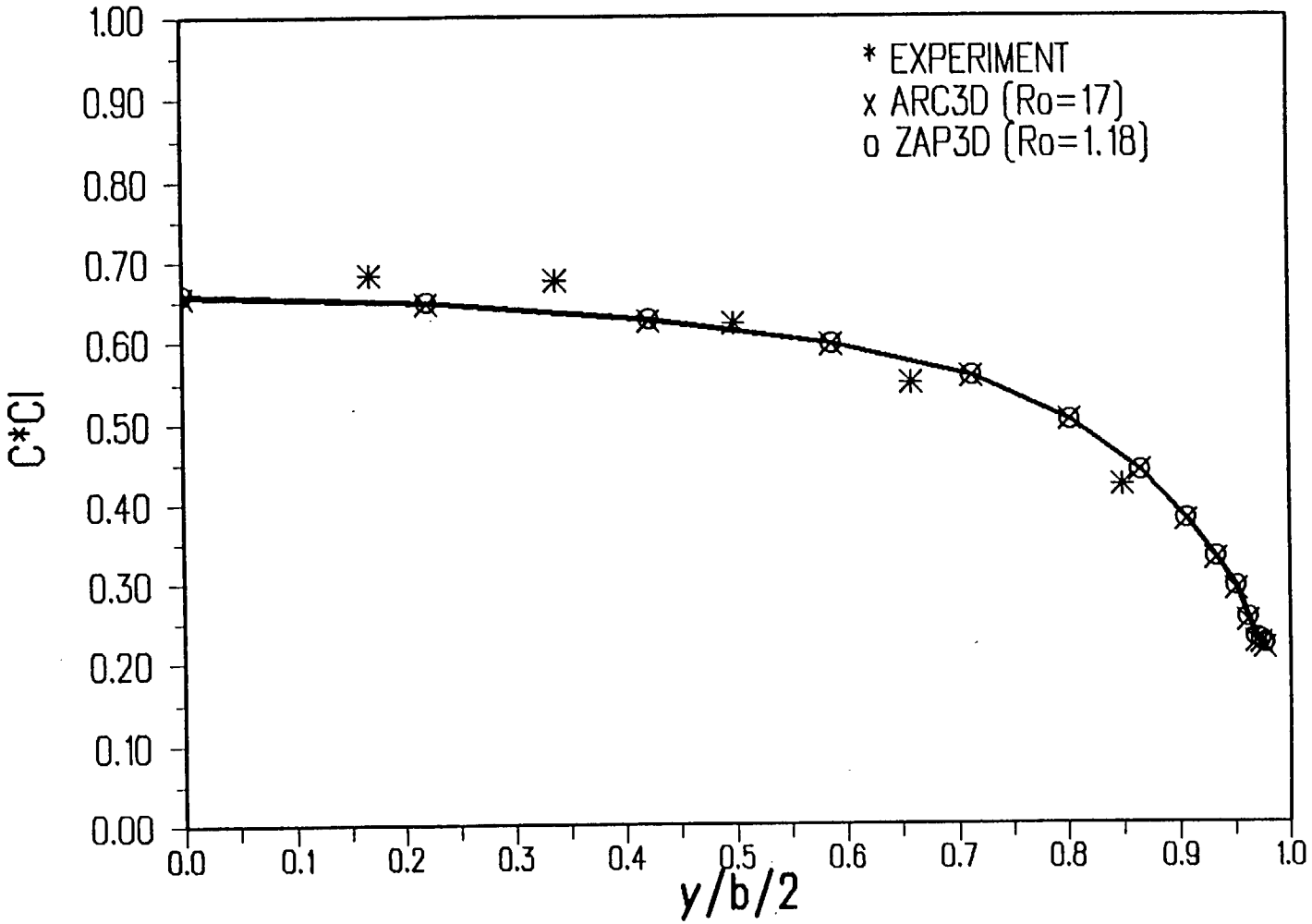

Fig. 27. Computed and Experimental Wing Spanwise Load Distribution for an AR 5 Rectangular Wing at Mach 0.12, α=8.75 and R_e 1.5 Million.

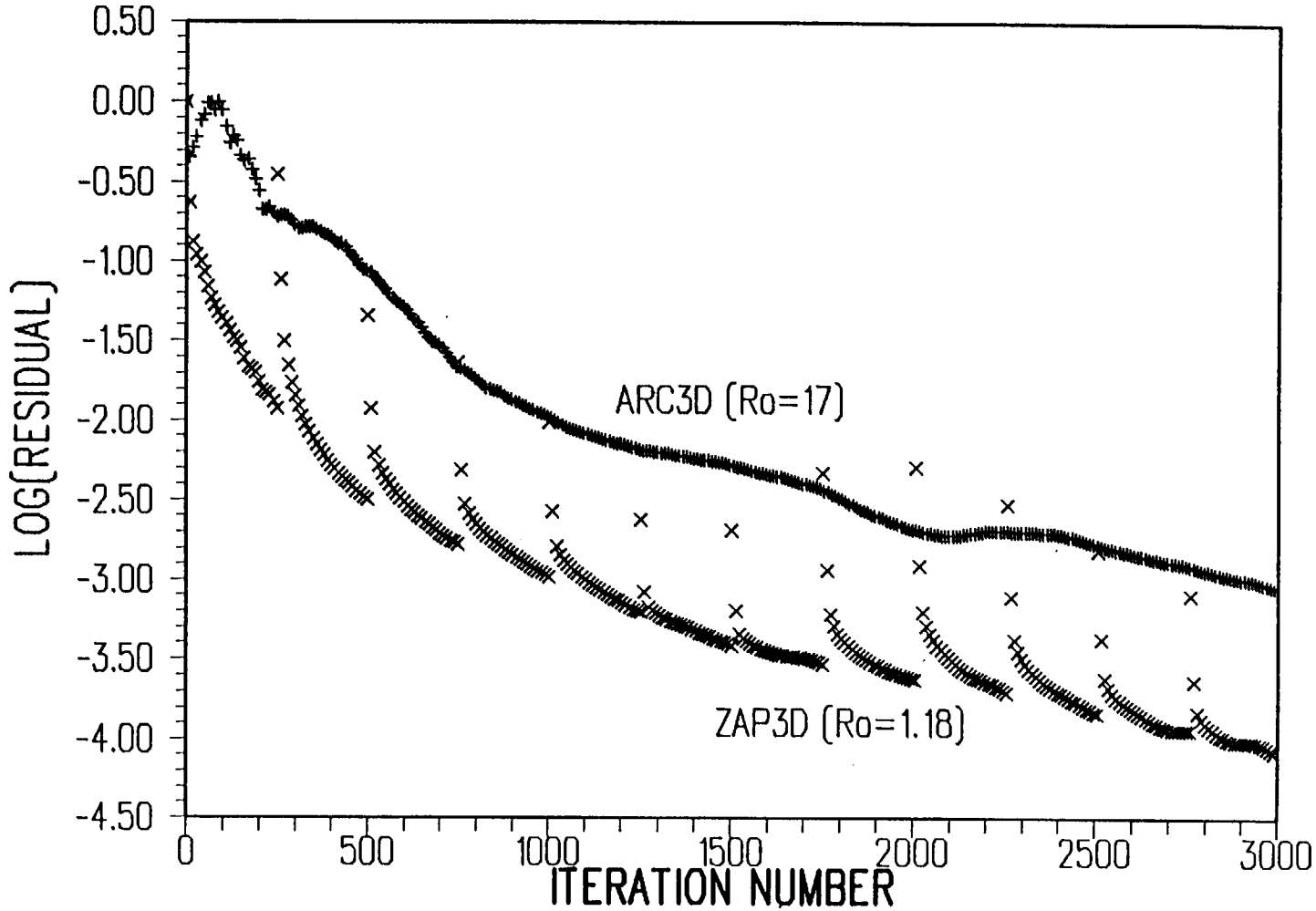

Fig. 28. History of Solution Residual for an AR 5 Rectangular Wing at Mach 0.12, α=8.75 and R_e 1.5 Million.

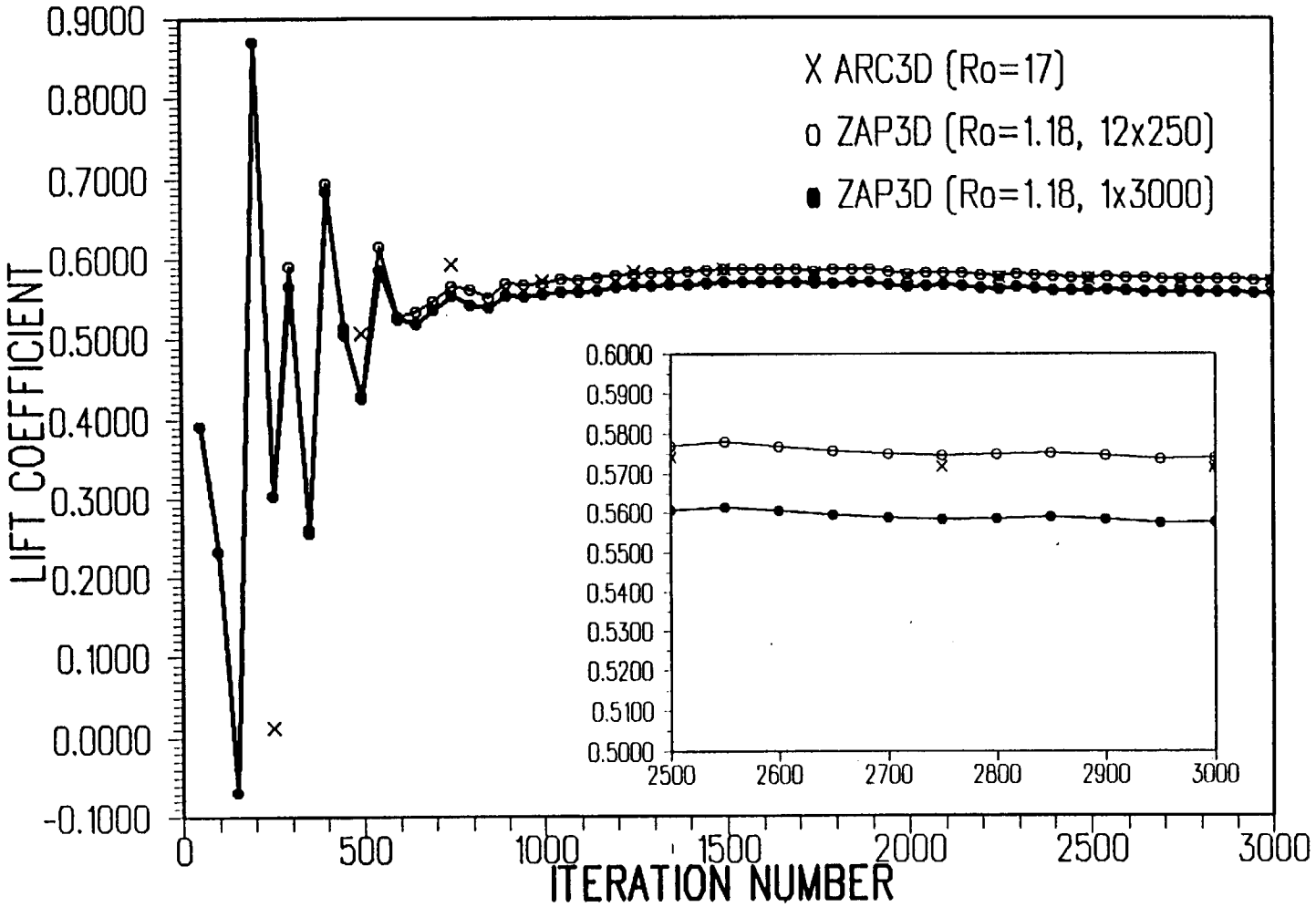

Fig. 29. History of Lift Coefficient for an AR 5 Rectangular wing at Mach 0.12, α=8.75 and R_e 1.5 Million.

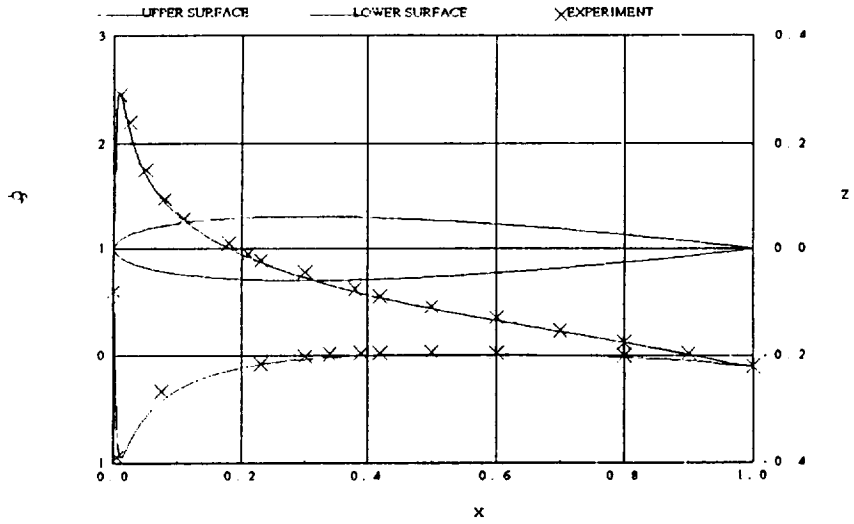

(a) y/b/2 = 0.17

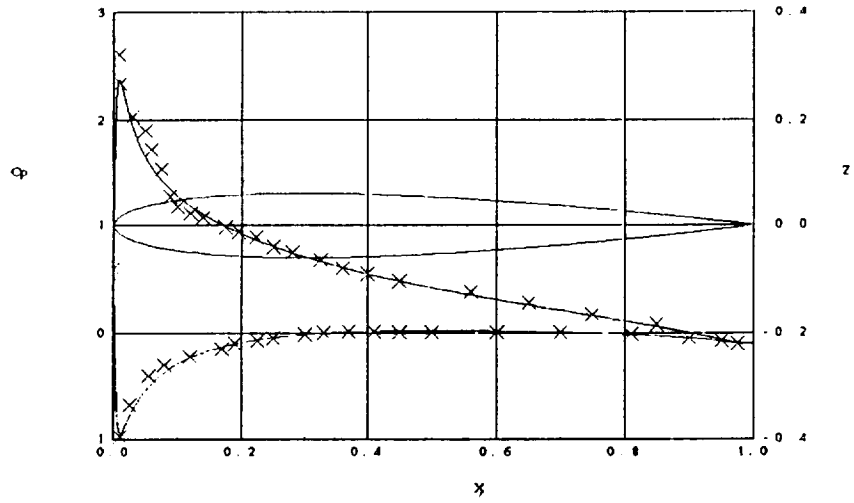

(b) y/b/2 = 0.50

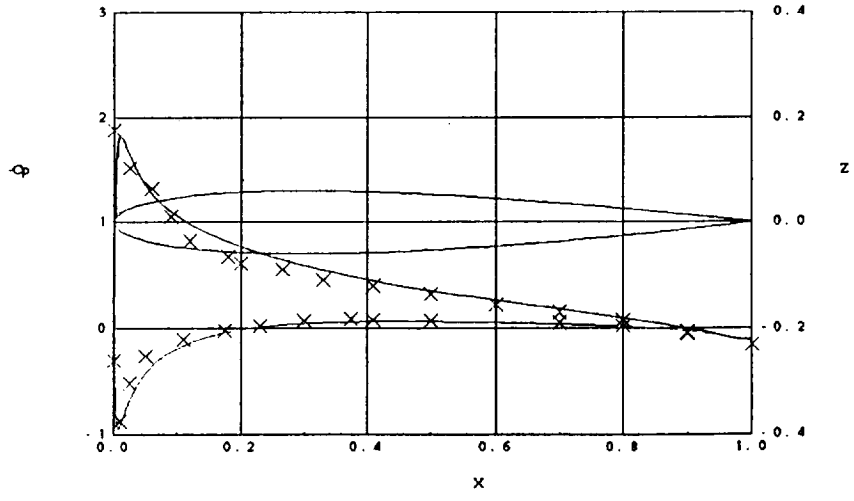

(c) y/b/2 = 0.85

Fig. 30. ZAP3D Computed and Experimental Surface Pressure Distribution for an AR 5 Rectangular Wing at Mach 0.12, α=8.75, R_e 1.5 Million and R_o=1.2.

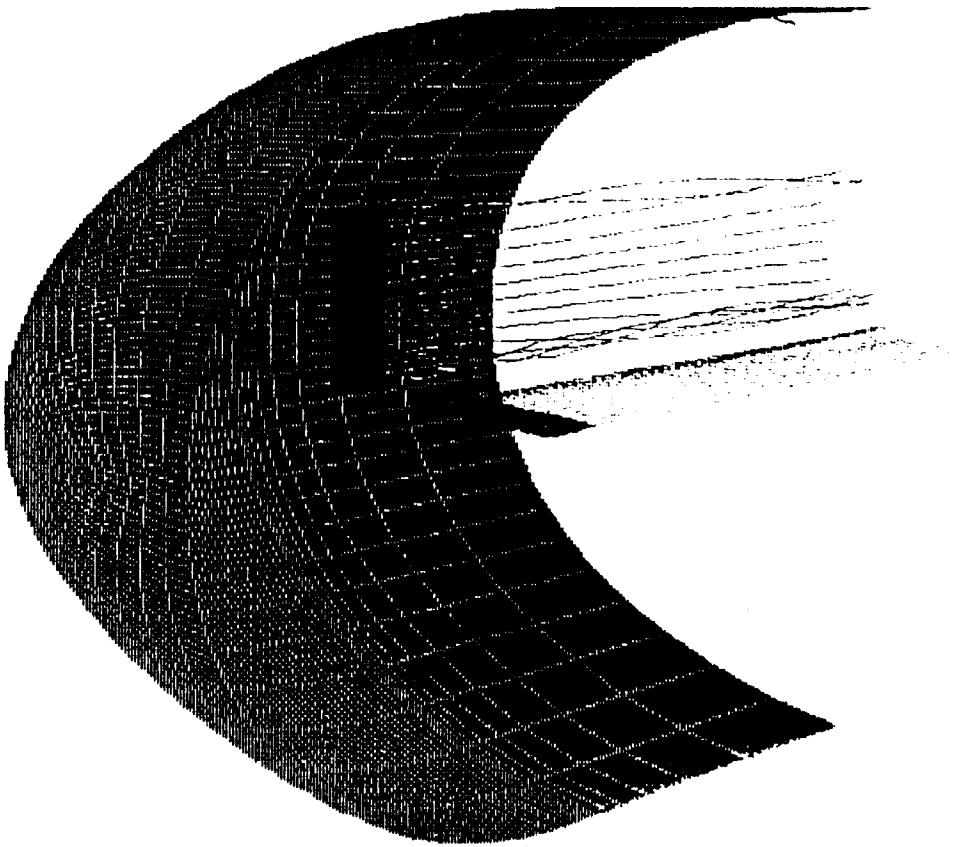

Fig. 31. Computational Model of the Wing/Vortex Validation Case.

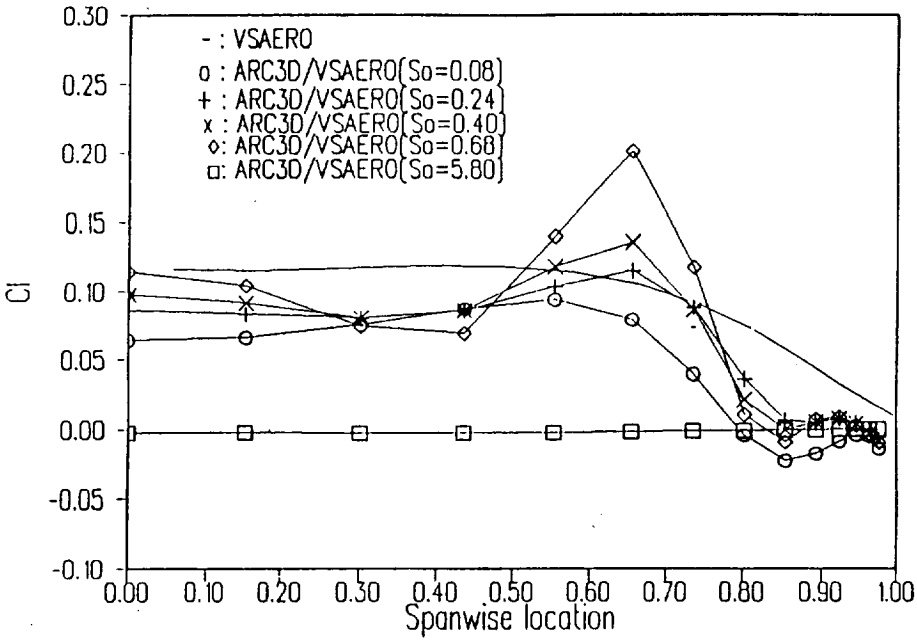

(a) Lift Induced by a Vortex-generating Wing

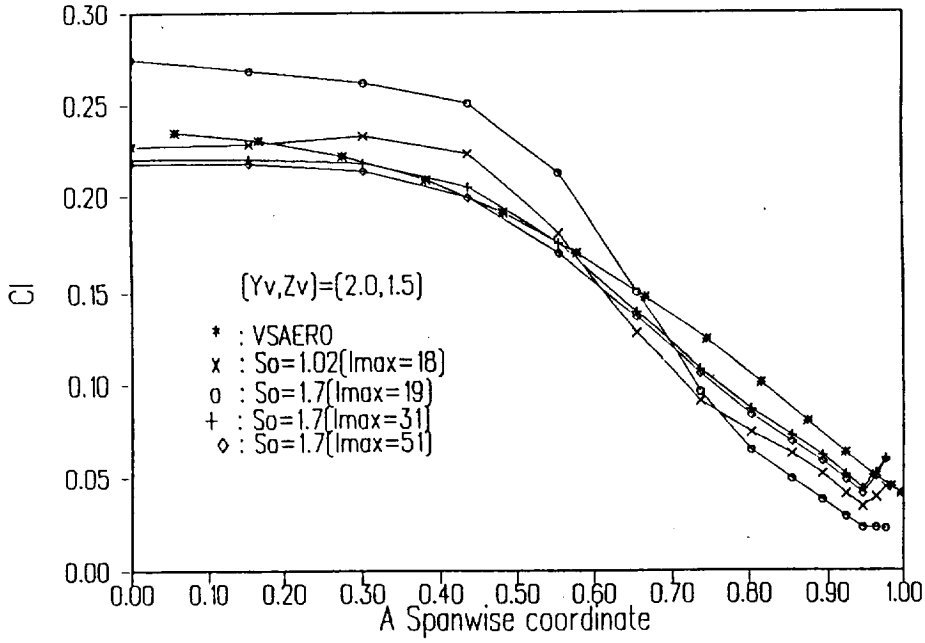

(b) Lift Induced by a Prescribed Vortex Strength NACA 0012 Wing for a Non-lifting Rotor Case

Fig. 32. Comparisons of Calculated lift on a NACA 0012 Wing.

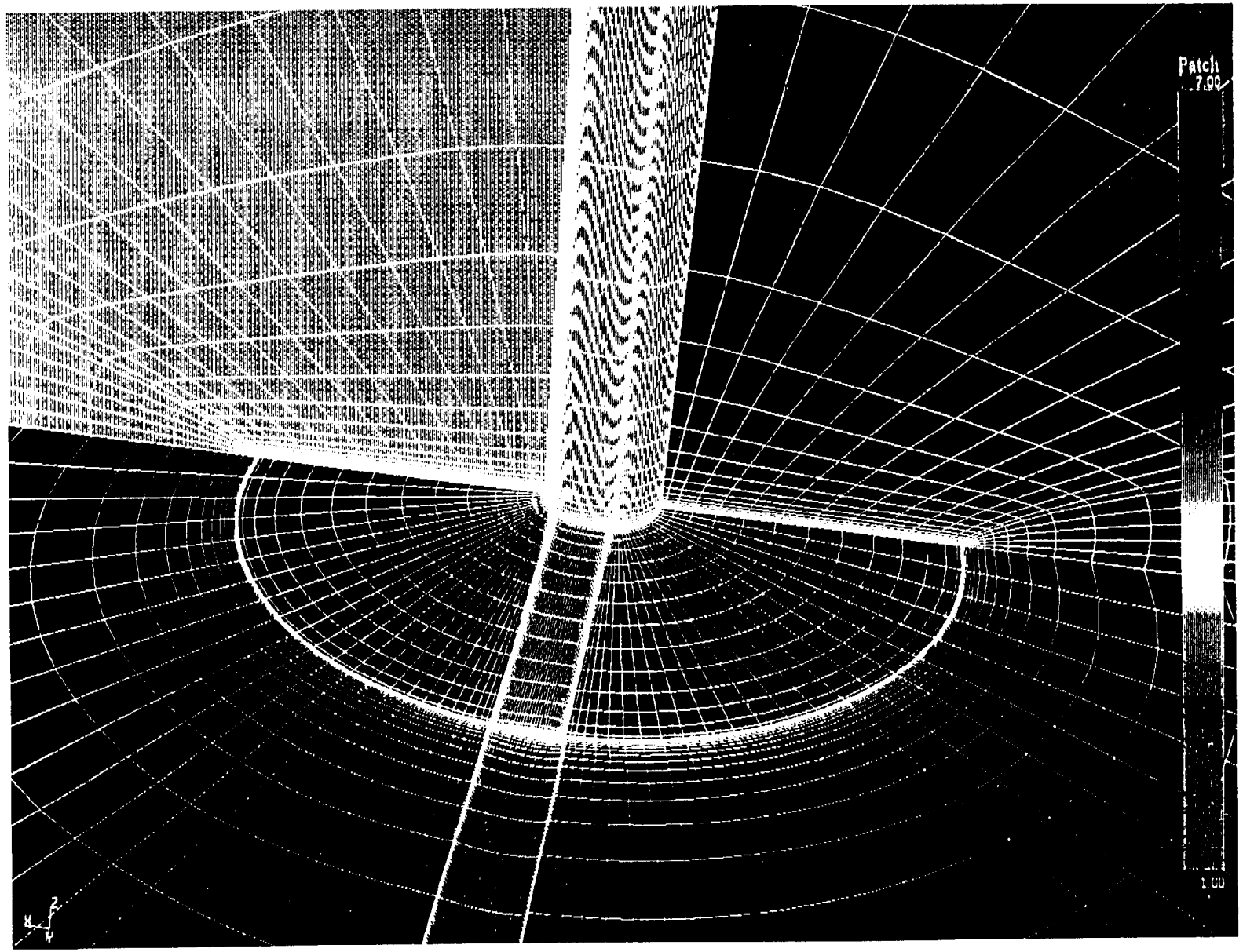

Fig. 33. A Partial View of the Grid Generated around a NACA 0012 Wing for a Non-lifting Rotor Case.

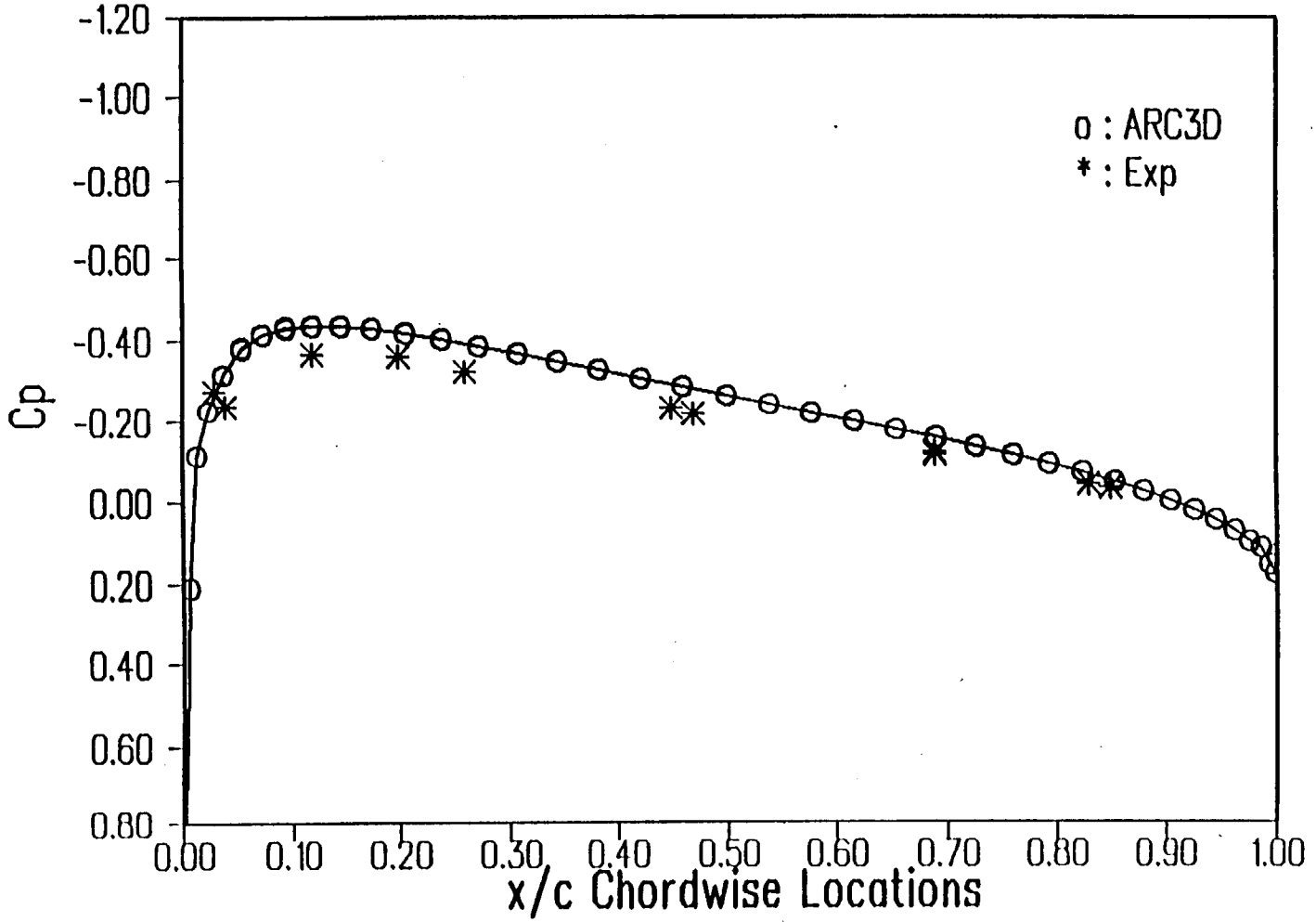

(a) The Span Location Y=0.5

Fig. 34. Calculated Pressure Coefficients Based Upon a Local Dynamic Pressure along the Span Direction (M=0.52, R_e=2.32 Million, θ=0°).

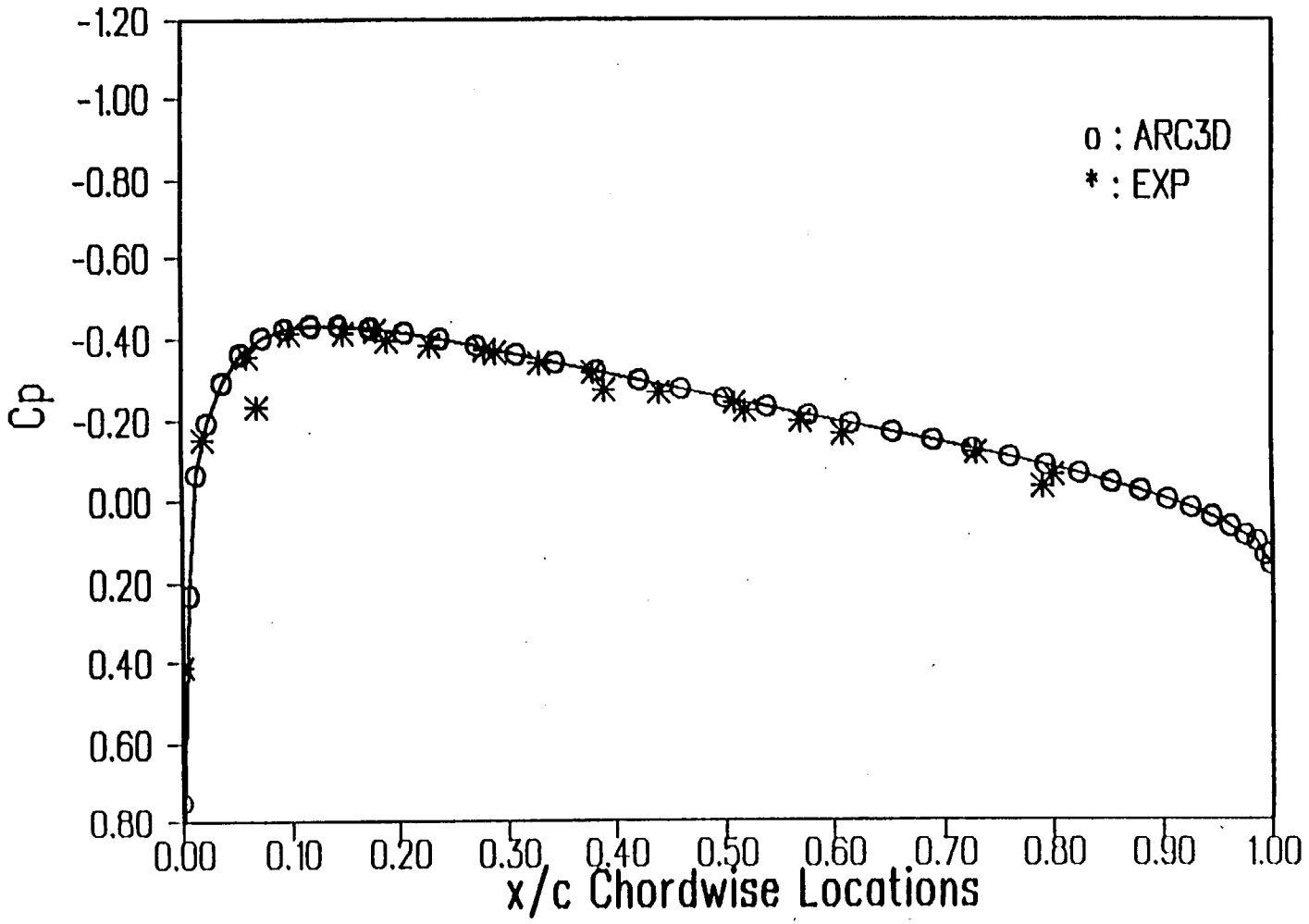

(b) The Span Location Y=0.68

Fig. 34. Continued.

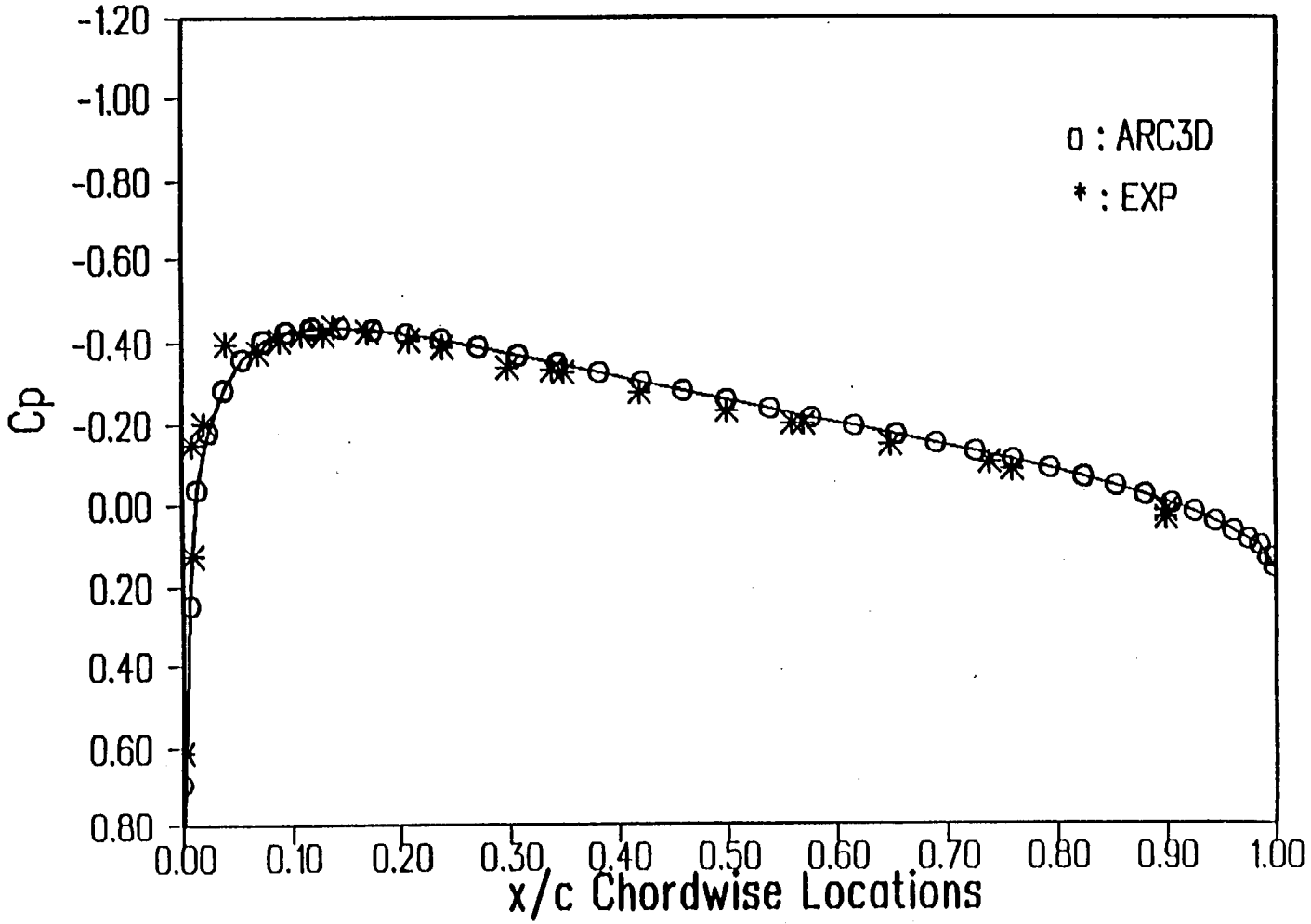

(c) The Span Location Y=0.80

Fig. 34. Continued.

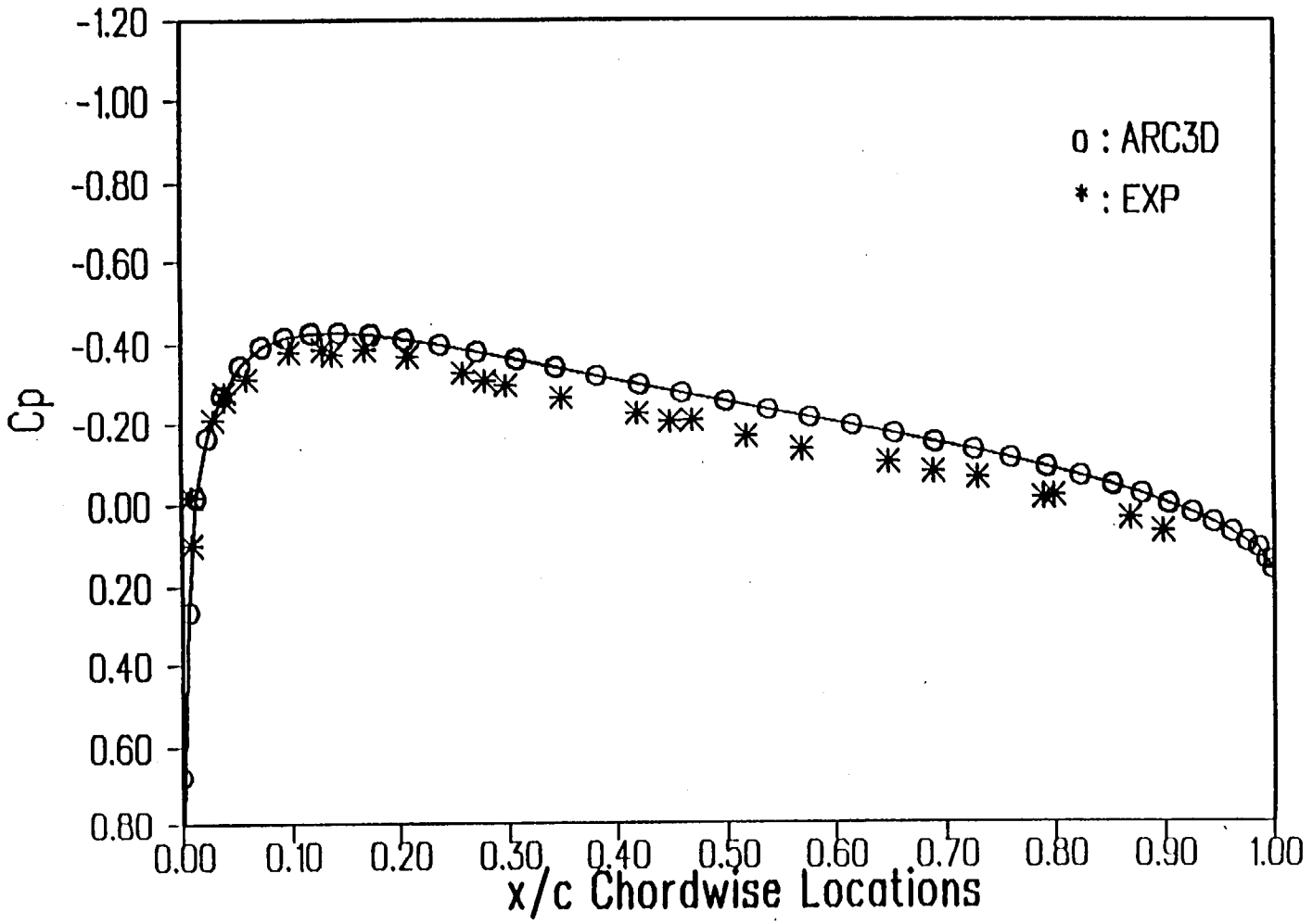

(d) The Span Location Y=0.89

Fig. 34. Continued.

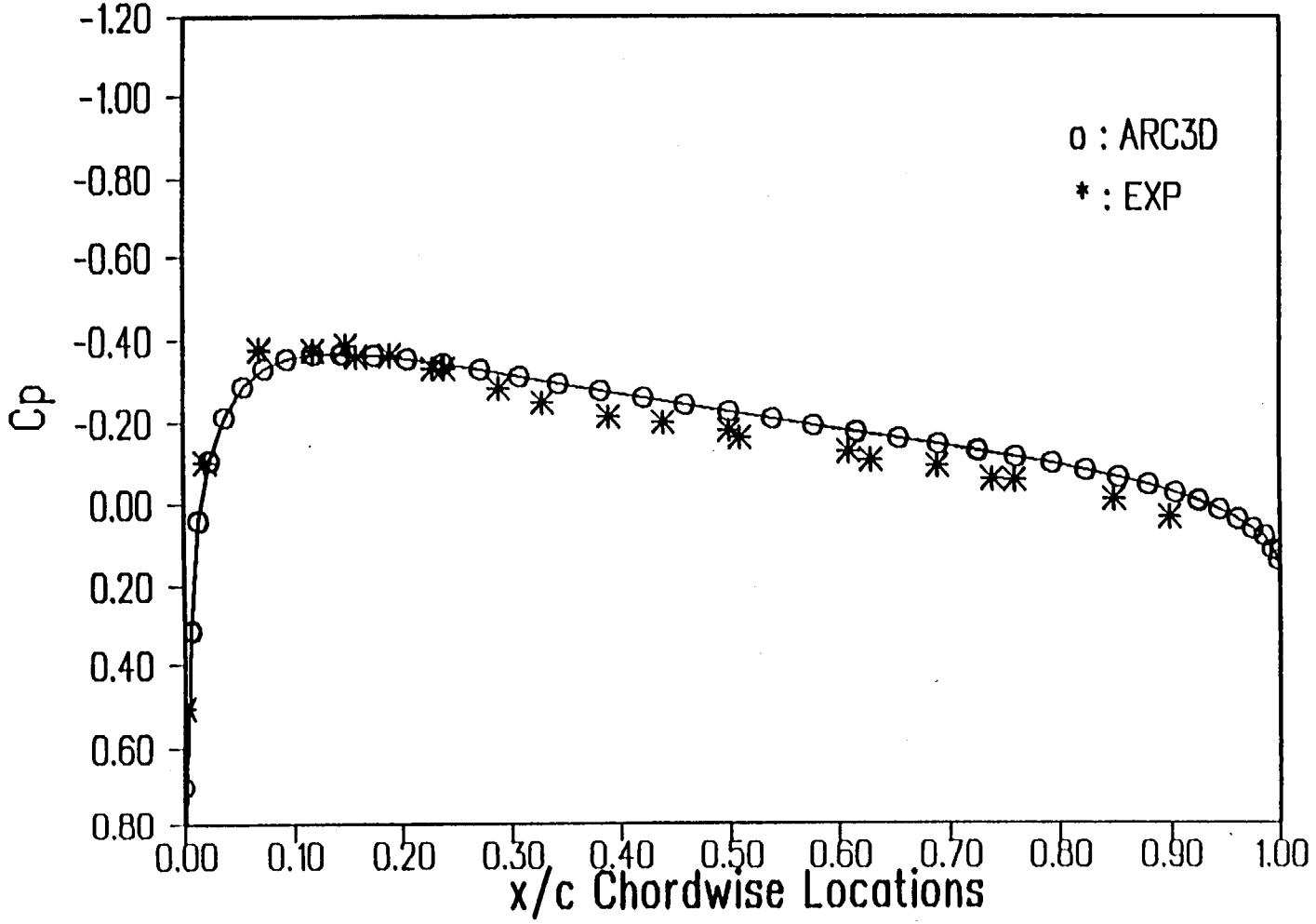

(e) The Span Location Y=0.96

Fig. 34. Concluded.

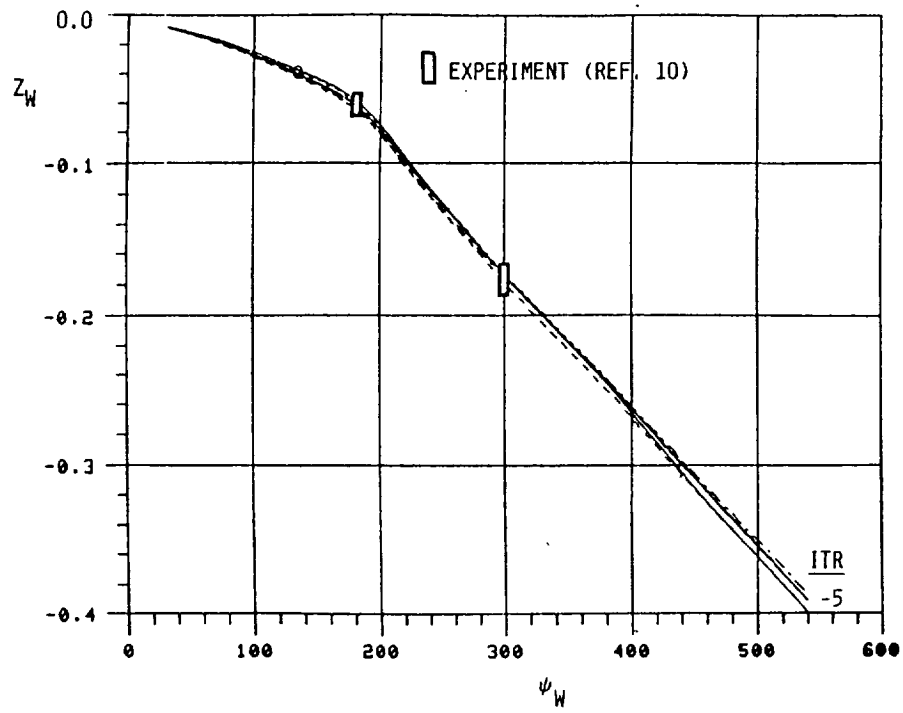

(a) Axial Coordinates

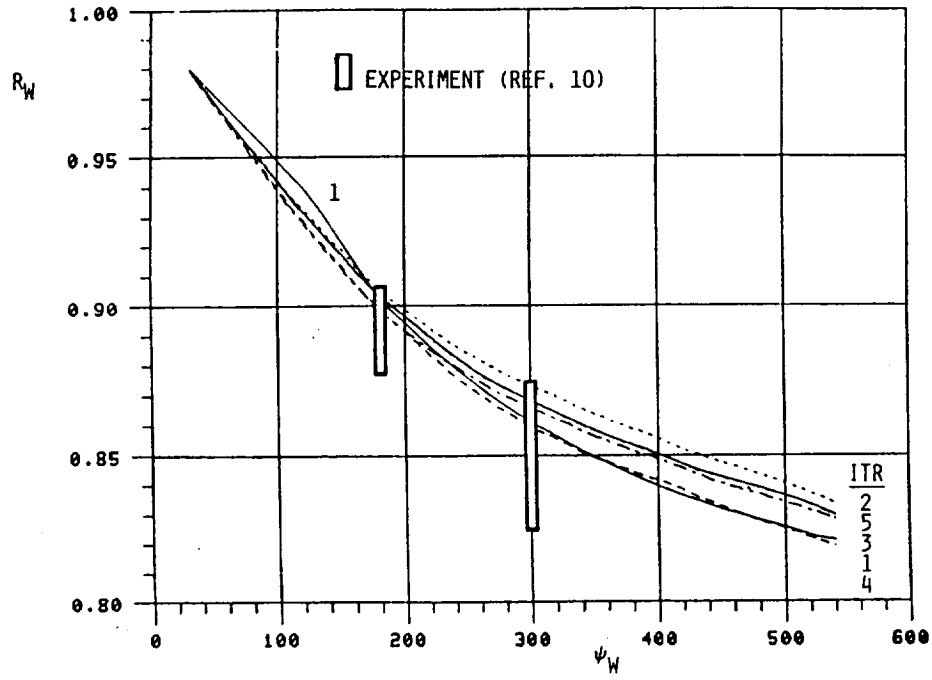

(b) Radial Coordinates

Fig. 35. Comparison of Experimental and Calculated Tip-vortex Geometry for the Un-twisted Rotor of Ref. 10.

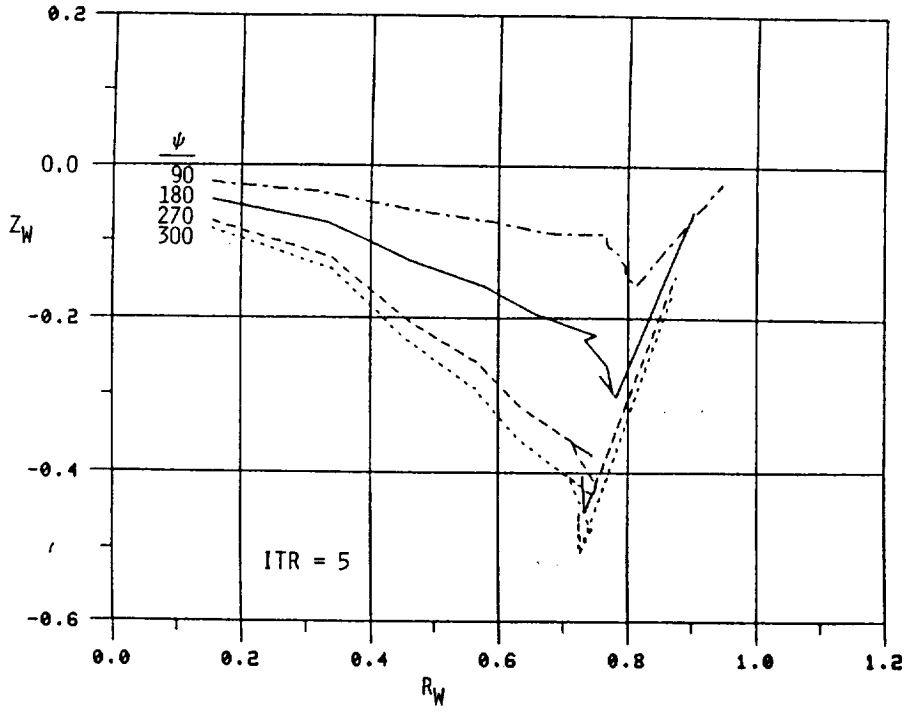

Fig. 36. Final Calculated Relaxed Wake Geometry at Constant Azimuth for the Un-twisted Rotor of Ref. 10.

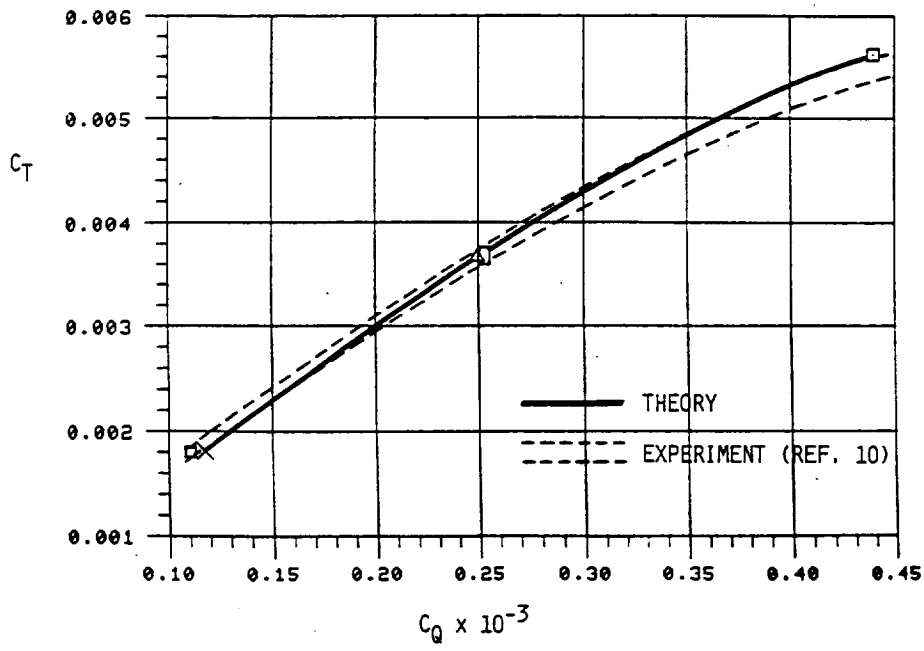

Fig. 37. Comparison of Calculated and Experimental Hover Performance for the Un-twisted Rotor of Ref. 10.

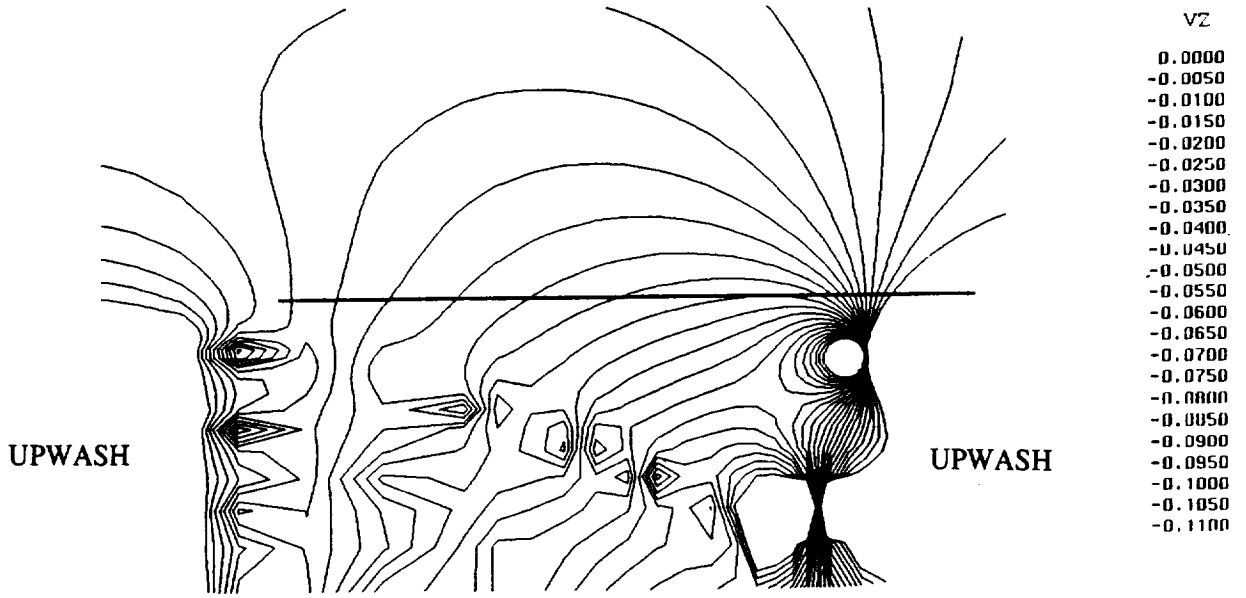

(a) Complete Flow Field

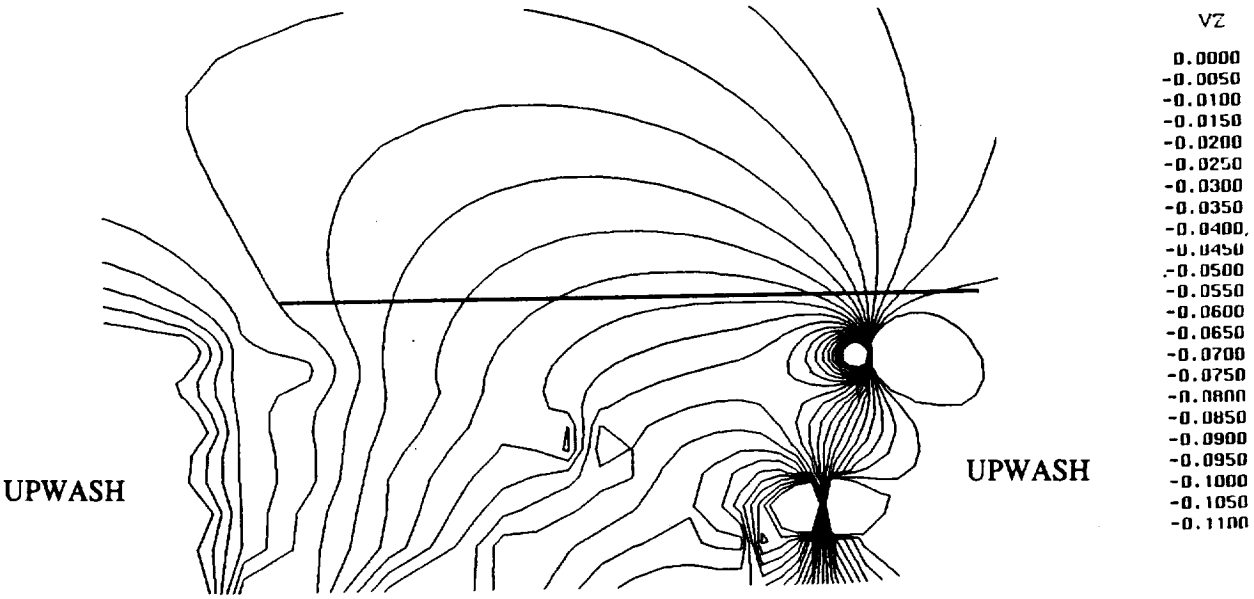

(b) Flow Field Outside of S_i

Fig. 38. The Downwash Predicted by HOVER for the Viscous Calculations at an Upstream Plane.

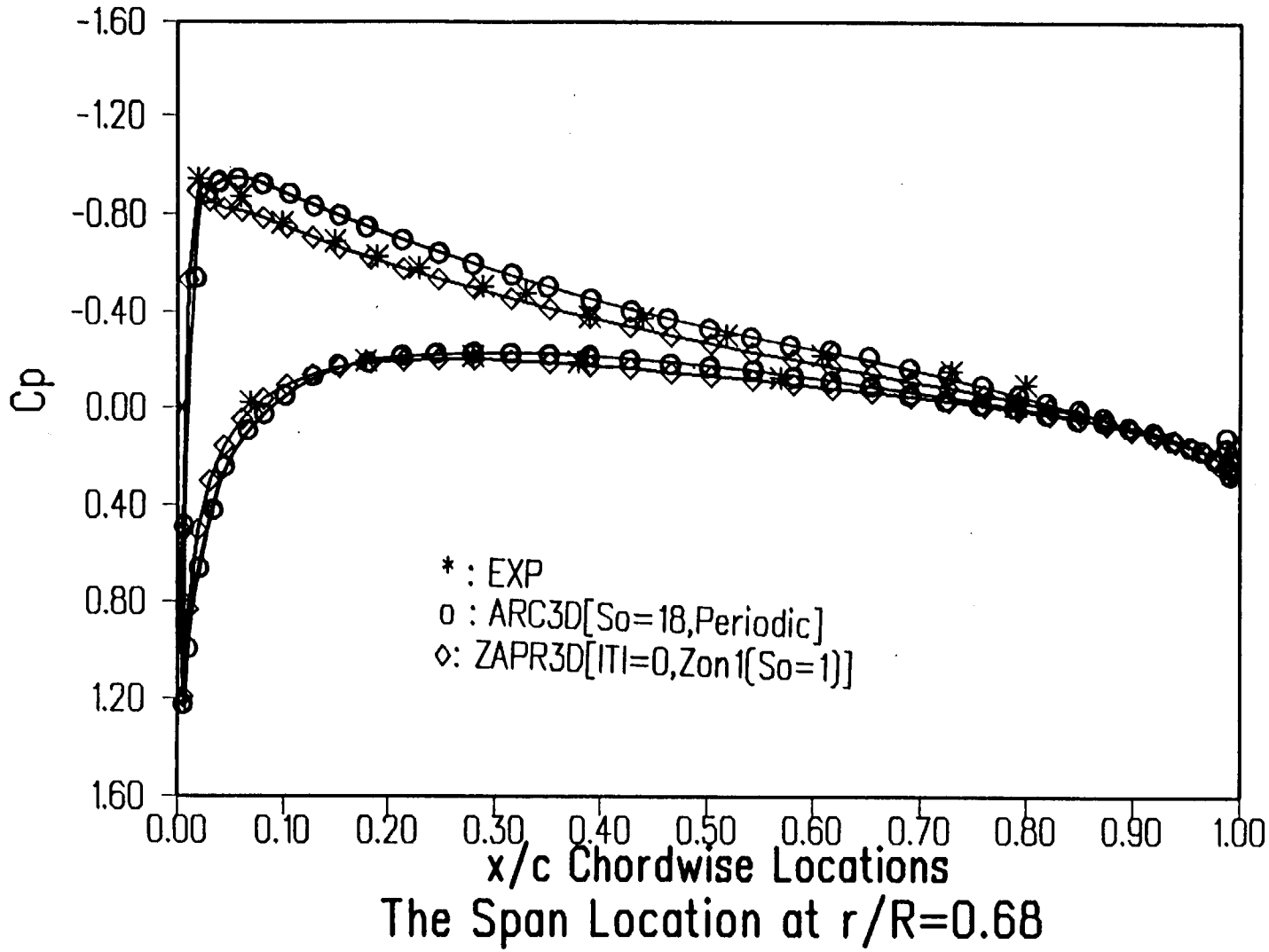

Fig. 39. Comparison of the Calculated and Experimental Chorwise Pressure Distribution at r/R=0.68 for a Rotor in Hover (M=0.44, Re=1.92 Million, θ=8°).

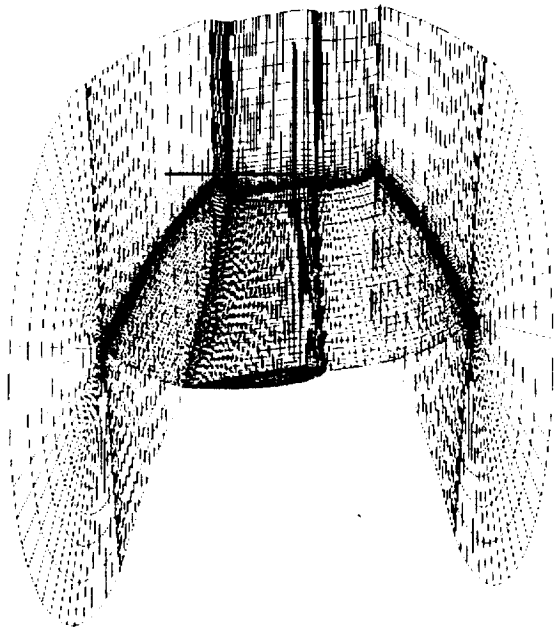

Fig. 40. Selected Planes and Grid for a Reduced Domain (Zon1) Simulation.

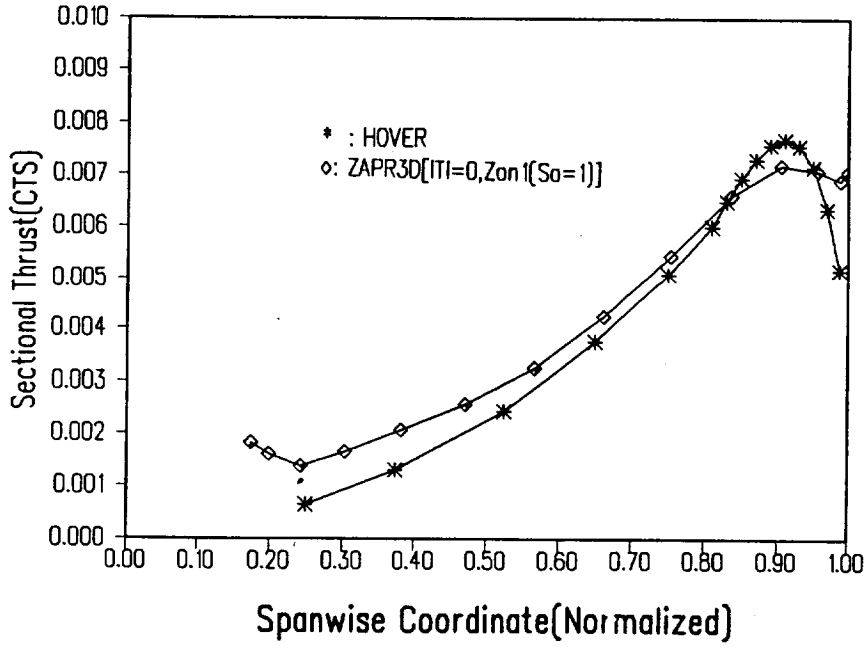

Fig. 41. Comparison of the Calculated Radial Thrust Distribution by HOVER and ZAPR3D (Zon1) (M=0.44, Re=1.92 Million, θ=8°).

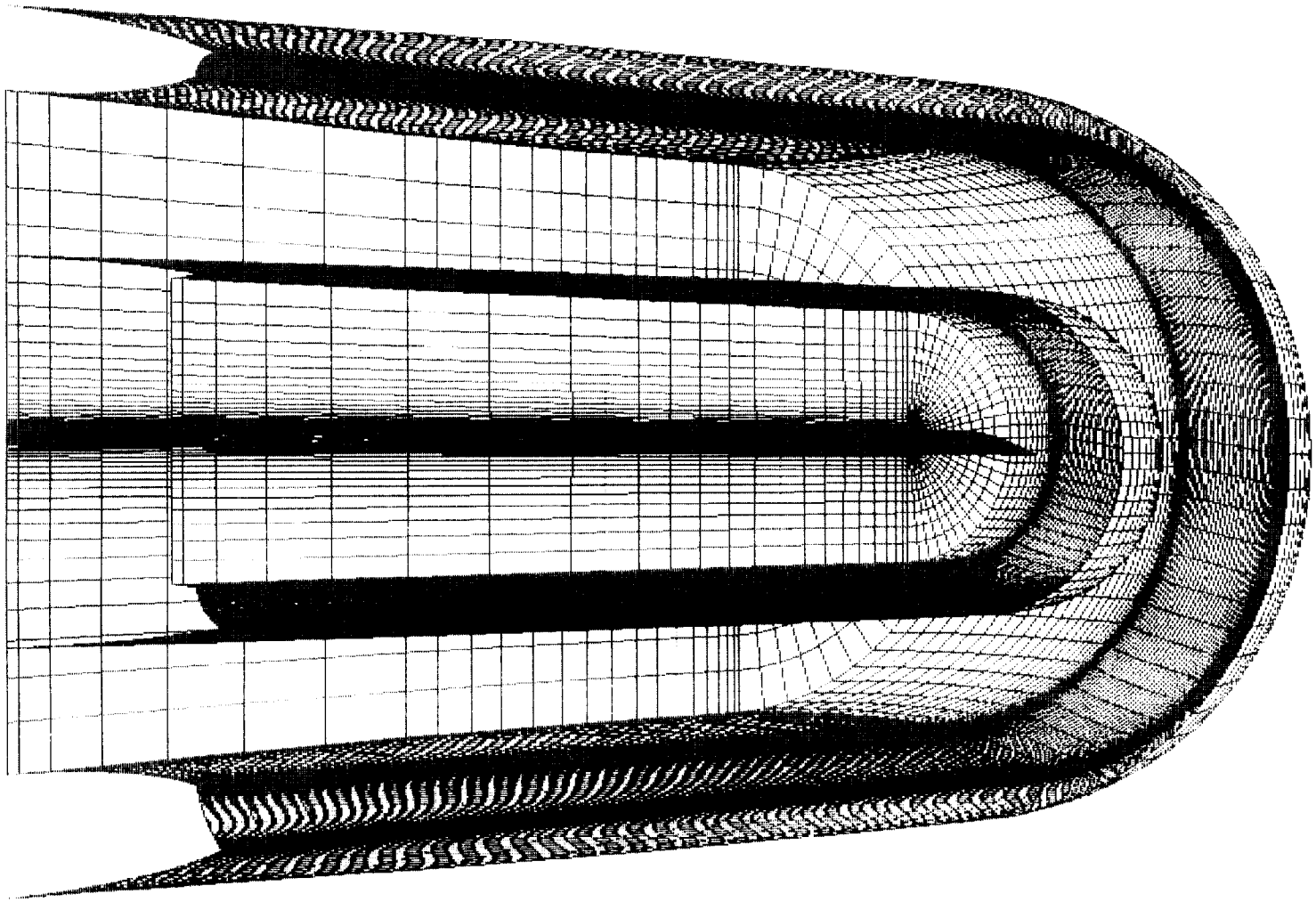

Fig. 42. ZAPR3D Zonal Boundaries and Dense Grid (Zon2) for the Rotor Simulation.

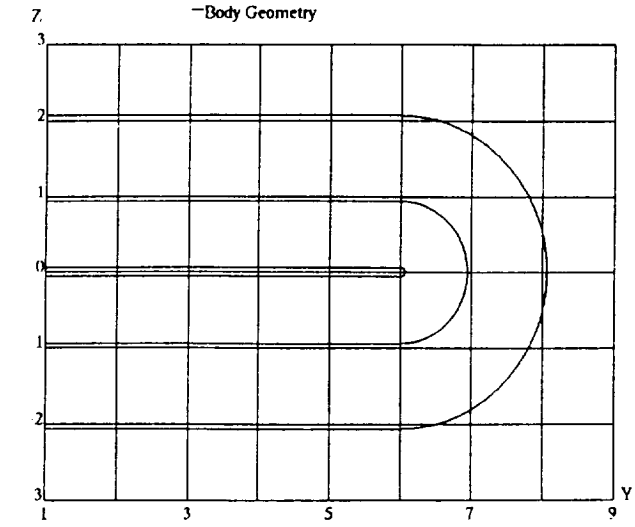

(a) α=0.0

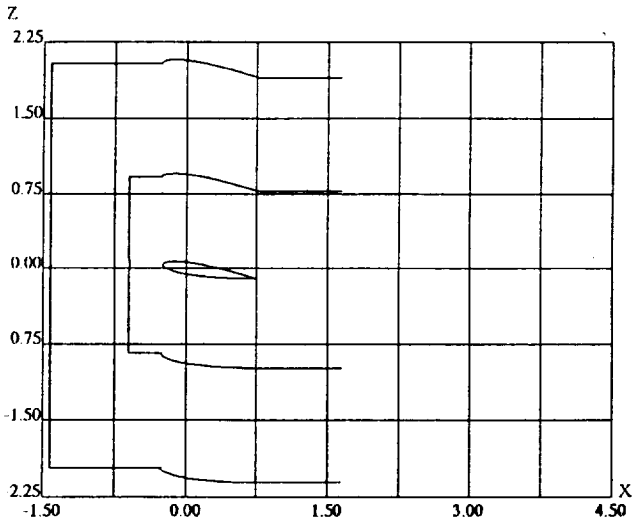

(b) Y=4.5

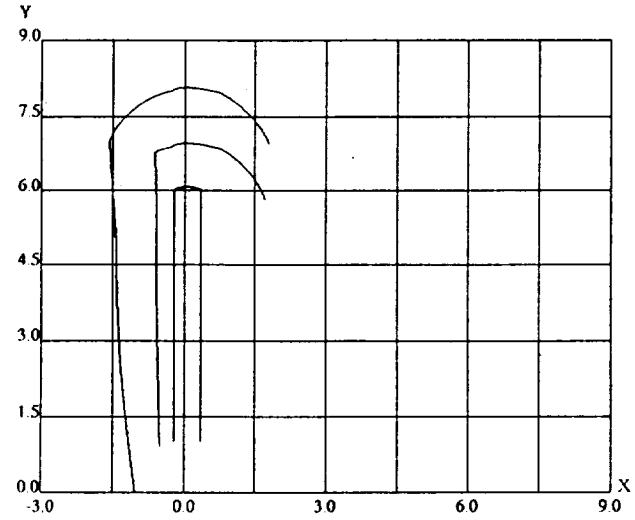

(c) Z=0.0

Fig. 43. Geometric Data Cuts of the Zonal Boundaries (Zon2).

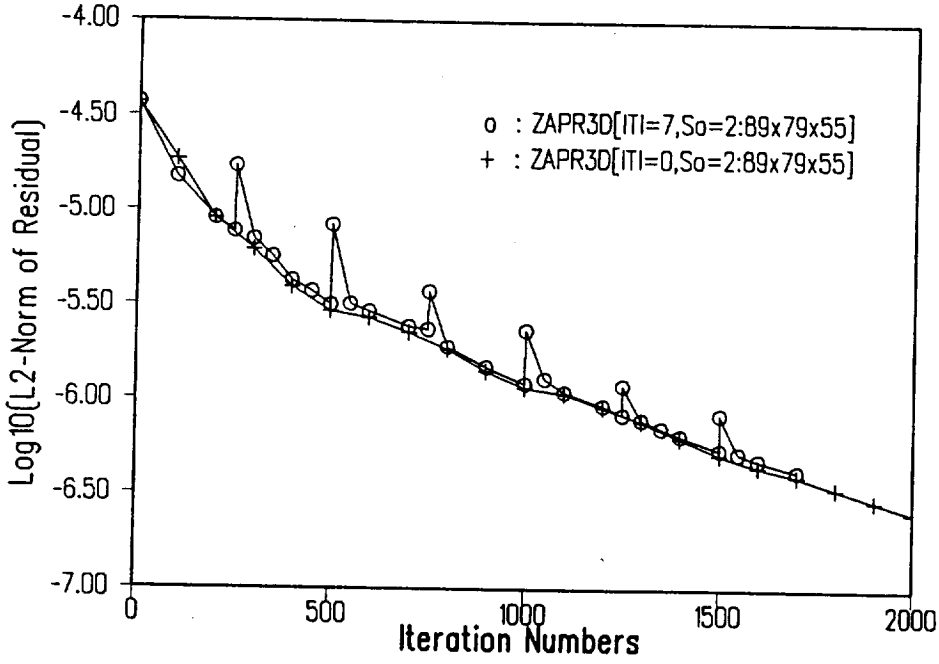

Fig. 44. ZAPR3D Residual Convergence History for a Two-Bladed Rotor (M=0.44, Re=1.92 Million, θ=8°).

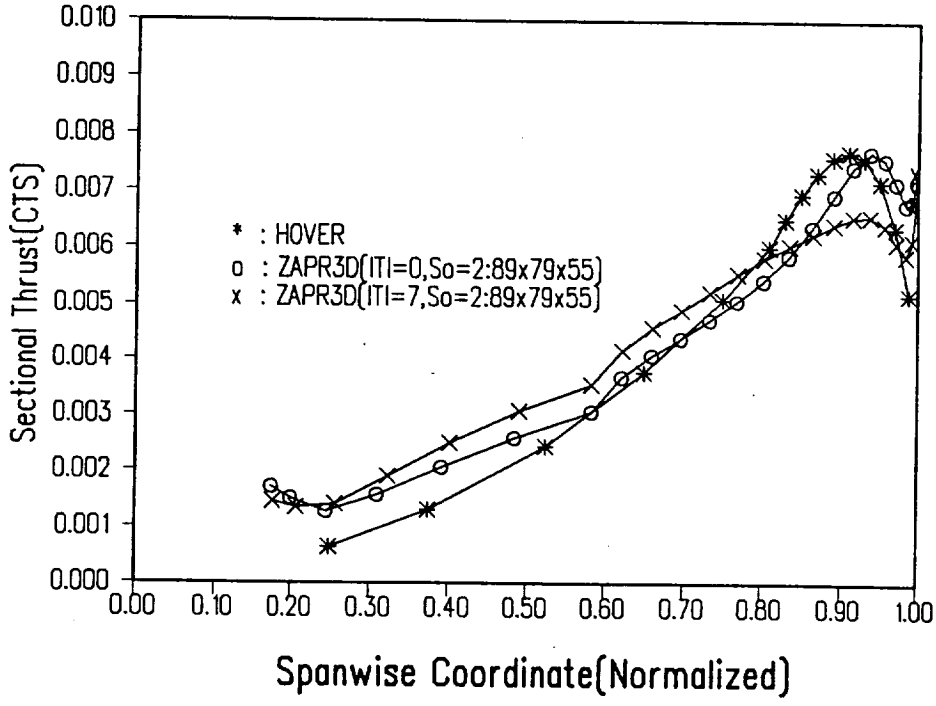

Fig. 45. Comparison of HOVER and ZAPR3D Computed Radial Thrust Distribution for a Two-Bladed Rotor (M=0.44, Re=1.92 Million, θ=8°).

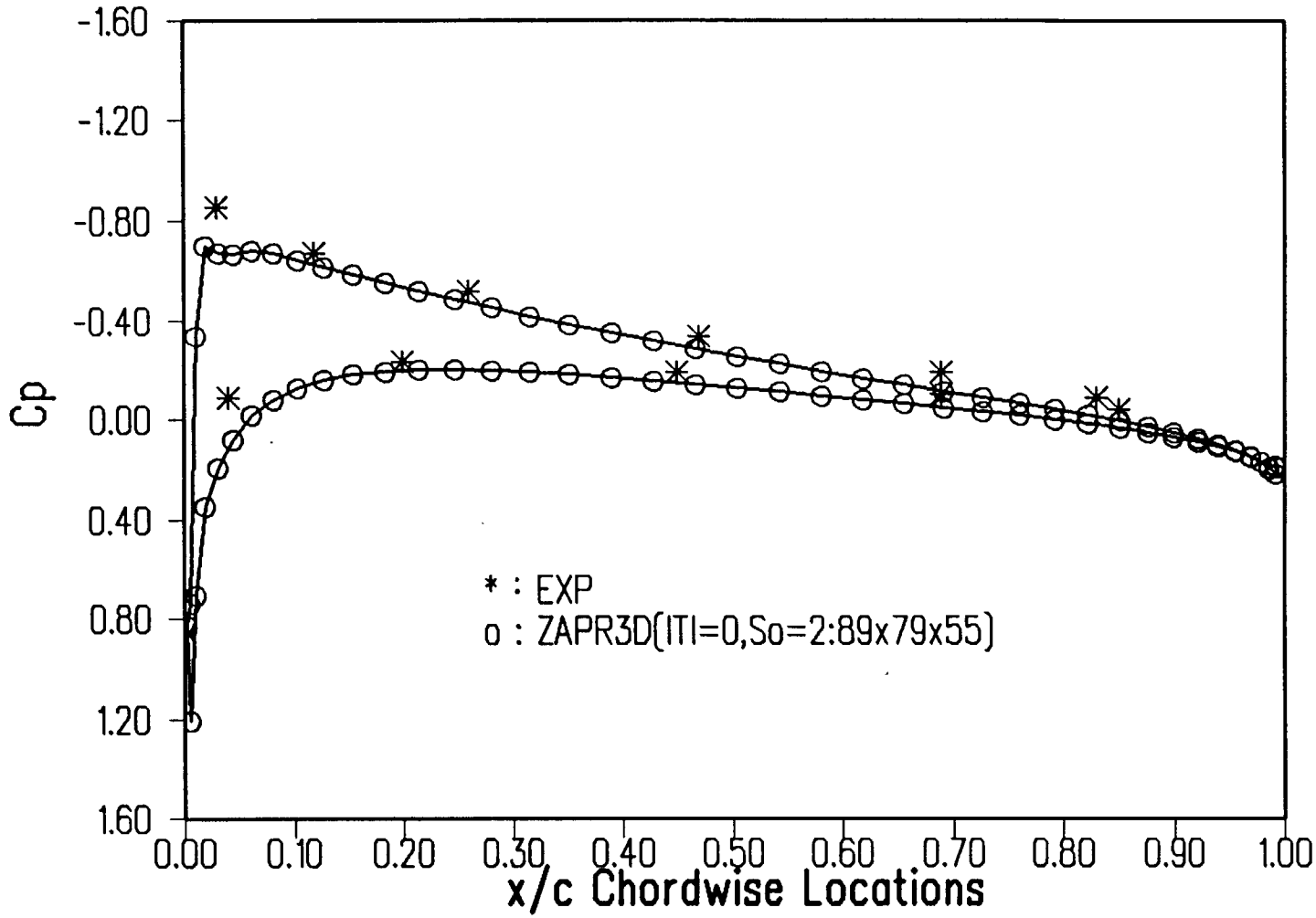

(a) Y=0.50

Fig. 46. Comparison of ZAPR3D Calculated and Experimental Chordwise Pressure Distribution for a Two-Bladed Rotor (M=0.44, Re=1.92 Million, θ=8°).

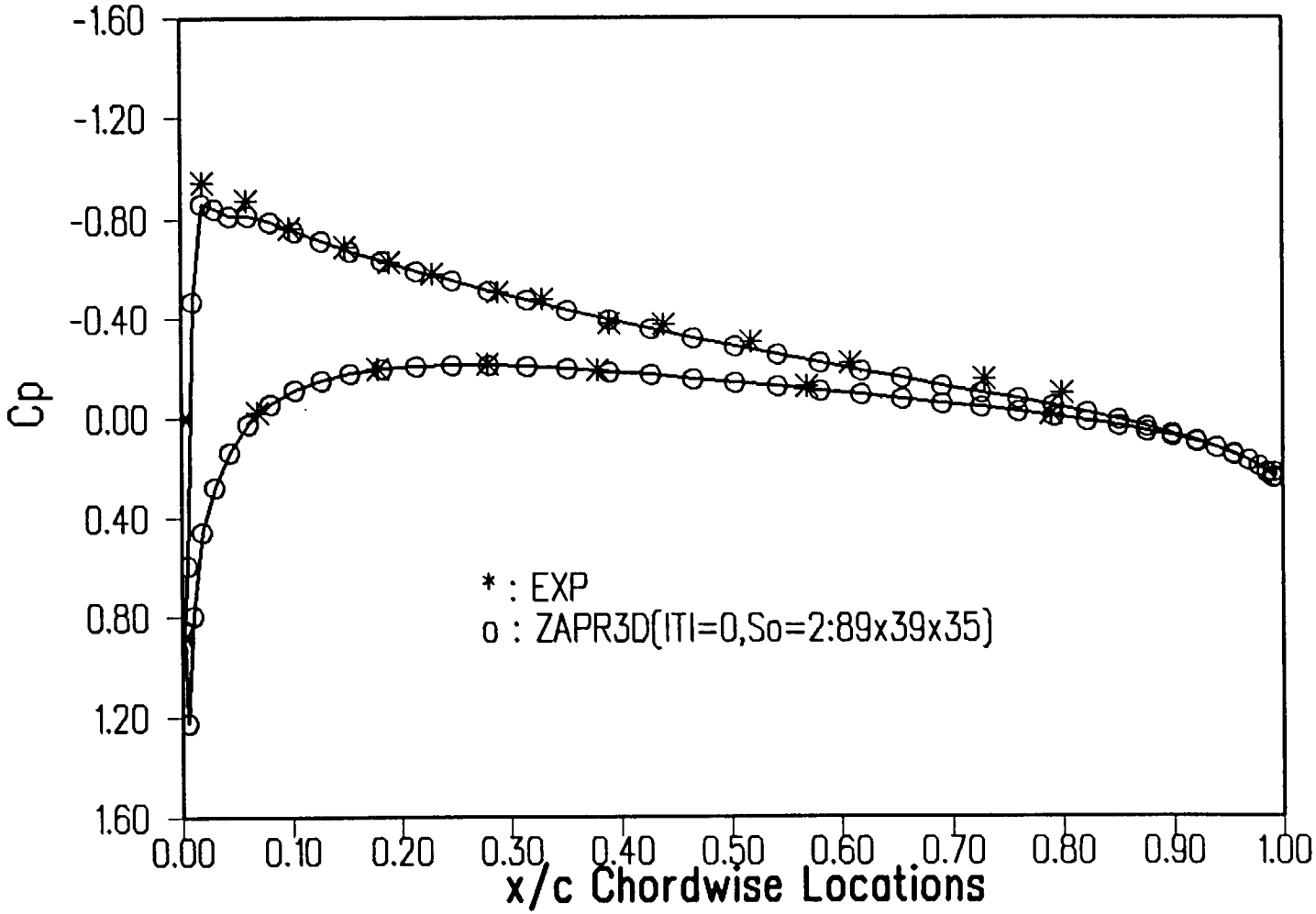

(b) Y=0.68

Fig. 46. Continued.

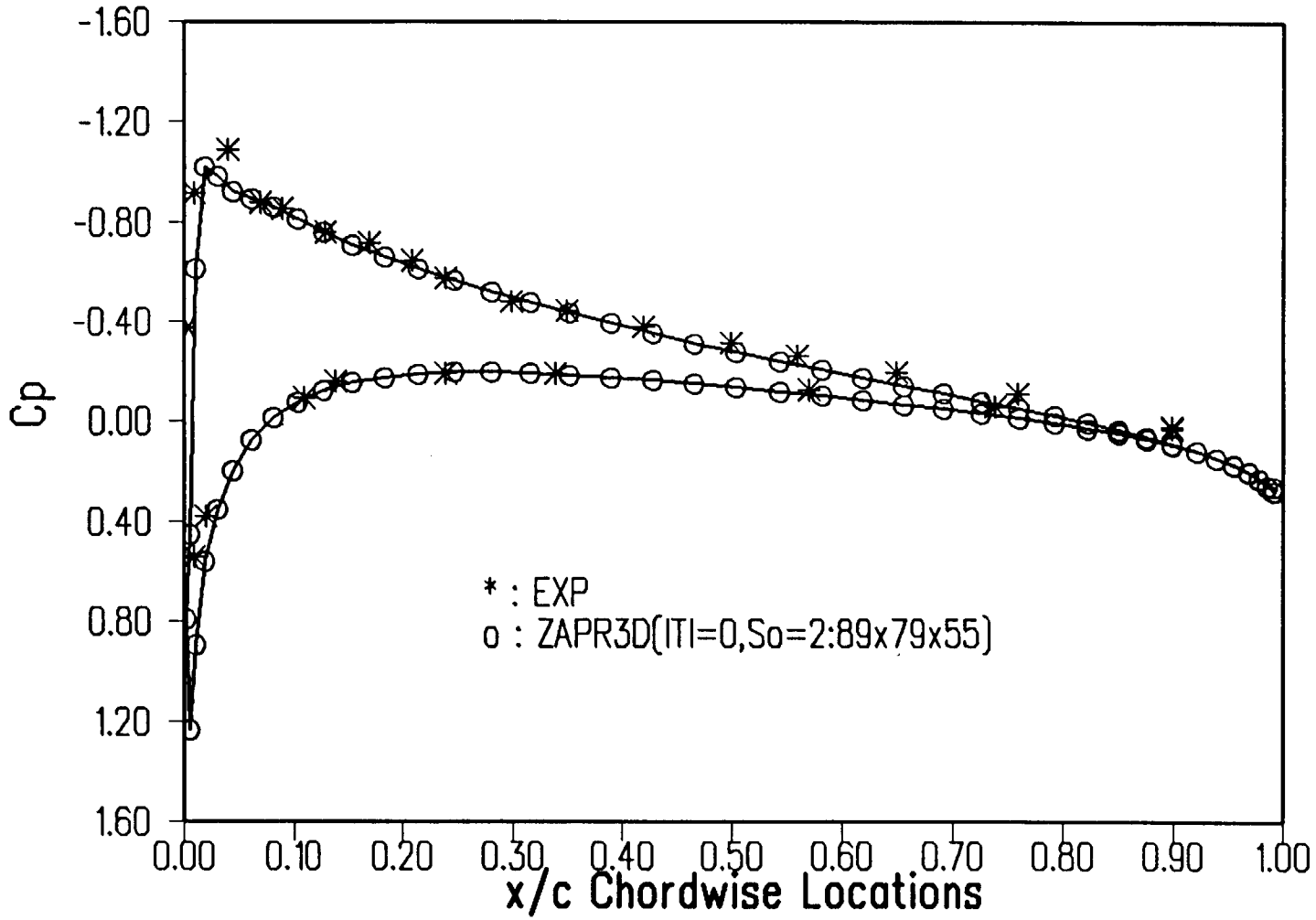

(c) Y = 0.80

Fig. 46. Continued.

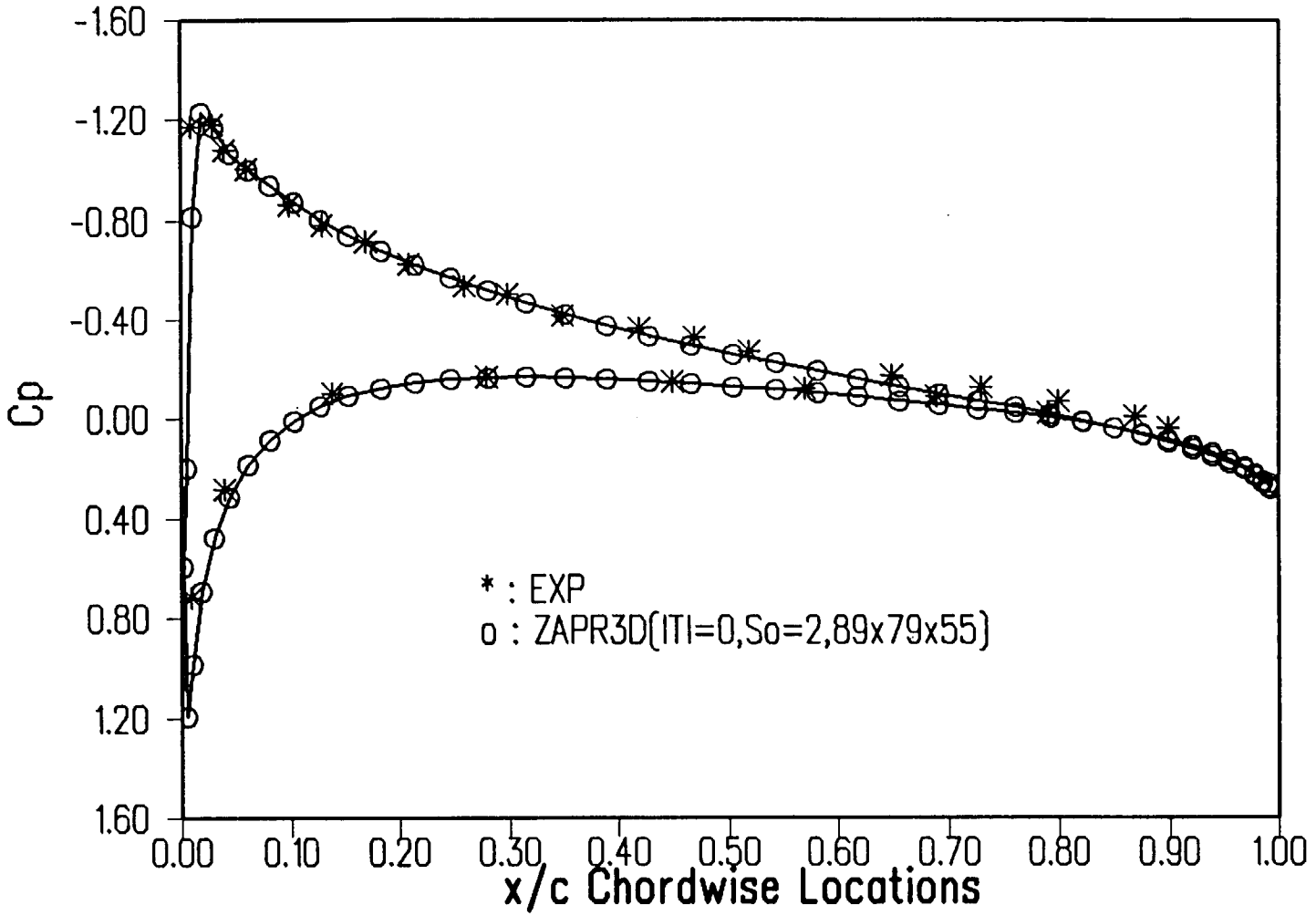

(d) Y=0.89

Fig. 46. Continued.

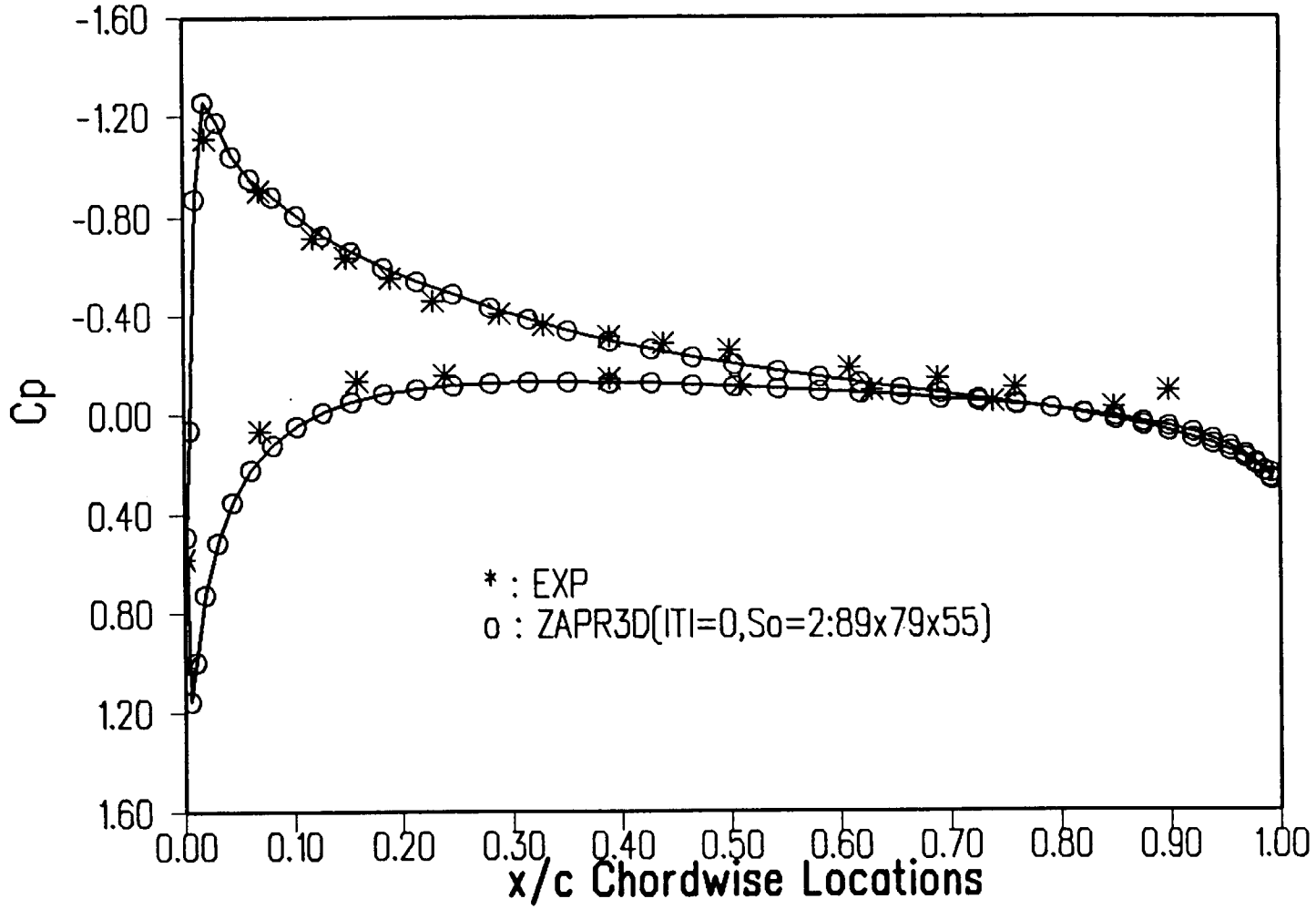

(e) Y=0.96

Fig. 46. Concluded.

NASA National Aeronautics and Space Administration

Report Documentation Page

1. Report No.	2. Government Accession No.	3. Recipient's Catalog No.

4. Title and Subtitle
A Novel Potential/Viscous Flow Coupling Technique for Computing Helicopter Flow Fields

5. Report Date
June 1993

6. Performing Organization Code
9M695

7. Author(s)
J. M. Summa
D. J. Strash
S. Yoo

8. Performing Organization Report No.
9304

10. Work Unit No.

9. Performing Organization Name and Address
Analytical Methods, Inc.
2133 - 152nd Avenue, NE
Redmond, WA 98052

11. Contract or Grant No.
NAS2-13194

12. Sponsoring Agency Name and Address
National Aeronautics and Space Administration
Ames Research Center ASF: 241-1
Moffett Field, CA 94035-1000

13. Type of Report and Period Covered
Final
16 MAR 90 - 26 MAY 93

14. Sponsoring Agency Code

15. Supplementary Notes

The primary objective of this work was to demonstrate the feasibility of a new potential/viscous flow coupling procedure for reducing computational effort while maintaining solution accuracy. This closed-loop, overlapped, velocity-coupling concept has been developed in a new two-dimensional code, ZAP2D (Zonal Aerodynamics Program-2D), a three-dimensional code for wing analysis, ZAP3D (Zonal Aerodynamics Program-3D), and a three-dimensional code for isolated helicopter rotors in hover, ZAPR3D (Zonal Aerodynamics Program for Rotors-3D). Comparisons with large domain ARC3D solutions and with experimental data for a NACA 0012 airfoil have shown that the required domain size can be reduced to a few tenths of a percent chord for the low Mach and low angle of attack cases and to less than 2-5 chords for the high Mach and high angle of attack cases while maintaining solution accuracies to within a few percent. This represents CPU time reductions by a factor of 2-4 compared with ARC2D. The current ZAP3D calculation for a rectangular plan-form wing of aspect ratio 5 with an outer domain radius of about 1.2 chords represents a speed-up in CPU time over the ARC3D large domain calculation by about a factor of 2.5 while maintaining solution accuracies to within a few percent. A ZAPR3D simulation for a two-bladed rotor in hover with a reduced grid domain of about two chord lengths was able to capture the wake effects and compared accurately with the experimental pressure data. Further development is required in order to substantiate the promise of computational improvements due to the ZAPR3D coupling concept.

17. Key Words (Suggested by Author(s))
Navier Stokes
Potential Flow
Zonal Coupling
Rotor

18. Distribution Statement
Distribution Unlimited

19. Security Classif. (of this report)	20. Security Classif. (of this page)	21. No. of pages	22. Price
Unclassified	Unclassified	79	